MIMO Visible Light Communications with Camera-Based Receiver for Intelligent Transport Systems

Navid Bani Hassan

A thesis submitted in partial fulfilment of the requirements of the University of Northumbria at Newcastle for the degree of Doctor of Philosophy

Research undertaken at the Faculty of Engineering and Environment

February 2019

Abstract

The number of vehicle accidents in the world each year is considerable which yield to an approximately 1.2 million deaths. Besides, the car manufacturers are now investing significantly on autonomous vehicles, which highlights the need for communication between vehicles and the surrounding environment. Intelligent Transportation Systems (ITS) enables the vehicles to realize this need. In ITS, vehicles and infrastructure can communicated directly without the need of cellular networks. Currently, the developed technology for ITS is based on radio frequency (RF) under the name of dedicated short-ranged communication (DSRC), which shares the frequency spectrum with other RF applications such as fixed satellite and wireless services, mobile services, radiolocation, etc. Therefore, DSRC can be a potential interfering source for other communication services. Besides, the licence to use this spectrum makes this service costly in the frequency range of 5.855-5.925 GHz and in heavy traffics may cause severe packet collision. Alternatively, visible light communication (VLC) can be used to release the pressure on RF. The equipment required for VLC, such as light emitting diodes (LEDs), camera, and computer, is already available on most of the vehicles nowadays. Therefore, VLC can be considered as a less expensive option for ITS. Most of the works done in camera-based VLC, also known as optical camera communication (OCC), consider a line-of-sight (LOS) link from the transmitter (Tx) to the receiver (Rx). However, in some scenarios, the LOS link might not be available. In this thesis, a non-LOS (NLOS) link is considered to decrease the probability of outage. Accordingly, this thesis highlights another advantage of using camera compared to photodiodes, i.e., the Rx can extract the data information from the off-axis projection of the Tx on the road surface when the LOS link is blocked or is not available. An end-to-end NLOS OCC system is proposed which employs differential signalling and frame subtraction. Throughout the thesis, different detection techniques are proposed based on spatial division multiplexing (SDM) and time division multiplexing (TDM), hybrid selection/equal gain combining (HS/EGC), hybrid selection/maximal ratio combining (HS/MRC), and zero forcing (ZF) equalization, respectively. The thesis deals with different types of the road in terms of the density of the light sources. An experimental investigation of the proposed system shows that, using HS/EGC and simple detection zero forcing equalization (SDZFE), the system can achieve the 7% overhead forward error correction limit of 3.8×10^{-3} at a very low transmit power of 9 dBm over a link span of 5 m at a data rate of 30 bps, when the Tx is 2 m above the floor surface. It is also shown that by doubling the ISO level, exposure time and aperture size, the performance of the system improves by ~3 dB. In addition, by increasing the link span from 5 to 10 m, the power penalty is ~3 dB. This is because at very low light environment, the intensity of received light is close to the nonlinear region of the camera and since the footprint shrinks as the link span increases, the nonlinearity affects the signal less in longer link spans.The thesis states that the focal length and focusing distance of the camera does not make a significant impact on the performance of the system. Therefore, the camera can have a large field of view with a wide-open aperture. In addition, the thesis demonstrates that the ZF-based detection schemes outperform the HS/EGC schemes under severe level of interference. It is shown that, in ZF-based cases the normalized height of the eye diagram in is 70% higher compared to HS/EGC when the spacing between Txs is double the height of them.

Table of Contents

List of Figures

List of Tables

Glossary of Abbreviations

ACMA	Australian Communications and Media Authority
ACO-OFDM	Asymmetrically clipped optical orthogonal frequency division multiplexing
ADC	Analogue to digital converter
APD	Avalanche photodiode
APS	Active pixel sensor
BER	Bit error rate
CAP	Carrier-less Amplitude and Phase
CAPEX	Capital expenditure
CCD	Charge-coupled device
CDMA	Code division multiple access
CEPT	European Conference of Postal and Telecommunications Administrations
CFA	Colour filter array
CFL	Compact fluorescent light
CMOS	Complementary metal oxide semiconductor
COB-LED	Chip-on-board light emitting diode
CoC	Circle of confusion
CRTC	Canadian Radio-television and Telecommunications Commission
CSK	Colour shift keying
D2DC	Device to device communications
DCO-OFDM	DC-biased optical orthogonal frequency division multiplexing
DSRC	Dedicated short-range communications
DSSS	Direct sequence spread spectrum
DZFE	Direct detection zero forcing equalization
EGC	Equal gain combining
EMI	Electromagnetic interference
FCC	Federal communications commission

FDM	Frequency division multiplexing
FDMA	Frequency division multiple access
FEC	Forward error correction
FFT	Fast Fourier transform
FoV	Field of view
FPN	Fixed pattern noise
fps	Frames per second
FWHM	Full width half maximum
GaAs	Gallium arsenide
GDRV	Gaussian distribution random variable
HCCD	Horizontal charge coupled device
HS/EGC	Hybrid selection/equal gain combining
HS/MRC	Hybrid selection/maximal ratio combining
ICI	Inter-cell interference
IFFT	Inverse fast Fourier transform
IM	Intensity modulation
IS	Image sensor
ISI	Intersymbol interference
ITS	Intelligent transport service
LCD	Liquid crystal display
LDs	Laser diodes
LEDs	Light emitting diodes
Li-Fi	Light-fidelity
LOS	Line of sight
LSI	Linear shift-invariant
MIMO	Multiple-input multiple-output
ML	Maximum likelihood
MLSE	Maximum likelihood sequence detection
MOS	Metal-oxide semiconductor
MOSFET	Metal-oxide semiconductor field effect transistor

MRC	Maximal ratio combining
MU-MIMO	Multi-user multiple-input multiple-output
NASA	National Aeronautics and Space Administration
NLOS	Non-line-of-sight
NOMA	Non-orthogonal multiple access
NRS	Non-rolling-shutter
NRZ	Non-return-to-zero
OBU	On-board unit
OCC	Optical camera communications
OFDM	Orthogonal frequency division multiplexing
OFDMA	Orthogonal frequency division multiple access
OLED	Organic light emitting diote
OOK	On-off-keying
OSIC	Optimally ordered successive interference cancellation
PAM	Pulse amplitude modulation
PAPR	Peak to average power ratio
PD	Photodiode
PGA	Programmable gain amplifier
PIN	Positive-intrinsic-negative
PLED	Polymer light emitting diode
PMF	Probability mass function
PSK	Phase shift keying
QAM	Quadrature amplitude modulation
QR	Quick response
RB	Rectangular box
RF	Radio frequency
RGB	Red-green-blue
RRCF	Root-raised cosine filters
RS	Rolling shutter
RSU	Road-side unit

Rx	Receiver
RZ	Return to zero
S2PSK	Spatial-2-phase-shift-keying
SC	Selection combining
SD-FEC	Soft-decision forward error correction
SDM	Space division multiplexing
SDMA	Space division multiple access
Si	Silicon
SIC	Successive interference cancellation
SINR	Signal to interference and noise ratio
SMOLED	Small organic molecules light emitting diode
SNR	Signal to noise ratio
SPAD	Single-photon avalanche photodiode
TDM	Time division multiplexing
TDMA	Time division multiple access
THP	Tomlinson Harashima precoding
Tx	Transmitter
UFSOOK	Undersampled frequency shift on off keying
UPSOOK	Undersampled phase shift on off keying
V2I	Vehicle-to-road side infrastructure
V2V	Vehicle-to-vehicle
VANET	Vehicular ad hoc networks
VCCD	Vertical charge coupled device
VLC	Visible light communication
VLL	Visible light localization
VLPS	Visible light positioning system
WDM	Wavelength division multiplexing
ZF	Zero forcing
ZFE	Zero forcing equalization

Glossary of Symbols

a	Pixel length
A_{f}	Footprint area
A_{int}	Intersecting area
A_{f}	Area of the footprint of the Tx on the floor surface
A_{lens}	Aperture of the lens
A_{IS}	Image sensor area
A_{pixel}	Pixel area
A_{PD}	Photodiode area
b	Packet
B	Bandwidth
B_{PD}	Photodiode bandwidth
BER	Bit error rate
C	Capacitance
C_{ox}	MOS gate capacitance
CL	Confidence level
d	Payload data stream
$\hat{d}$	Estimated payload data stream
d_{c}	Distance from the element of surface to the camera
d_{t}	Distance from the element of surface to the Tx
$\mathrm{d}A$	Element of area on the floor surface
D	Distance between neighbouring Txs
D_{LED}	Distance between two light source in the Tx
D_{lens}	Diameter of the lens
E	Exposure
f	Camera focal point
f_{stop}	F-number of the camera

$Flag_{\mathrm{g}}$	Group flag
$Flag_{\mathrm{pi}}$	Pilot flag
$Flag_{\mathrm{pr}}$	Preamble flag
g	Gap between two pixels
g_{lens}	Gain of the camera lens system
$\mathbf{G}$	Matrix of preamplifiers gain
$h_{\mathrm{ch},u,v}$	Channel impulse response of (u, v)-th pixel
H_{c}	Height of the camera
H_{t}	Height of the Tx
H_{RB}	Height of RB
$\overline{\mathbf{H}}^{+}$	Pseudo inverse matrix of channel impulse response
$\overline{\mathbf{H}}^{\mathrm{H}}$	Hermitian transpose of channel impulse response
$\widetilde{\mathbf{H}}^{\mathrm{RGB}}$	Channel impulse response in the coloured JPEG frame
$\widetilde{\mathbf{H}}$	Channel impulse response in the grayscale JPEG frame
$\overline{\mathbf{H}}$	Channel impulse response in the grayscale JPEG frame after
$\mathbf{H}_{\mathrm{cam}}$	Matrix of camera impulse response
$\mathbf{H}_{\mathrm{ch}}$	Matrix of channel impulse response
$\mathbf{I}$	Matrix of inference
I_{ab}	Apparent brightness
$I_{\mathrm{b,th}}$	Threshold brightness
I_{b}	Magnitude of the brightness
I_{dark}	Dark current
I_{LED}	LED drive current
K	Boltzmann's constant
L_{mos}	Length of MOS gate
L_{s}	Link span
m_{r}	Lambertian mode number of reflection from floor surface
m_{t}	Lambertian mode number of Tx
M	Symbol per frame
$\overrightarrow{n_c}$	Unitized camera plain normal vector

$\vec{n}$	Unitized incident beam vector
$\overline{N_e}$	Mean number of photoelectrons
N_{g}	Number of groups
N_{pa}	Number of payload bits
N_{pi}	Number of pilot bits
N_{pr}	Number of preamble bits
N_{r}	Number of Rxs
N_{t}	Number of Txs
N_e	Number of photoelectrons
$\hat{\mathbf{n}}_{\mathrm{t}}$	Unit orientation vector
$\mathbf{N}$	Matrix of noise
$\widetilde{\mathbf{N}}^{\mathrm{RGB}}$	Noise of coloured JPEG frame
$\widetilde{\mathbf{N}}$	Noise of grayscale JPEG frame
$\overline{\mathbf{N}}$	Noise of grayscale JPEG frame after binning
P_{t}	Transmit power
q	Electron charge
r_{int}	Intersection ratio
$\mathbf{r}_{\mathrm{t}}$	Position vector of Tx
R	Resistance
R_{b}	Data rate
R_{r}	Radiation pattern of the floor surface
R_{t}	Radiation pattern of the Tx
$\Re$	Responsivity
S	Absolute value of the mean of preamble frames
S_{ISO}	ISO indicator
T	Temperature
T_{b}	Bit duration
T_{exp}	Exposure time
T_{fr}	Frame time
T_{res}	Reset time

th_{pa}	Threshold of payload
th_{pi}	Threshold of pilot frames
U	The number of rows in an image sensor
V	The number of columns in an image sensor
$\mathbf{w}$	Matrix of combining weights
$w_{\mathrm{eye},1}$	Height of inner eye
$w_{\mathrm{eye},2}$	Height of outer eye
w_{RB}	Width of RB
W_{mos}	Width of MOS gate
x	Modulated data
x_{c}	Camera location in the x direction
x_{op}	Optical transmit data
x_{t}	Tx location in the x direction
y_{c}	Camera location in the y direction
y_{t}	Tx location in the y direction
$\mathbf{Y}$	Matrix of frame
$\mathbf{Y}_{\mathrm{G}}$	Matrix of frame after gamma correction
$\widetilde{\mathbf{Y}}$	Grayscale JPEG frame
$\widetilde{\mathbf{Y}}_{\mathrm{pi}}$	Matrix of pilot frame
$\overline{\mathbf{Y}}$	Grayscale JPEG frame after binning
$\widetilde{\mathbf{Y}}^{\mathrm{B}}$	Blue component of JPEG frame
$\overline{\mathbf{Y}}^{\mathrm{e}}$	Even frames
$\widetilde{\mathbf{Y}}^{\mathrm{G}}$	Green component of JPEG frame
$\overline{\mathbf{Y}}^{\mathrm{o}}$	Odd frames
$\widetilde{\mathbf{Y}}^{\mathrm{R}}$	Red component of JPEG frame
$\widetilde{\mathbf{Y}}^{\mathrm{RGB}}$	Coloured JPEG frame
Z	Signal after combining
$\alpha_{\mathrm{f-c}}$	Channel loss from the element of area to the camera
$\alpha_{\mathrm{t-f}}$	Channel loss from the element of area to the Tx
$\Delta\overline{\mathbf{Y}}^{\mathrm{o}}$	Subtracted matrix of odd frames

θ_{r}	Emission angles of the reflection
θ_{t}	Emission angles of the Tx
θ_{tilt}	Elevation tilting angles
μ_0	Mean value of bit “0”
μ_1	Mean value of bit “1”
σ_0	Standard deviation of bit “0”
σ_1	Standard deviation of bit “1”
σ^2_{dark}	Dark current noise variance
σ_{res}	Standard deviation of reset noise
σ_{shot}	Standard deviation of shot noise
$\sigma^2_{\mathrm{thermal}}$	Variance of thermal noise
$\sigma_{b,x}$	Standard deviations in the x direction
$\sigma_{b,y}$	Standard deviations in the y direction
ψ_c	Incident angle of the camera
$\phi_{1/2}$	Half angle beam width
ϕ_{tilt}	Azimuth tilting angles
γ	Gamma factor
Γ	Heaviside step function
κ	Magnification factor of the camera
ρ	Reflection coefficient
ω	Angular frequency
$\oplus$	Modulo2 operator
$\otimes$	Convolution operator

Dedications

To the most important people in my life, my parents, family, wife and two children (I do not have any children, yet. I even do not have a wife.).

Acknowledgments

First, my deepest apology in case I have unintentionally missed anyone.

Second, I would like to express my thanks to Northumbria university for sponsoring me and providing an opportunity for me to study PhD.

Third, sincere special thanks goes to my principle supervisor Professor Zabih (Fary) Ghassemlooy for his advice, guidance, constant enthusiasm and support throughout this PhD journey. Without his unlimited support, this work would not has been accomplished on time.

Fourth, I would like to thank Professor Stanislav Zvanovec, Dr Hoa Le-Minh, Dr Mauro Biagi, Dr Anna Maria Vegni, Dr Pengfei Luo, Dr Mojtaba Mansour Abadi, Dr Andrew Burton, Dr Khald Werfli, and the rest of the colleagues and friends who helped me a lot throughout my journey.

Fifth, I specially thank Eat4Less and McDonald's, which were there whenever I needed them.

Finally, I specially thank Microsoft for creating a super powerful, yet horrible software like Word, which made me 10 years older since I decided to write my thesis in this platform.

Declaration

I declare that the work contained in this thesis has not been submitted for any other award and that it is all my own work. I also confirm that this work fully acknowledges opinions, ideas and contributions from the work of others.

Any ethical clearance for the research presented in this thesis has been approved. Approval has been sought and granted by the Faculty Ethics Committee / University Ethics Committee / external committee.

I declare that the Word Count of this Thesis is 33,179 words

Signature: 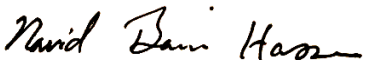

Name: Navid Bani Hassan

Date: 27th February 2019

Chapter 1 INTRODUCTION

1.1 Background

Applications of solid-state light emitting diodes (LEDs) for illuminations, indoor data communications and localization, as well as sensing have been growing over the last few years [1, 2]. Visible light communication (VLC) systems, which uses the LED-based lights installed in indoor and outdoor environments to provide wireless services, offers a potential licence-free bandwidth B orders of magnitude higher than the radio frequency (RF) technologies [2]. Line of sight (LOS) VLC systems employing LEDs and standard photodiodes (PDs) have been adopted in many applications in indoor environments offering high data rates R_{b} over a short transmission span (~10 m). However, LOS based links suffer from shadowing and limited user mobility [1]. Both mobility and shadowing can be addressed by adopting (*i*) multi-array transmitters (Txs) and receivers (Rxs) (i.e., increased complexity); and (*ii*) the diffuse system but at the cost of reduced R_{b}, see [1, 2] and the references within.

The wide spread use of smart devices equipped with LED based screen lighting, flashlight ,and quality cameras offer the opportunity to establish VLC links, where the flashlight and the camera can be used as a transceiver without the need for the additional hardware. The optical camera communications (OCC) offer new possibilities for the use of VLC systems in a number of applications including display based transmission, device to device communications (D2DC) - as part of the Internet of things, vehicular communications where the camera based Rx will offer multiple functionalities including vision, data transmission, localization and range measurement [1, 3-5]. In contrast to the single PD-based VLC systems, a camera based Rx in OCC, which is composed of an imaging lens and an image sensor (IS), has many unique features including a wide field of view (FoV) due to the PD array as well as spatial and wavelength separation of the light beams [6].

OCC can help intelligent transportation systems (ITS) mainly for transmission of safety warnings and traffic information, which can be effective for avoiding accidents and traffic congestion. Every year, road accidents cause ~1.2 million deaths and 50 million injuries around the world, which if it is not controlled, car accidents will become the third-leading cause of death by 2020 [7]. Cameras (i.e., a matrix of PDs) can be employed for object and people detection as well as collision warning, enhancing driving safety, range estimations and data communications in vehicle-to-vehicle (V2V), and vehicle-to-road side infrastructure (V2I) communications [6, 8, 9].

In this Chapter, we outline the concept of OCC and challenges associated with it as well as the need for this research work. The Chapter present the aims and objectives as well as outlines the original contributions made to this field of research. Also

presented are the thesis's structure, a list publications generated during the PhD research work and awards.

1.2 Problem Statements

Globally, approximately 1.2 million people die each year as a result of road traffic accidents [7, 10]. Moreover, with the introduction of autonomous vehicles, localization and communications between vehicles and the surrounding environment (i.e., the road side infrastructure, etc.) has become an essential part of future smart cities [11]. Within this context, ITS have been proposed as a means to support improving the traffic flow, reduce pollution and road accidents, reduced energy usage, and improve economical productivity and the quality of life [12-14]. ITS enables sharing of information between vehicles and/or vehicles and road infrastructures. The current ITS technologies are also known as the vehicular ad hoc networks (VANET), V2V or V2I communications, and are RF-based under the name of dedicated short-range communications (DSRC) [15]. In ITS, vehicles can communicate with each other without the use of cellular wireless base stations. The main features of VANET are safety, improved road usage efficiency and providing in vehicle information/entertainment [16-18].

There are a number of use cases for ITS considered in the standards, which generally fall into eight categories as bellows [19]:

- **Localisation:** The location information can be transmitted to the vehicles employing a number of road-side units (RSUs).

- **Electronic Parking Management:** In parking, this technology can be used for payment transactions.
- **Traffic Signal Control Management:** RSUs along the roads can collect the traffic information and use it for traffic management applications such as adaptive traffic-light phasing at the junctions. Besides, RSUs can give priority at the junctions to the emergency vehicles or the public transportation at traffic junctions.
- **Traffic Information:** Warning information such as road conditions, obstruction, low height clearance, road works, etc. as well as curve speed assistance, stop light assistance, and parking availability information can be transmitted using the RSU to the vehicles. Left turn assistant and lane change warning are other information that can be transmitted among cars using their on-board units (OBUs). Moreover, enhanced guidance and navigation, green light optimal speed advisory, and lane merging assistant signals are the essential part of the improved road usage efficiency [16].
- **Safety Application:** ITS also supports safety services such as intersection collision avoidance, platooning, pre-crash sensing, cooperative adaptive cruise control, and cooperative collision warning, which can be transmitted among vehicles.
- **Emergency Applications:** Live videos captured by DSRC devices can be sent to the control centre as a supporting evidence as required.
- **Kiosk Related Services:** Diagnostic data such as automotive repair records and firmware/software updates may be transferred through this service. Other applications such as ordering takeaway foods or purchasing fuel can use this service.

- **Other ITS Application and Services:** Pedestrians and cyclists can carry DSRC devices to alert other drivers when approaching an intersection or crossing roads.

ITS can help off-load data from the existing cellular communication systems, thus reducing the spectrum congestion in existing RF wireless systems [16, 20]. However, there is a number of drawbacks to RF-based VANET communications including:

(i) Sharing the same carrier frequency with a number of RF-based services such as fixed satellite and wireless services, mobile services, radiolocation, amateur radio, etc. Therefore, they may both experience and introduce interference [21, 22].

(ii) Incurring higher costs since a DSRC link will need RF OBU and RSU to be mounted on vehicles and roadsides, respectively.

(iii) Incompatibility with future systems and services. This is due to the fact that, the bandwidth of DSRC defined by regulatory agencies (i.e., Federal Communications Commission (FCC), European Conference of Postal and Telecommunications Administrations (CEPT), Australian Communications and Media Authority (ACMA), car-to-car consortium, and Canadian Radio-television and Telecommunications Commission (CRTC)) is about 70 MHz in the frequency band of 5.855-5.925 GHz, which may not be sufficient in the future [21-23].

(iv) Vulnerability to the so-called broadcast storm, where several vehicles transmitting at the same time that may lead to packet collision [24].

(v) Potential hazards to the environment and human health [25].

As a viable alternative solution, the VLC technology [26] could be adopted in V2V communications by simply using new lighting fixtures (i.e., front, back and internal) in new vehicles, which are based on LEDs, organic LEDs (OLEDs), or laser diodes (LDs).

In VLC systems, two types of detectors are commonly used: (*i*) PDs with a wide bandwidth B_{PD} (i.e., a few MHz to beyond a GHz depending on the PD's size), which is the most widely used due to their high-speed communications [5]; and (*ii*) ISs (i.e., multi-array PDs as in cameras with much lower data rates R_{b} [1, 3-5, 27]). Short range PD-based VLC systems offer higher R_{b} (up to 4.81 Gbps [28] compared to ~200 Kbps for a high-speed camera [29] and 55 Mbps for an optical communication image sensor [30]) at the cost of reduced mobility and an increased level of shadowing and blocking [1]. However, in indoor environments both mobility and shadowing have been addressed using multi-array Txs and Rxs and/or non-line-of-sight (NLOS) VLC links, but at much reduced R_{b} as a result of multipath induced dispersion in the case of NLOS link (see [1, 2] and the references within). Note that, in outdoor environments PD-based VLC system will suffer from the high level of ambient light (i.e., sunlight) induced noise, thus resulting in significant deterioration in the link's performance (i.e., signal to noise ratio (SNR) and the bit error rate (BER) [31].

Unlike PDs, complementary metal oxide semiconductor (CMOS) based cameras offer spatial separation of multiple Txs (i.e., sunlight, street light, vehicle lights, etc.), which is highly useful in VLC [1, 3, 4, 27]. Such systems also offer MIMO capability [3, 32] for use in indoor [33, 34] and outdoor [6] applications including ITS, indoor localizations and D2DC [35, 36]. In ITS, the MIMO feature of cameras can be exploited for collision warning, adaptive cruise control, enhancing driving safety,

people and object detection, range estimation, and data transmission in V2V and V2I communications [6, 8, 9, 37]. In addition, cameras can be used for multiple purposes such as vision, surveillance, biometric facial recognition [38], scene change detection [39], augmented reality [40] and positioning [41]. Nowadays, new vehicles come with at least two front and one rear cameras for the purpose of people and object detection, smart lighting (where the position of on-coming or can be estimated using the camera and the information is used for adjusting the front lights intensity and profiles in order to avoid dazzling) [42], parking, ranging, etc.

OCC-based ITS can be categorized into LOS and NLOS link configuration. LOS-based OCC for ITS has been extensively investigated in the literature [6, 9, 43-45]. However, in some scenarios, the Txs may not be within the field of view (FoV) of the LOS path or the LOS link might be blocked, which requires communications via NLOS paths – an obvious option [27, 46]. Below are some examples for transmitting localisation, traffic information, road conditions, road works, obstruction, collision warning, pre-crash sensing, accident reports, etc. via the NLOS link:

- Vehicles approaching a road junction or a crossroad from different directions, where there is no LOS link between them.
- Vehicles travelling in the same direction, which are not in the FOV of neither the front or rear camera of each other. Hence, the need for vehicles to send information for lane changing.
- Heavy good vehicles blocking the LOS link between the vehicle and roadside lights.
- In urban areas, tall trees, especially in the spring and summer, may block the LOS link between the streetlights and the vehicles. In this case, the

[8]information about vehicles approaching a junction and cyclists or pedestrians crossing the road is achievable via a NLOS link.

- In indoor car parking areas, the lights might be behind a wall or be blocked by indoor signs and fixtures, which sends the information about the parking availability.
- Tall streetlights not in the FoV of the vehicles, especially at roundabouts and urban areas, therefore unable to transmit the information about the traffic conditions, emergency vehicles, etc.
- In heavy traffic road condition, where the LOS between cars might not be available, therefore reflections from the road surface may be the option to establish communications.

In NLOS links, the reflected optical beams normally have a large illumination footprint, thus offering an increased level of mobility and link tolerance to the cameras' movements but at the cost of reduced detected power level at the Rx, thus leading to higher BER. Enabling the OCC system to establish a link via NLOS along with a LOS path reduces the probability of outage, increases the reliability, improves the quality of service, and gives more flexibility in the design of the lighting fixtures, etc.

Note that, in some countries vehicles head and are on while on the road for improved visibility, thus making V2V communications possible at all times. However, with the streetlights being off during the daytime, V2I communications is no possible. One possible solution would be to use a hybrid infrared/OCC system [47], where the streetlights should have both infrared and visible LEDs or lasers but at a cost of a considerable capital expenditure (CAPEX). Therefore, during the daytime with the available technology, the information that was supposed to be broadcasted by

streetlights will be offloaded to V2V links and at nighttime the process is reversed. Thus, in this thesis we are more interested in providing the NLOS link during the nighttime to improve the quality of service.

In addition, there are a number of challenges in IS-based VLC links, which is also known as OCC, as outlined below:

1- *Detection and tracking of the Txs*: Given that the Txs is positioned within the captured image by the camera, a number of detection schemes have been proposed such as frame subtraction in LOS [30, 35] and NLOS [48], block matching [36], and vision-based image processing [49, 50].

2- *Limited data rate*: In OCC, the data rate is limited by the frame rate of the camera (typically 60 frames per second (fps)), which is very low from data communications, therefore not suitable in applications where high data rates is the main requirement such as Internet access. However, in the CMOS-based IS technology, the quality of captured videos using modern digital cameras has improved significantly. Cameras in new smartphones can record video streams up to an R_{f} of 960 fps at a resolution of 720p [51]. In addition, there are commercially available high-speed cameras with R_{f} of 25.7 kfps and 1 Mfps at resolutions of 1280×800 and 128×32, respectively [52]. In addition, in [6], a CMOS IS with a data capture rate of 20 Mb/s/p was reported. Moreover to increase R_{b} (i.e. > R_{f}) the rolling shutter (RS) has been used [53]. In [54], a novel multi-level intensity modulation was used to achieve R_{b} of >10 kbps using a RS camera with $R_{\mathrm{f}} = 30$ fps at a distance of 2 m. In [27] and [55], RS cameras were employed in a NLOS OCC to detect the fast changing intensity of reflected lights

in an indoor environment. However, these systems have a number of problems including a complex detection mechanism and a limited link span L_s of up to 1.5 m [55]. Note that, VLC links with low R_b can be effectively used in a number of applications such as ITS, indoor visible light localization (VLL), sensing, etc., where high R_b is not a requirement [1].

3- *Flickering*: is an effect that takes place as a result of low-frequency changes in the intensity of the Tx. To address this problem, high-speed cameras or the RS effect can be used to increase R_b. In [56] and [57], an under-sample frequency and phase shift OOK modulation technique was investigated, respectively for OCC with low-speed cameras in order to increase the frequency of alteration between low and high signal to 120 Hz.

4- *Multiple access and multiplexing*: This refers to the case where signals from independent sources are combined at the Rx, which leads to interference. In [50], a space division multiplexed system was demonstrated for an OCC LOS link at a distance of 120 m and R_f of 1000 fps. In [58], colour-shift keying and code-division multiple access schemes were proposed for OCC at a distance of 50 cm and $R_b = 15$ bps, which employed Tx and Rx modules with increased levels of complexity.

1.3 Aim and Objectives

This research aims to conduct a comprehensive theoretical and experimental investigation of an NLOS OCC VLC system using LEDs and a camera in order to

transmit road safety, traffic, electronic parking, and localisation information. In order to achieve this, a list of research objectives are outlined as follows:

- Comprehensive review of the fundamental concepts of OCC systems, and outline the key technical challenges associated with OCC.
- Review the basics of cameras within the context of OCC and develop a comprehensive channel model for a NLOS OCC system.
- Develop a dedicated experimental test-bed (i.e., prototype) for the NLOS OCC system.
- Propose a novel packet structure and a data extraction method for OCC.
- Evaluate experimentally and numerically the performance of the proposed schemes in terms of BER under different camera settings such as ISO, exposure time, aperture size, and defocusing, and different channel conditions.

1.4 Original Contributions

As outcomes of the conducted research, the following original contributions have been made to the research field:

1. Proposing a unique packet structure and a novel extraction method for a MIMO NLOS OCC system based on hybrid selection/equal gain combining (HS/EGC), hybrid selection/maximal ratio combining (HS/MRC), differential signalling and frame subtraction (see Chapter 4).
2. Investigating the impact of channel and camera parameters on the performance of the system (see Chapter 4).

3. Proposing a comprehensive theoretical channel model for an NLOS OCC system (see Chapter 4).
4. Proposing a unique packet structure, space-time division multiplexing scheme, and a detection method for NLOS OCC for increased level of interference between the neighbouring Txs (see Chapter 5).
5. Proposing two detection methods for NLOS OCC based on zero-forcing equalization and comparing the results with HS/EGC (see Chapter 6).

These original contributions are further summarised in Fig. 1.1. The green boxes show what has been carried out in this work within the context of VANET.

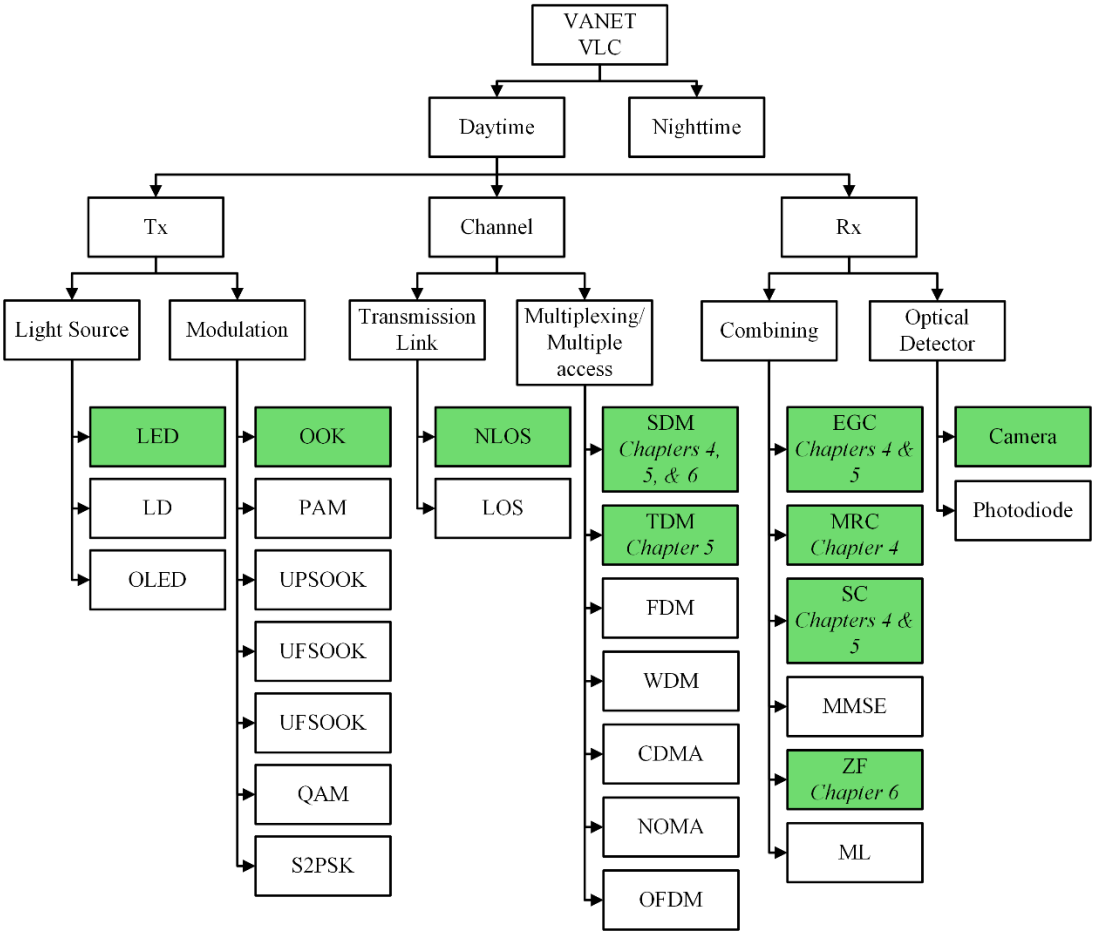

Figure 1.1: VLC domains in the ITS.

1.5 Thesis Structure

This thesis is arranged into seven chapters. Chapter 1 highlights the challenges in ITS and OCC, as well as the research motivations and objectives. Chapter 2 outlines a literature review on the recent works and achievements in VLC-based ITS systems, including the channel model, the Tx and the Rx. Chapter 3 covers the literature review on different parts of OCC block diagram. The advance modulation techniques for OCC is reviewed. A theoretical model for LOS channel is given followed by detailed structure of a typical camera including the lens system and the IS. The structure of ISs for both charge-coupled device (CCD) and CMOS sensors, as well as two types of ISs also are discussed in terms of their exposure to light. The Bayer pattern for coloured ISs and the method to change coloured images into grayscale are also discussed. In addition, the parameters related to the exposure, such as exposure time, ISO, and aperture, are presented, and the impact of them on the quality of the picture is discussed. Furthermore, a non-linear conversion method, called gamma correction, is reviewed. Next, the noise in ISs is studied and finally, different combining methods used in OCC is reported. In Chapter 4, a comprehensive theoretical channel model for an NLOS OCC system is proposed. Then, a novel packet structure and detection scheme based on HS/EGC and HS/MRC and frame subtraction is suggested in order to extract information from a video stream in a $2 \times N$ MIMO NLOS OCC system. Furthermore, a practical investigation of the performance of the proposed system is presented under different channel conditions and camera settings. In Chapter 5, in order to reduce the interference level, a space and time multiplexing technique along with a unique packet structure is proposed and the proposed method was experimentally investigated for different link spans and under different ambient light

level. In Chapter 6, two detection techniques are proposed based on zero-forcing equalization for a MIMO NLOS OCC system. An experimental setup for the proposed techniques is presented and the results are compared with the algorithms in Chapters 4 and 5. Finally, Chapter 7 concludes the thesis by providing a summary of all key findings, as well as some recommendations for future work on OCC.

1.6 Publications and Awards

1.6.1 *Journal*

1. **N. Bani Hassan**, Z. Ghassemlooy, S. Zvanovec, M. Biagi, A. M. Vegni, P. Luo, M. Zhang, "Non-Line-of-Sight MIMO Space-Time Division Multiplexing Indoor Optical Camera Communications Employing Equal-Gain Combining," Journal of Lightwave Technology (JLT), Vol. 37, No. 10, pp. 2409-2417, May 2019.

2. **N. Bani Hassan,** Z. Ghassemlooy, S. Zvanovec, P. Luo, H. Le-Minh, *"Non-Line-of-Sight 2 × N Indoor Optical Camera Communications"*, Applied Optics, Vol. 57, no. 7, pp. B144-B149, Mar 2018.

3. K. Werfli, P. Chvojka, Z. Ghassemlooy, **N. Bani Hassan**, S. Zvanovec, A. Burton, P. A. Haigh, *"Experimental Demonstration of High-Speed 4 × 4 Imaging MIMO Visible Light Communications Employing Multi-CAP"*, Journal of Lightwave Technology (JLT), VOL. 36, NO. 10, MAY 15, 2018.

4. S. VÍTEK, J. LIBICH, P. Luo, S. Zvanovec, Z. Ghassemlooy, **N. Bani Hassan**, "*Influence of camera setting on vehicle-to-vehicle VLC employing*

undersampled phase shift on-off keying", Journal of Radioengineering, Vol. 25, No. 1, April 2016.

1.6.2 *Conference*

1. **N. Bani Hassan**, Y. Huang, Z. Shou, Z. Ghassemlooy, S. Zvanovec, M. Zhang, "Impact of Camera Lens Aperture and the Light Source Size on Optical Camera Communications", in Communication Systems, Networks and Digital Signal Processing (CSNDSP), June 2018, Budapest, Hungary.
2. Sturniolo, **N. Bani Hassan**, Z. Ghassemlooy, S. Zvanovec, "ROI Assisted Digital Signal Processing for Rolling Shutter Optical Camera Communications", in Communication Systems, Networks and Digital Signal Processing (CSNDSP), June 2018, Budapest, Hungary.
3. **N. Bani Hassan**, Y. Huang, Z. Shou, Z. Ghassemlooy, S. Zvanovec, M. Zhang, "Impact of Defocusing of the Camera Lens on the Image in Optical Camera Communications", in West Asian Colloquium on Optical Wireless Communications (WACOWC), April 2018, Isfahan, Iran.
4. K. Werfli, P. A. Haigh, Z. Ghassemlooy, **N. Bani Hassan**, S. Zvanovec, "A new concept of multi-band carrier-less amplitude and phase modulation for bandlimited visible light communications", in Communication Systems, Networks and Digital Signal Processing (CSNDSP), June 2016.
5. R. Bates, C. Geldard, **N. Bani Hassan**, A. Burton, P. Luo, "Comparison of LED illumination patterns for camera based car to car communications", in Communication Systems, Networks and Digital Signal Processing (CSNDSP), June 2016.

1.6.3 *Awards*

1. Received a full scholarship from Northumbria University (2015-2018)

2. Received a Travel Grant from Intel-NTU IoX Center (2017)
3. Won the Best Paper Award in the West Asian Colloquium on optical wireless communications (2018)

Chapter 2 VISIBLE LIGHT COMMUNICATIONS FOR ITS

2.1 Introduction

Light was one of the earliest means of communication employed by humans since ancient times. In Iliad, Homer, the ancient Greek poet [59], reported the use of optical signals to announce the fall of Troy in ~1200 BC. Furthermore, Anabasis, the famous book of the Ancient Greek professional writer Xenophon, indicates that the same technique was used between Perseus and the army of Xerxes in ~440 BC. Furthermore, ancient Greeks polished their shields to reflect the sunlight as a means of providing signs to other soldiers in wars. Ancient Romans also used polished metals as mirrors to transmit information over long distances. Later, the Romans placed watchtowers on top of mountains all over the Roman Empire to transmit optical signals. Moreover, in 150 BC, native Indian Americans used smoke to communicate over very long distances. In recent times, the use of light beams to transmit information has become more advanced. In 1792, Claude Chappe created the first optical telegraph network, which enabled transmission of 192 different symbols using two arms connected to a

crossbar. The next version of the optical telegraph used sunlight or oil lamps to flash light messages encoded via Morse code, which was widely used by Navy ships for navigation. In 1880, Alexander Graham Bell invented the photophone, which could transmit voice signals on light carriers (see Fig. 2.1) [60]. In his setup, a vibrating mirror at the transmitter modulated the voice signal onto light carriers, while a crystalline selenium cell located at the focal point of a parabolic mirror at the Rx converted the light beams to electrical signals. With the development of the positive-intrinsic-negative (PIN) PDs in late 1950 and the invention of the p-n junction infrared LED using gallium arsenide (GaAs) in early 1960, a revolution in the telecommunication industry started.

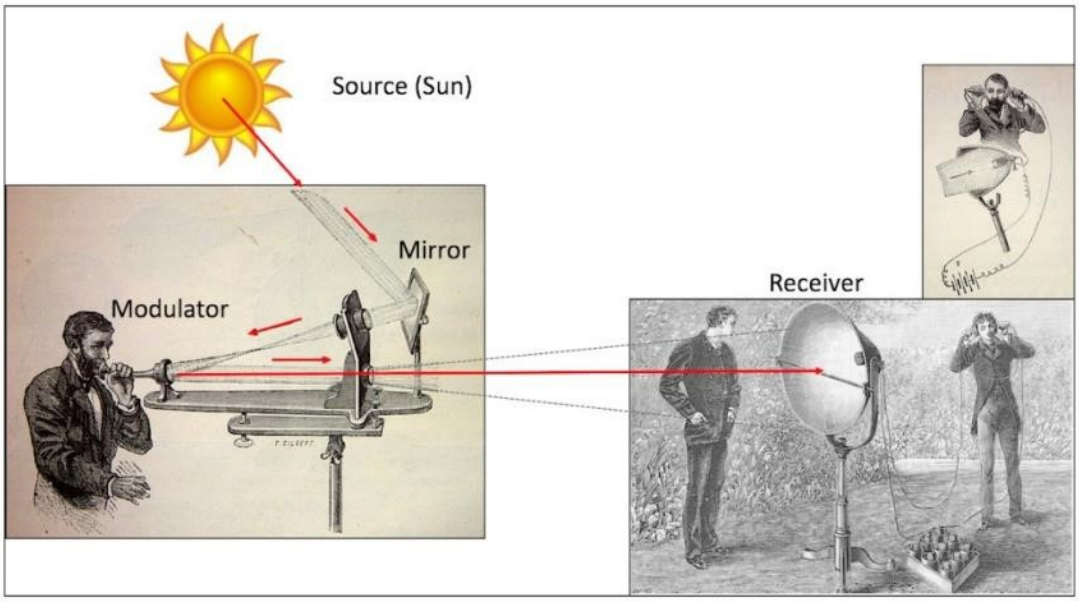

Figure 2.1: The concept of the photophone introduced by A. G. Bell. The sunlight is reflected on a modulator, the output of which is transmitted over a wireless channel and received by a photo-collector Rx [61].

Due to the ever-growing wireless networks and demand for higher bandwidths, the congested frequency spectrum in the RF region has become insufficient. As discussed in Chapter 1, in the DSRC standard set for RF-based car-to-car communications, the frequency spectrum is shared with fixed satellite and wireless services, mobile

services, radiolocation, and radio amateur services. VLC being license free, directional, and short ranged, is an ideal alternative for multi-hop car-to-car communication environment. The new generation of cars are equipped with LED head and taillights, as well as front and rear cameras, which reduces the CAPEX for car industries to establish a communication link. Both head and taillights are directional with a maximum intensity pointing towards the road direction (i.e., the transmitter light has little interference with other optical Rxs outside the road or roadside). VLC is a technology that can be utilized to ease the pressure on RF spectrum and let it be used for more efficient and effective applications. Furthermore, VLC can offer multiple functionalities simultaneously such as data communications, localization, and illumination. The other advantages of VLC over the already mature technologies such as RF communications are:

1- **Licence free**: There is no licences fee for using the light spectrum.

2- **High bandwidth**: Using micro-LEDs and PDs, multi-Gbps VLC links have been reported in [62], and [63].

3- **High transmission security**: Since light is highly directional and is confined within a closed environment, therefore eavesdropping is considerably more difficult in VLC compared to the RF systems, thus offering inherent security at the physical layer in contrast to the RF based wireless technologies.

4- **Green and available technology**: VLC takes advantage of the off-the-shelf LEDs, which are highly energy efficient (more than 50%) compared to the traditional lights and are used for illumination.

5- **No electromagnetic interference (EMI)**: VLC systems do not suffer from RF induced EMI and do not introduce interference to other wireless communication systems.

6- **Broad frequency spectrum**: The visible light spectrum band is broad within the range of 380 – 780 nm, see Fig. 2.2 [61].

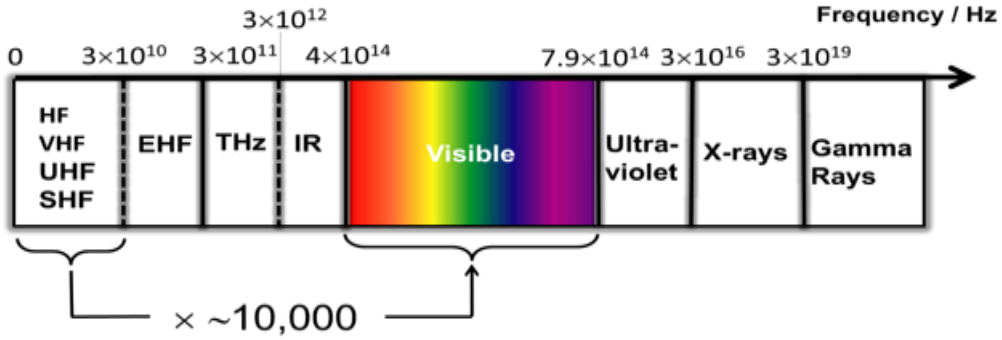

Figure 2.2: The electromagnetic spectrum showing the visible light spectrum band, which is 10000 higher than the RF band [61].

In this Chapter, a typical VLC system for ITS is presented. Popular modulation schemes used in VLC is reviewed and advances in light sources in the literature as well as industry as well as typical arrangements and requirements for streetlights are discussed. The channel model of the ITS system including the road surface and the impact of channel impairments such as turbulence, fog, rain, and ambient light is covered. Moreover, the typical Rxs used in VLC is reviewed and the main noise sources are discussed.

2.2 VLC System

Figure 2.3 depicts a typical system model for VLC. The intensity modulated light beam is transmitted through a free space channel (i.e., LOS, NLOS, or a combination of the two). On the Rx side, the information is captured using an optical Rx and processed in order to recover the transmitted data.

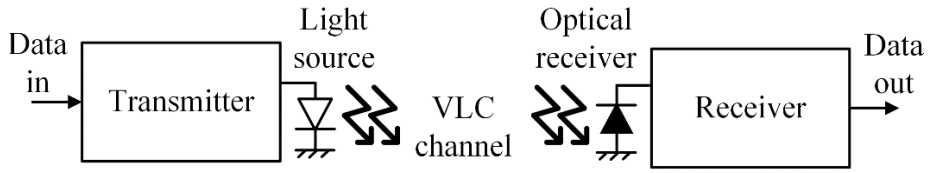

Figure 2.3: Typical VLC system block diagram.

2.2.1 *Transmitter*

2.2.1.1 ***Modulation***

In VLC, the information is carried on the intensity of the light (i.e., the optical carrier signal), which is unipolar and real-valued. The popular modulation schemes adopted in VLC are outlined as follows:

- **On-Off-Keying non-Return-to-Zero (OOK-NRZ):** which is the simplest modulation scheme, in VLC where the low and high states represent bits "1" and "0". The simplicity of implementation has made OOK-NRZ a very popular candidate for modulation among researchers. In [64], OOK-NRZ along with a pre-equalizer at the Tx was employed achieving a spectral efficiency of ~2 bit/s/Hz for the forward error correction (FEC) limit of

3.8×10^{-3}. Note that, OOK with a return to zero (RZ) format can also be adopted in VLC but at the cost of doubling the bandwidth requirement compared to the OOK-NRZ.

- **Pulse Amplitude Modulation (PAM):** which is a multi-level modulation in order to increase the spectral efficiency. In M-PAM, where $M = 2^m$ levels of intensities are used to represent m bits. Accordingly, the spectral efficiency can be improved by m times compared to OOK-NRZ. 8-PAM and wavelength division multiplexing (WDM) together with phase shifted Manchester coding and hybrid time frequency domain equalizations have been used to transmit data at rates of 3.375 and 4.05 Gb/s in [65] and [66], respectively. A spectral scrambling technique was proposed in [67] by employing 8-PAM with a data rate of 1.08 Gb/s over a 1.2 m transmission distance.
- **Orthogonal Frequency Division Multiplexing (OFDM):** is a multi-carrier modulation scheme where each carrier is orthogonal to the others during a symbol period. Each subcarrier can be modulated independently and hence can exploit the out of band frequencies of the LEDs. Since signals in VLC are unipolar and real, the complex and bipolar OFDM modulated signals cannot be directly sent through a VLC channel. Therefore, in optical OFDM, following mapping the signal on quadrature amplitude modulation (QAM) constellations, Hermitian symmetry is employed before inverse fast Fourier transform (IFFT) in a way that a complex conjugate version of the subcarriers is considered for the negative frequencies [68]. In order to make the signal unipolar, two popular techniques of DC-biased optical OFDM (DCO-OFDM) and asymmetrically clipped OFDM (ACO-OFDM) are used.

In [69], it is demonstrated that in a multi-user MIMO (MU-MIMO) system, ACO-OFDM is more efficient than DCO-OFDM under low optical power conditions. It is also shown that, at the average emitted optical power of 0 dB and for 25 subcarriers DCO-OFDM can reach a spectral efficiency of >15 bit/s/Hz. One of the drawbacks with OFDM is the high peak to average power ratio (PAPR). Since the dynamic range (i.e., power-current relationship) of LEDs is limited, higher PAPR results in clipped signal, hence reduced performance. A data rate of 5.04 Gb/s and a spectral efficiency of 4.2 bit/s/Hz with a soft-decision FEC (SD-FEC) limit of 2.4×10^{-2} was experimentally achieved over a 5-m free space link span for a 450 nm blue LD with a bandwidth of ~1 GHz in [70].

- **Carrier-less Amplitude and Phase (CAP):** is another multi-carrier modulation scheme, in which the signal after QAM mapping is filtered by in-phase and quadrature root-raised cosine filters (RRCF) and for demodulation matched filters are deployed. By introducing multiple passband RRCF with different central frequency, an m-subcarrier CAP (m-CAP) modulation can be realized, which is more tolerant to non-flat LED frequency responses [71]. The advantage of using m-CAP over OFDM is lower PAPR and the relaxed requirement to have IFFT and fast Fourier transform (FFT) blocks, hence a simpler implementation [72]. It is shown that, at a transmission distance of 1 m, the spectral efficiency of 10-CAP can reach 4.85 b/s/Hz [73]. This has enhanced to 23.25 b/s/Hz using a 4×4 MIMO system at a signal bandwidth of 5 MHz [74].

From the aforementioned modulation schemes, OOK-NRZ and PAM can be adopted in OCC, whereas due to high PAPR and non-linearity of the camera, OFDM

and CAP are not the most suitable options. In this thesis, we have adopted the OOK-NRZ modulation scheme for ITS applications, which can be changed to PAM as part of the future works. In Chapter 3, modulation schemes for OCC proposed in the literature are reviewed.

2.2.1.2 ***Light Source***

Conventionally, incandescent, mercury vapour, metal halide, high-pressure sodium, low pressure sodium, fluorescent, compact fluorescent and induction lamps have been used for lighting. In comparison, LEDs have longer lifetime of at least 50000 hours [75], higher luminous efficiency of ~100 lumens/watt [76], a wide range of colour, higher colour rendering index and faster switching time. In addition to illumination, LEDs provide the extra capability of encoding data onto the light carriers at a very high speed. In the past two decades, numerous research studies have been carried out in VLC employing visible LEDs as transmitters (Txs) and PDs as the Rxs [1]. The applications of VLC can range from indoor systems such as light-fidelity (Li-Fi), D2DC and localization to outdoor systems such as car-to-car communications.

The beam profile of the LEDs normally follow a Lambertian pattern. Lambertian surfaces are defined as emitting or scattering flat surfaces whose radiance is uniform in different directions [3]. However, based on Federal Motor Vehicle Safety Standards [77] and United Nations Economic Commission for Europe, the headlamps of cars do not follow Lambertian model [78]. These regulations are set to ensure that car's headlights illuminate the road surface while not dazzle other drivers. The headlamp usually has two levels of high and low beams, where the former is used to illuminate long distances in the absence of oncoming cars, and the latter is utilised for

illumination of short distances with minimum dazzling of the oncoming cars. Figures 2.4 and 2.5 illustrate the iso-candela and iso-illuminance diagrams of a road surface of a market-weighted pair of headlamps with a spacing of 1.12 m and at a height of 0.62 m, respectively for high and low beams [79]. The high beam has a very narrow illumination pattern projected horizontally, while the low beam is wider, asymmetrical and projected with an angle towards the road surface to avoid dazzling of the other drivers.

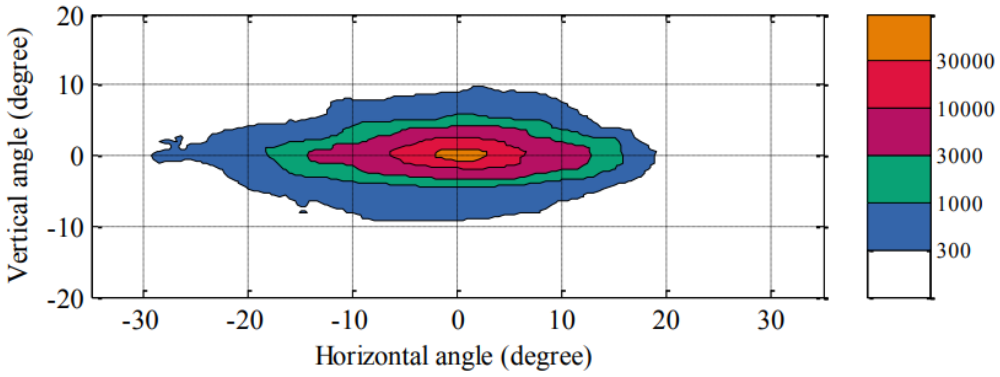

(a)

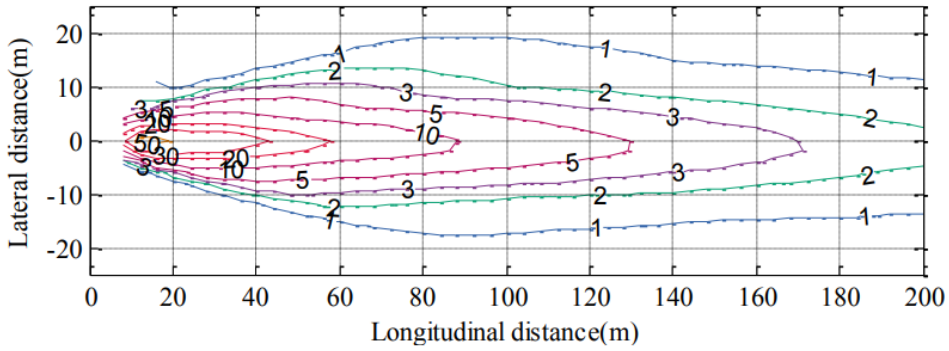

(b)

Figure 2.4: (a) Iso-candella and (b) iso-illuminance patterns of a market weighted high beam headlight [79].

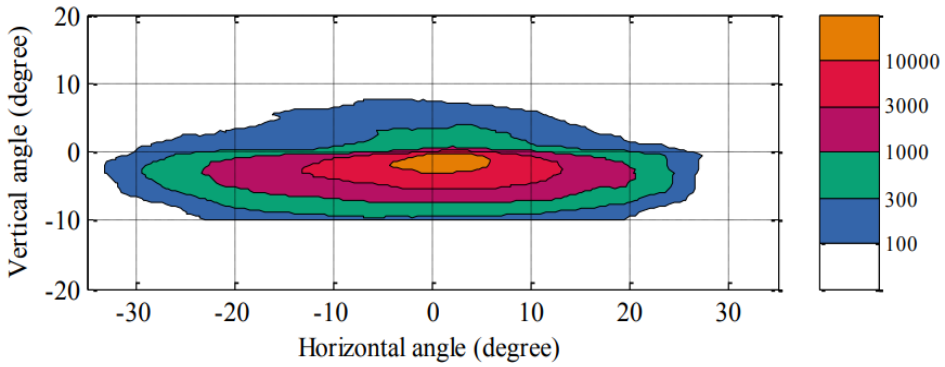

(a)

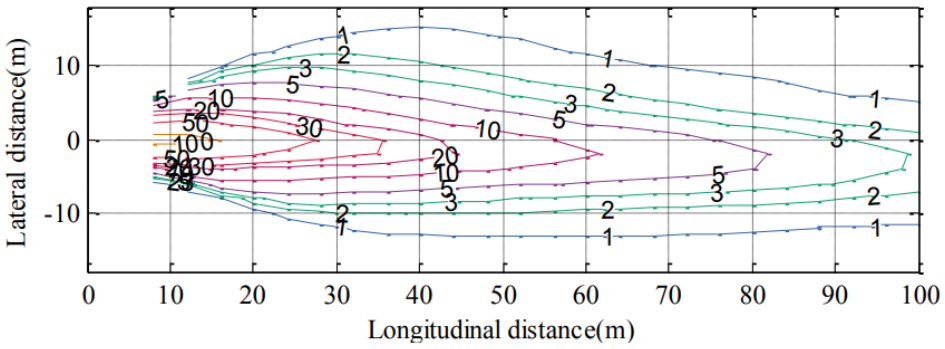

(b)

Figure 2.5: (a) Iso-candella and (b) iso-illuminance patterns of a market weighted low beam headlight [79].

Based on regulations set by the British government for street lights, the light poles should have a height of 6-12, 6-30, 8-10 and 12-18 m in small towns, city centres, motorways, and roads, respectively [80, 81]. Lighting falls into different classes based on the areas and applications. The ME lighting class refers to lighting of motorized roads with medium to high speed driving speed and the luminance level vary from 2 to 0.3 cd/m^2 for ME1 to ME6 classes, respectively. The CE lighting class represents the lighting for areas where vehicles have to expect other road users (e.g., pedestrians and cyclists) and areas such as complex road intersections, roundabouts, queuing areas, shopping streets, etc. In this class, the illuminance intensity is important and ranges from 50 to 7.5 lux for CE0 to CE5 class. S and A classes are related to lighting intended for the pedestrian and cyclists on footways, cycle-ways, pedestrian streets, emergency

lanes, residential roads, schoolyards, parking places, etc. The luminance level in the S class ranges from 2 to 15 lux [82]. In order to avoid light pollution, different types of street lights are defined depending on the vertical light distribution (see Fig. 2.6) as in [83]:

- **Full cut-off luminaires:** a maximum of 10% of the total lumens are emitted at the angles of >80º and <90º and 0% at >90º.
- **Cut-off luminaires:** a maximum of 10% of the total lumens are emitted at an angle of >80º and 2.5% at an angle of >90º.
- **Semi cut-off luminaires:** a maximum of 20% of the total lumens of the lamp is emitted at >80 and 5% at >90.
- **Non-cut-off:** the light emits to all directions.

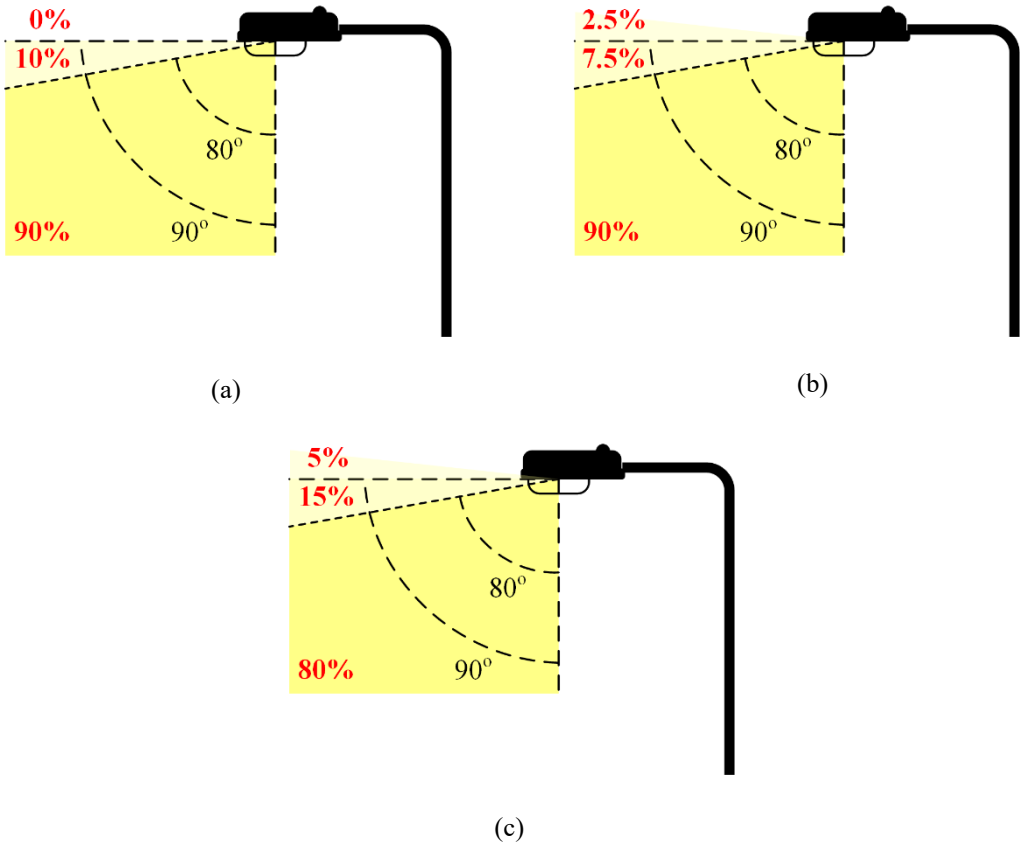

Figure 2.6: Definition of cut-off criteria: (a) full cut-off, (b) cut-off, and (c) semi cut-off [83].

In [84], a rectangular street light illumination is presented using two cylindrical spherical lenses to create a uniform illumination pattern on the road surface with a divergence-angle ratio of 7:3. The arrangement of streetlights depends on the geometry of the road, the ground condition of the road, the environmental requirements, physical characteristics of the mast, the space available for maintenance, the available budget, etc. [83]. The most common arrangements are single-sided, staggered, opposite, and central/twin central as shown in Fig. 2.7.

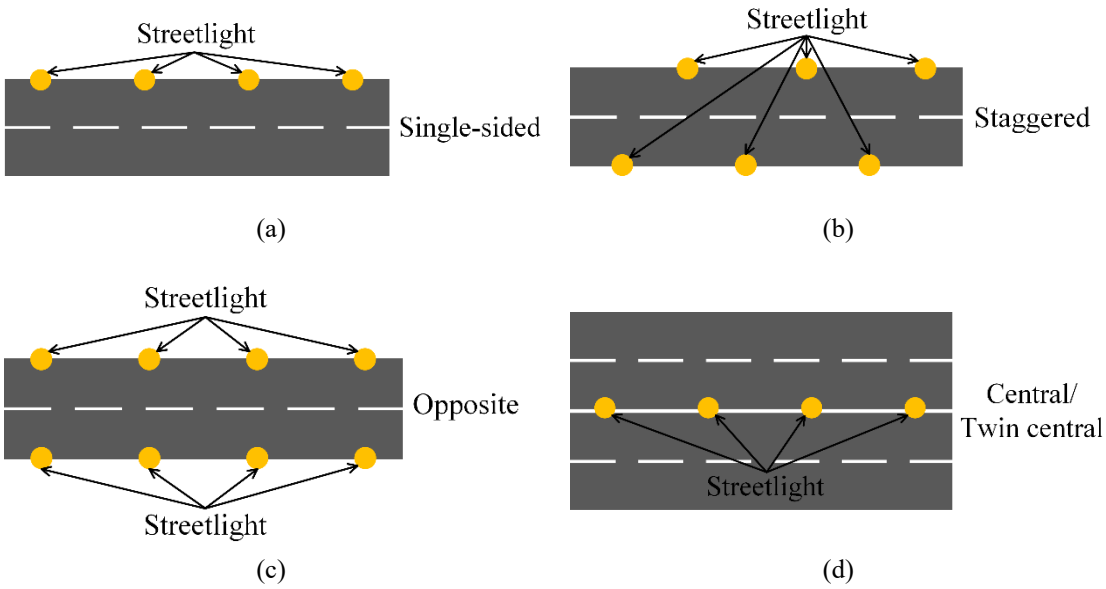

Figure 2.7: Arrangement of streetlights: (a) single-sided, (b) staggered, (c) opposite, and (d) central/twin central [83].

2.2.1.2.1 LEDs

LEDs are vastly being used for illumination as they are cost-effective, low power consuming, illumination efficient, compact in size and they require low maintenance cost. LEDs unlike traditional light sources such as compact fluorescent light (CFL) and incandescent bulbs can switch on and off at a fast speed, which makes it a viable option for communications [1]. Early versions of phosphor-based white LEDs, which are made of Gallium Nitride (GaN) semiconductors offer a modulation bandwidth

limited to several MHz, which is due to long response time of the yellow phosphor. Using blue filters [85] and pre-equalizations [64], the modulation bandwidth can be increased to ~20 MHz and 45 MHz, respectively. With the introduction of micro-scaled LEDs (μLEDs), the modulation bandwidth is increased further by orders of magnitude. In [86], a 72-μm LED with a bandwidth of 245 MHz, which is an order of magnitude more than standard white LEDs, was reported for a wavelength of 450 nm, while by decreasing the size to 44 μm the bandwidth increased to ~430 MHz [87]. Later, a bandwidth of >800 MHz for a 450-nm μ-LED was presented in [62] for VLC. Recently, a nonpolar InGaN/GaN μLED is proposed with improved bandwidth of 1.5 GHz [88], which is further extended to 2.5 GHz [63], which is the highest bandwidth reported for an LED to date. However, the drawback of the micro-LEDs is the low output intensity level for illumination. This means that for a typical room illumination a large number of LEDs (i.e., μ-LED array) will be required thus leading to increased cost, which could eventually reduce as more of these devices are used [89]. In the car industry, Lexus is the pioneer in using LED-based headlights in LS 600h L series, followed by Audi (R8 V-12 TDI series) [90]. Nowadays, most car manufacturers are considering the use of LEDs for both head and taillights.

2.2.1.2.2 Laser Diodes (LDs)

LDs with more converged emission and smaller size compared to LEDs, are a better option for high beam headlights for long-range illumination. LDs are particularly impressive due to their small size, where a single LD is much brighter light that a LED. The primary benefit for drivers is that these headlights will have the longest range provided by any current headlight technology. This offers the driver improved visibility, resulting in increased road traffic safety. In addition, LDs offer a narrower

spectral linewidth and higher modulation bandwidth than LEDs. With the current advances in the design of LDs, the modulation bandwidth can reach up to ~730 MHz for LD with an external cavity length of 19 cm [91]. In 2014, laser headlights were first adopted in BMW i8 series for an improved quality of illuminations (see Fig. 2.8). Compared to LED headlights, BMW laser lights are much brighter, which enhances the visibility from 300 m to 600 m and consume 30% less energy [92]. Following BMW i8, this technology was adopted in Audi R8 LMX, and BMW 7 series [93].

Figure 2.8: Laser headlights (right) offer increased visibility compared to LED headlights (left) [92].

2.2.1.2.3 Organic LEDs (OLEDs)

OLED, which is mainly made of long-chain polymers (PLED) or small organic molecules (SMOLED), is an emerging technology in the light industry. This technology is particularly used in displays as it provides an improved image quality in terms of contrast and colour range [94]. Besides, OLEDs can be made flexible, which is ideal for decorative lighting fixtures and where the light needs to be attached to a

non-flat surface. Recently, Royole introduced the world's first foldable screen called FlexPai with an OLED display [95]. Furthermore, OLEDs can be designed to be transparent in large proactive areas [96]. Although the illumination level and the luminous efficacy of typical OLEDs (i.e., 80-90 lm/W) [97] is comparably lower than to phosphor-based white LED (~160 lm/W) [98], RGB-based white LED (330 lm/W) [98] and phosphor-based white LD (~223.71 lm/W) [99], OLEDs are being used as a dazzle-free option for headlights in car industries. Audi proposed the OLED matrix taillight on TT RS series for the first time in its production line [100]. BMW is another pioneer, which has decided to equip the M4 GTS series with OLED taillights [101].

2.2.2 *Channel*

2.2.2.1 ***Surface Reflection***

In vehicular communications, the channel can be either LOS or NLOS. The NLOS cover reflections from road surface, walls, pavement, etc. Reflections can be classified into three general types; specular, spread, and diffused reflections (see Fig. 2.9). Specular reflections occurs in polished surfaces, where the incident light beam is reflected at the same angle. In rough surfaces, the incident light is reflected at more than one angle, causing what is known as spread reflection. Diffuse reflections, also known as Lambertian diffusion, happens when a light beam hits a matt surface and is reflected in all directions following a first order Lambertian pattern [102]. On road surfaces and pavements various conditions (e.g., dry, wet, icy, etc.) can cause reflections to be a combination of diffuse and specular [103]. Besides, the reflective coefficient of the road surface may vary depending on how long the road was being

used. To quantify the reflectivity of the pavement and road surfaces two parameters of average luminance coefficient Q0 and the mirror factor S1 as well as a reflection coefficient table also known as the *r*-table are used. As a general rule, higher Q0 indicates road being more matt whereas higher S1 means shinier road and more specularity [104]. Reflection coefficient is an effective indicator of the absorbance of the material, which is defined as the ratio of total luminance from an element of surface to the total illuminance from the same element of surface. For a typical asphalt road, this coefficient is 0.1 to 0.2 [105]. More details on the channel modelling for OCC systems will be given in Chapter 4.

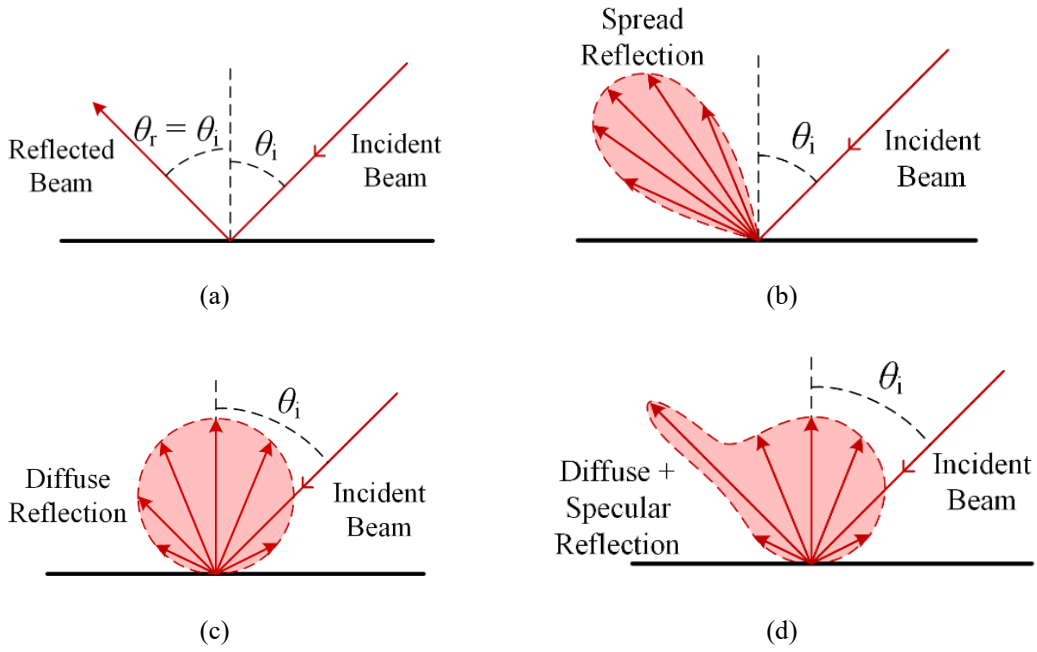

Figure 2.9: Reflection patterns from road surfaces: (a) specular, (b) spread, (c) diffuse, and (d) a combination of specular and diffuse.

2.2.2.2 ***Turbulence***

In outdoor environments, VLC is vulnerable to atmospheric conditions such as fog, haze, rain, snow, and atmospheric turbulence, also known as fading and scintillation.

Scintillation is temporal and spatial variation in the intensity of the received light beams. Scintillation can be a result of phenomena such as pressure and temperature gradients, which yield to random variation in pressure and temperature (hence different refraction indices) in the medium along the beam path. In outdoor VLC systems, this effect can be observed as heatwaves in hot sunny days or distorted images of distant objects. To model scintillation, log-normal for weak turbulences and Gamma-Gamma and K-distribution for strong turbulences are used [106]. In some outdoor applications, the channel may change slowly, hence sufficient time to estimate the channel state information accurately. In these scenarios, a symbol-by-symbol maximum likelihood (ML) [107] or ML sequence detection (MLSE) [108] can be employed provided that the marginal distribution of channel coefficient is known at the Rx. However, in C2C communications where the vehicles move at a relatively high-speed, channel will change rapidly. In order to mitigate the impact of fading, repetition coding (RC) is used in [106] for an outdoor MISO VLC system under a weak turbulence region, which could achieve a BER of 3.8×10^{-3} at SNR of ~8 using two Txs and coding block length of 101 bits. In this thesis, we consider a car to infrastructure NLOS scenario, which can function during the nighttime, as streetlights are on at nights or heavy overcast situations. In these scenarios, usually the floor surface is not hot enough to produce heatwaves. Therefore, in this work we do not consider the impact of turbulence on the proposed system.

*2.2.2.3 **Absorption and Scattering***

In the atmosphere, parameters such as snow and dense dust can absorb a part of transmit power, which results in reduced received power, hence SNR. Moreover, the

small water particles of rain and snow can absorb and scatter the light. More importantly, heavy fog can strongly reduce the received power through a combination of absorption, scattering and reflection, which can be observed as reduced visibility [109]. The impact of Fog on the SNR of the received signal is investigated in [110]. It is shown that, at visibility level of 50 m and a distance of 20 m, the path losses due to rain and dense fog are ~0.5 dB and ~3 dB, respectively. It is shown that, in a PD-based vehicular VLC system for OOK-NRZ and a transmit power of 10 dBm, the maximum distance to achieve a BER of 10^{-6} under conditions of clear, rain, and fog with a visibility of 50 m is ~72, ~69, and ~53 m, respectively. In [111], the impact of fog on vehicular communications is mitigated using multiple PDs with the help of a Fresnel lens and SC, which enabled the system to achieve a SNR of ~33 dB under a heavy fog condition over a link span of 1 m. In this work we only consider a road under clear condition. Outdoor cases with fog, rain, etc. will be considered as part of the future work.

2.2.2.4 ***Ambient Light***

The most significant problem in C2C VLC is the strong background noise caused by solar radiations during daytime or artificial lights during night time [112]. Note, the outdoor illuminance can vary from 120,000 lux for direct sunlight at noon to less than 5 lux for thick storm clouds. PDs may become saturated if they are in direct exposure to the sunlight, which leads to deterioration of the system performance as it blinds the Rx in capturing the modulated signals from Txs. However, in V2V and V2I VLC systems, the sun can only shine directly on a PD at the sunrise and the sunset [113]. Even if the PD is not saturated, the shot noise due to the ambient light can severely

affect the SNR of the link. To alleviate the impact of ambient light-induced shot noise, a solution is to reduce the FoV of the Rx. In [114], it was shown that this is possible for a FoV of 20º where a BER of 10^{-7} at a distance of 50 m was achieved. However, by reducing the FoV, the mobility decreases. The other approach is to use direct sequence spread spectrum (DSSS), which enables a communication over a link span of 40 m by expanding each bit to 10 bits, hence reducing in the data rate [115]. Since the streetlights are normally on during nighttime, the performance of the proposed system in this research work is limited to the nighttime. Therefore, we do not consider the impact of sunlight. However, the impact of artificial ambient light will be investigated in Chapters 5 and 6.

2.2.3 *Receiver*

In VLC systems, two types of detectors are commonly used at the Rx: (*i*) PDs; and (*ii*) image sensors (ISs) i.e., multi-array PDs as in cameras. This section gives an overview of each.

2.2.3.1 ***PDs***

Typical commercial silicon (Si)-based positive-intrinsic-negative (PIN) PDs can provide a 2 GHz of bandwidth for a photosensitive area A_{PD} of ~0.00785 mm^2 [116]. Higher bandwidth in PDs yields to smaller photosensitive area, hence reduced optical gains. On the other hand, due to limited Étendue of PD-based Rxs, with increase in the optical gain, the FoV decreases. In [117], a fluorescent antenna was used to boost the optical gain to 12 while maintaining a full-width half-maximum FoV at 120º. At a low intensity of light, PIN PDs do not offer the required SNR. Alternatively, avalanche

PDs (APDs), which have built-in first stage gain, can be employed under low illumination conditions. The commercial Si-based APDs with $A_{\mathrm{PD}} = 0.0314$ mm^2 can reach a bandwidth of 2 GHz at a wavelength of 700 nm offering a gain of 100 [118]. The other option is the single-photon avalanche PDs (SPADs), which works above the breakdown voltage and are capable of detecting a single photon. However, at the detection of a photon, the bias voltage across the SPAD drops. In order to detect the second photon the bias voltage needs to recover and hence the "dead time". In order to mitigate the "dead time", an array of SPADs has been employed [119]. However, the APDs and SPADs are very costly and require high bias voltage levels of ~100 and ~10 V, respectively. Besides, PD-based VLC systems are for short-range links and are complex to implement for multiple access-based schemes, and suffer from high-level of ambient light noise.

2.2.3.2 ***Cameras***

A cameras , on the other hand, are well-developed and cheap, which can be considered as a massive MIMO Rx, thus offering spatial separation of multiple light sources as well as spatial diversity [3], [4]. Buick was the first company, which employed a camera on Centurion XP-301 series in 1956, to give the driver a rear view of the vehicle [120]. Since then, many other manufacturers have used cameras to assist the drivers. Moreover, the luxury division of Nissan, Infiniti, for the first time employed cameras in the new technology called Omniview technology or Birdview on Infiniti EX35 SUV series, which assists the driver in parking with a 360$^{\mathrm{o}}$ view of the car. Now the car manufacturers are installing a dashcam to record while driving for accident and insurance purposes, parking, protection against the crash for cash frauds,

report dangerous drivers, capture and report road rage incidents and record driving memories. In addition, Mercedes-Benz has developed a technology based on stereo camera to detect the pedestrians and other obstacles within a range of 35 m in order to avoid accidents. Typical cameras have a low frame rate within the range of 30 to less than few thousand frames per second, hence a low speed Rx. However, with the imaging MIMO capabilities of the camera, higher order modulation schemes together with the RS effect can be effectively utilised in order to increase the data rate in OCC. Accordingly, since cameras are already available on most cars, they are a suitable option as Rx in low-data-rate road safety and traffic related applications as part of the ITS. Thus, in this thesis the camera-based Rx is investigated and is covered in details in Chapter 3.

2.3 Summary

In this Chapter, different parts of a VLC system, including Tx, channel, and Rx was discussed. The typical modulation schemes in VLC was reviewed. The regulations on the light sources in ITS was discussed and the advancements in the literature on LEDs, LDs, and OLEDs were reviewed. The NLOS channel in VLC-based ITS, which includes the road surface and the pavements, was introduced and characterized in terms of reflectivity. In addition, different types of optical Rxs with the current place in the car industry was discussed.

Chapter 3 OPTICAL CAMERA COMMUNICATIONS

3.1 Introduction

Following the introduction of the charge-coupled device (CCD) in 1969 by AT&T's Bell Labs for use in semiconductor memory devices, Michael Tompsett invented the CCD image sensor, which was the first electronic photography device. Later in 1975, the first digital camera built by Kodak had a CCD sensor with 0.01 megapixels image capability [121]. In the early 1990s, National Aeronautics and Space Administration (NASA) initiated a research on the employing CMOS technology as an architecture for imaging devices, which was commercialize as CMOS ISs in 1995 [121]. By 2005, almost all cameras were using this technology, thus the emergence of digital cameras. Nowadays, digital cameras with ISs containing a large number of micro-scale PDs are used for photography, vision, surveillance, motion detection, augmented reality [40], virtual reality [122], localization [123, 124], and data communications [125]. This development has led to the emergence of OCC, which has gained interests within the researchers [126] and is being considered as an option in IEEE 802.15.7m (TG7m)

visible light communication task group [127]. A number of applications for OCC in IEEE 902.11-17/0962r1 [128] have been proposed including indoor localization [129], digital signage [130], lighthouse-to-ship/ship-to-ship communications [131], and drone-to-drone communications for collision avoidance [132].

ISs are also used in C2C communications [6, 9, 43, 133]. ISs (or cameras), unlike PIN or APD PDs, are capable of differentiating the angle of arrival of light beams being received from different directions. As such, they provide a viable option to establish spatial division multiplexing in VLC [126]. In addition, in VLC systems, the level of interference using OCC is considerably lower than PD-based Rxs, which is particularly useful in C2C communications, where large number of mobiles and fixed optical Txs are in use. Moreover, due to longer sampling time and integrated high quality circuits, OCC offer relatively higher SNR compared to LiFi, which is beneficial in C2C communications with longer transmission ranges (i.e., tens of meters). The output intensity of head and taillights available in the market is limited, which limits the received optical power level at the Rx thus leading to a reduced transmission range or reduced data rates in PD-based VLC systems. However, ISs-based Rxs can overcome the power limitation by simply adjusting the exposure time, ISO, or aperture of the camera.

Accordingly, in this thesis, a camera is used as a Rx in C2C communications. In this Chapter, the modulation formats developed specifically for the OCC system are reviewed. Furthermore, the channel model for the LOS and NLOS based systems are reviewed and discussed. Also presented are the typical camera structure (lens and IS) and the parameters related to the exposure of the picture and gamma correction. Finally, the dominant noise sources in IS-based Rxs and the combining techniques adopted in OCC are discussed.

3.2 OCC

Figure 3.1 shows a block diagram of a typical OCC communications system. The input data $d_k(t)$ is modulated x_k prior to intensity modulation (IM) of the light source (i.e., LED). The modulated light beam x_{op} is transmitted over the free space channel. At the Rx side, the camera is used to capture images of intensity modulated LEDs in order to recover the data.

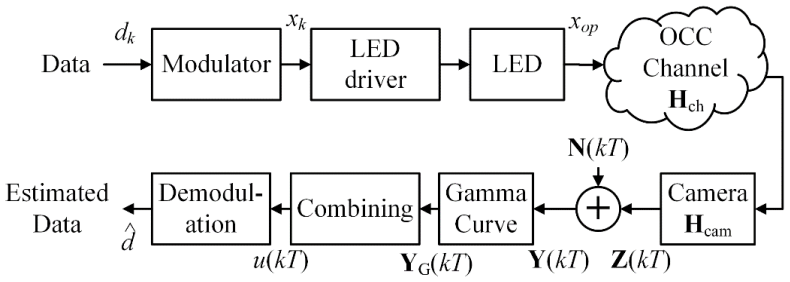

Figure 3.1: The block diagram of a typical OCC system.

3.2.1 *Transmitter*

The Tx is composed of the modulator, LED driver and LEDs.

3.2.1.1 ***Modulator***

The random data stream d_k is applied to the modulator, LED driver and LED in order for transmission over the OCC (i.e., free space) channel. In OCC systems with RS- and non-rolling-shutter (NRS)-based detection mechanisms, there are a number of modulation schemes that can be used. In [53], the simplest scheme of return to zero (RZ) or non-return to zero (NRZ) OOK based VLC with a data rate higher than the frame rate of camera was presented. In NRS-based OCC, the camera is only sensitive to the intensity of the light, as such advanced modulation techniques such as m-ary phase shift keying (m-PSK) and *m*-ary quadrature amplitude modulation (*m*-QAM) are implemented spatially.

Unlike in VLC, flickering is the major issue in OCC due to the low frame rate of the camera. One of the most popular techniques to avoid flickering is the under-sampled frequency shift OOK (UFSOOK) modulation scheme, which uses OOK with two different frequencies for two alternative sequences of '0' and '1' [56]. Note that, the camera samples either high or low intensity of the received signal provided the sample interval of less than one chip duration of the high frequency symbol. In contrast, the human eye do averaging over alternating symbols. A similar concepts known as undersampled phase shift OOK (UPSOOK) was proposed in [134], where the phase shift between two symbols was used to transmit data at double the data rate compared to UFSOOK. In [45], a spatial-2-phase-shift-keying (S2PSK) scheme was proposed for C2C communications. In this scheme, one taillight transmits an alternative sequence of '0' and '1', and based on the bit value of the data, the other taillight transmits the same sequence with a phase difference of '0' or '180' degrees. The advantage of this scheme are (*i*) flexibility of using cameras with variable frame rates; and/or (*ii*) using mismatch frequencies at the Tx and the Rx. In [135], an under-sampled-PAM scheme with a 50 fps camera was used to increase the modulation order and hence the transmission data rate to 250 bps. In addition, in [136], an under-sampled 1024-QAM scheme was demonstrated using two LEDs one each for the in-phase and the quadrature phase information of the QAM signal, where 32-PAM was used to generate 1024-QAM and a 50 fps camera was used to achieve a data rate of 500 bps for a 50 fps camera was achieved. Colour shift keying (CSK) modulation was demonstrated for a red-green-blue (RGB) LED to achieve data rates of 150 bps and 5.2 kbps in [4] and [137], respectively. In [138], a priority-based modulation scheme was proposed for traffic lights as part of ITS, employing a 2D fast Haar wavelet transform to modulate the data on different spatial components. As a result, high and

low priority signals with low and high data rates were transmitted over longer and shorter distances, respectively. In this thesis, OOK modulation, which is the simplest, is used for IM of the light sources (i.e., LEDs). However, the algorithms proposed in this thesis can be also adopted in other modulation schemes.

3.2.1.2 ***LED driver and LED***

The output of the modulator x_k (in Volts) is then applied to the LED driver for IM of the LED, see Fig. 3.2. The LED drive current is given by:

$$I_{\text{LED}} \cong \frac{x_k}{R_{\text{e}}}, \tag{3.1}$$

where R_{e} is the emitter resistor.

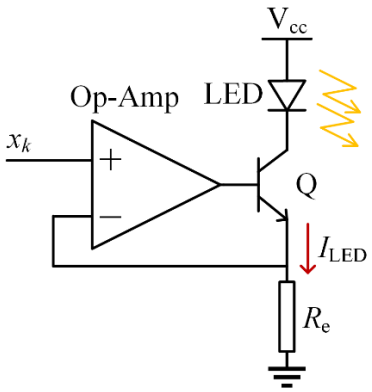

Figure 3.2: A typical voltage to current transducer used for driving LED.

A wide-beam optical source can be represented by a unit orientation vector , transmit power P_{t}, position vector $\mathbf{r}_{\text{t}}$, and radiation intensity pattern $R_{\text{t}}(\theta)$. For a uniaxial symmetrical light source, a generalized Lambertian radiation pattern model can be used, which is expressed as [139]:

$$R_{\text{t}}(\theta) = \frac{m_{\text{t}} + 1}{2\pi} \cos^{m_{\text{t}}}(\theta), \tag{3.2}$$

where $m_{\mathrm{t}} = \ln(2) / \ln\left(\phi_{\frac{1}{2}}\right)$ is the mode number of the radiation lobe. Figure 3.3 shows a Lambertian radiation pattern for different mode numbers.

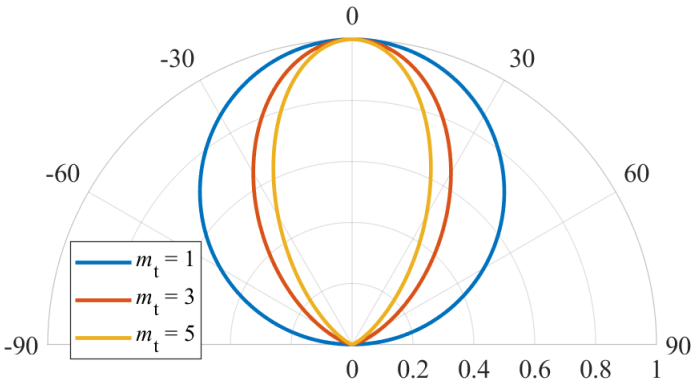

Figure 3.3: Lambertian illumination patterns.

3.2.2 *Channel*

In OCC, the transmission link can be LOS [9, 44, 45], NLOS [27, 140], or both. The channel impulse response for the LOS link can be represented as a matrix $\mathbf{H}_{\mathrm{ch}} = \left[h_{\mathrm{ch},u,v}\right]_{U\times V}$, where U and V are the number of rows and columns of the image sensor and $h_{\mathrm{ch},u,v}$ is the channel impulse response of the (u,v)-th pixel. Using a single LED and a Gaussian mixture model, $h_{\mathrm{ch},u,v}$ is estimated as [32]:

$$h_{\mathrm{ch},u,v} = A\sum_{k=1}^{v}\frac{\kappa^2 c_k}{2\pi\sigma_{x,k}\sigma_{y,k}\kappa_o^2} \times \int_{a_x-\frac{a}{2}}^{a_x+\frac{a}{2}}\int_{a_y-\frac{a}{2}}^{a_y+\frac{a}{2}}\exp\left(-\frac{x^2}{2\sigma_{x,k}^2}-\frac{y^2}{2\sigma_{y,k}^2}\right)dydx, \tag{3.3}$$

where $A = 1/a^2$, a is the pixel length, κ_0 and κ are the magnification factor of the camera at a reference link span $L_{\mathrm{s},0}$ and at a distance of L_{s}, respectively, $\sigma_{x,k}^2 = \left(\frac{\kappa}{\kappa_0}\right)^2 \sigma_i'^2 + \sigma_{b,x}^2$, and $\sigma_{y,k}^2 = \left(\frac{\kappa}{\kappa_0}\right)^2 \sigma_i'^2 + \sigma_{b,y}^2$, with σ_i' denoting the parameter of the

model and $\sigma_{b,x}$ and $\sigma_{b,y}$ is the standard deviations in the x and y directions on the image plane, respectively. In (3.2), $a_x = (u - i)(a + g) - \xi_x$ and $a_y = (v - j)(a + g) - \xi_y$, where (ξ_x, ξ_y) and (i, j) are the coordinates of the centre of the image and the nearest pixel to this centre, respectively and g is the gap between two pixels.

Most OCC systems reported are based on the LOS configuration. However, in scenarios where the Txs are not within the LOS FoV, such as for two vehicles approaching a cross-road and vehicles travelling on a motorway, the communication channel will be via NLOS. In NLOS, reflected beams normally have large off-axis projected optical illumination footprints, which can increase the link tolerance to the camera movements. In [27], a RS camera and Manchester coding were employed to avoid flickering while capturing the reflected lights from the floor surface. Frequency shift keying was adopted in [140] for an RS-based OCC using reflected lights from surfaces. A data rate of 10 bps was achieved using a camera with frame rate of 30 fps for a MIMO system in an indoor environment. However, this approach is not efficient for OCC in terms of the bitrate. A long distance RS-based OCC approach was proposed in [55], which was based on the reflections from the floor surface at a distance of 1.5 m. Multi-level illumination [141] and Manchester coding with variable pulse widths [142] are other techniques used in NLOS RS-based OCC. A novel spatial multiplexing scheme for NLOS RS-based OCC with PSK was proposed in [143], where a data rate of 4.5 kbps was achieved at a distance of 1 m. However, RS-based OCC is not a suitable option for ITS, as its performance highly depends on the footprint of the light source. Since in ITS the link span is more than 5 m and the camera has a wide FoV located at ~1.3 m from the road surface, the footprints of the reflections are small especially at longer distances. Therefore, in the rest of the thesis, NRS-based OCC is considered. In Chapter 4, a comprehensive channel impulse response for NLOS OCC

is proposed.

3.2.3 *Receiver*

Figure 3.4 depicts a cut-through of a typical digital camera. The camera consists of a complex lens system, an adjustable aperture, optical low pass filters, an infrared cut filter, a micro lens array, a colour filter array and a sensor chip. Here, the structure and functionality of the main parts of a camera are briefly discussed.

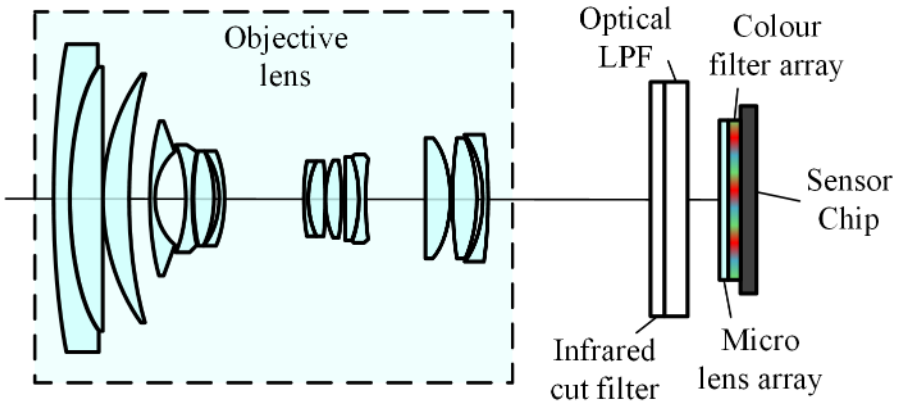

Figure 3.4: A simplified cut-through of a camera.

3.2.3.1 ***Lens System***

A lens is a device to converge or diverge light beams. In imaging, convex lenses are used to create a real image on the image plane of the camera, which is located at the image sensor plane. However, for the purpose of variable magnification and image correction, usually a complex set of convex and concave lenses are used in a lens system. Nevertheless, the overall complex lens system can be represented by a single lens with variable focal length, aperture size, and position (see Fig. 3.5). Therefore, in Chapter 4, the lens system is replaced by a single lens for simplicity, and the equations for the proposed system are derived. The magnification factor of the lens can be expressed as:

$$\kappa = \frac{f}{f - L_s}, \tag{3.4}$$

where L_s is the distance of the object from the lens and f is the focal length of the lens.

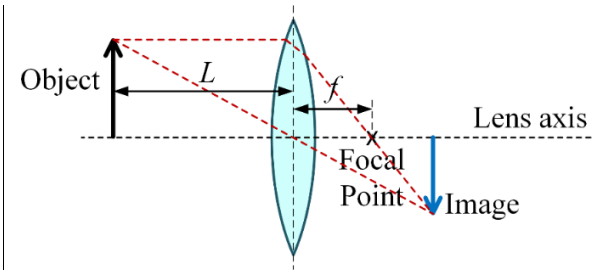

Figure 3.5: Ray tracing using a convex lens.

3.2.3.2 Image Sensor

A typical pixel structure of IS is illustrated in Fig. 3.6. A micro-lens array is used to increase the light collection efficiency of the IS since only a part of it is sensitive to the incoming photons. Following a colour filter array, which is used to recover the colours of the scene in the camera, part of the photons are absorbed by the PD to generate photoelectrons. To transfer charges from PDs to image processing circuits two techniques are used as outlined in the following.

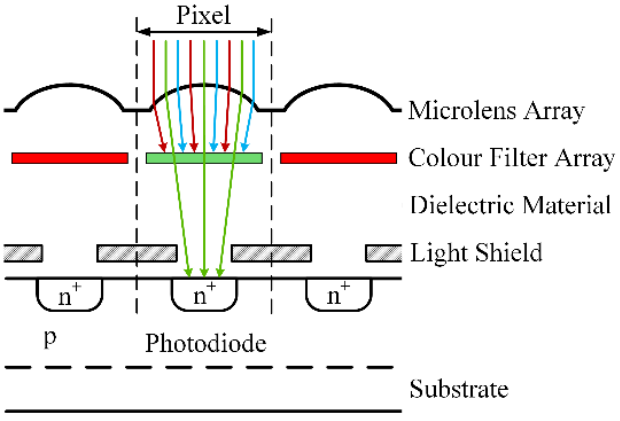

Figure 3.6: The structure of a pixel.

3.2.3.2.1 CCD Image Sensor

CCDs refer to devices where charges are transferred by moving them between capacitive bins within the device one at a time. In CCD cameras, the photosensitive region absorbs the light photons and a shift register region acts as the transmission part. In the CCD's structure, a large number of metal-oxide semiconductor (MOS) capacitors are placed within a close space to each other. The charge packet in the *i*-th potential well, see Fig. 3.7(a), can be transferred to the next well if a high voltage is applied to the electrode on both wells, thus forming a coupled potential well. In this case, the electrons from the *i*-th well can spread over the coupled well, see Fig. 3.7(b). Reducing the applied voltage on the electrode of the *i*-th well, the electron packet is completely transferred to the (*i*+1)-th well, see Fig. 3.7(c). In CCD cameras, the electron packets of each pixel are read through a vertical CCD (VCCD) and a horizontal CCD (HCCD) process, see Fig. 3.8. A single trans-impedance amplifier at the end of the horizontal CCD process then amplifies the electron packets. One of the artefacts of this architecture is the blooming effect, where the electrons from oversaturated pixels flow to the vertical neighbour pixels.

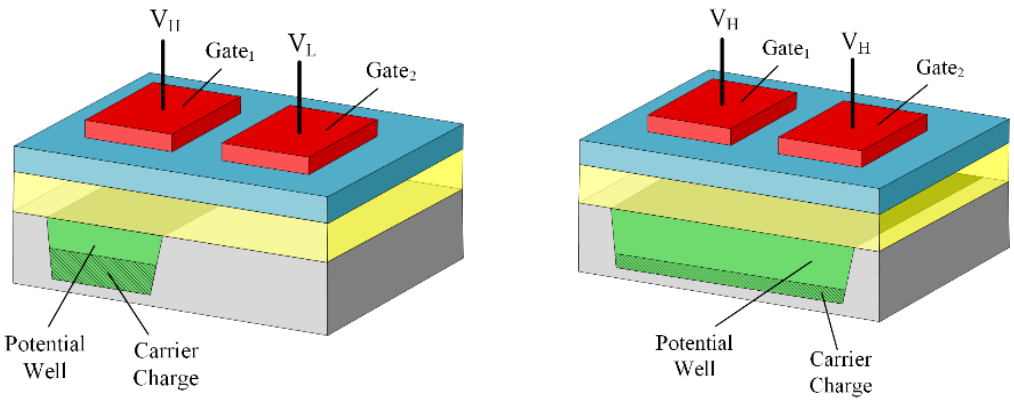

(a) (b)

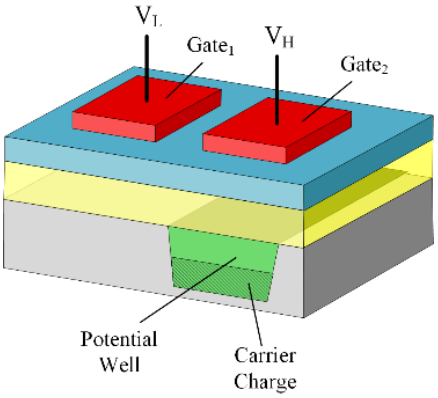

(c)

Figure 3.7: The concept of CCD charge transfer: (a) Gate$_1$ is activated by high voltage and Gate$_2$ is deactivated, (b) both gates are activated, and (c) Gate$_1$ is deactivated and Gate$_2$ is activated.

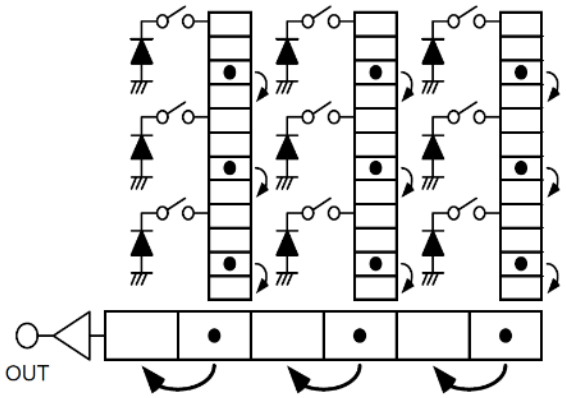

Figure 3.8: Charge transfer in a CCD camera employing a vertical CCD followed by a horizontal CCD [144].

3.2.3.2.2 CMOS IS

Complimentary metal-oxide semiconductor (CMOS) technology is a mature technology used in a wide range of devices such as solid-state memories, CPUs, and ISs. In the CMOS technology, metal-oxide semiconductor field effect transistors (MOSFET) are used for switching. The applications of CMOS cameras range from professional photographing cameras, low-cost cameras, and surveillance to industrial high-speed machine vision. The advantages of using CMOS over CCD cameras

include low power consumption, faster readout, more programmability, and low cost. Accordingly, CMOS is preferred for communication applications in the literature [6, 9, 27]. In a CMOS active pixel sensor (APS), each pixel is equipped with an amplifier (see Fig. 3.9), providing suppressed noise generated in the signal readout path (e.g., smear artefact, which occurs in the form of vertical streaks as a result of photodetectors being exposed to the light during readout process [145]). Pixel scanning in CMOS cameras is based on the X-Y address scheme, providing flexibility to activate the desired pixels. This helps to increase the readout speed (i.e., achieves a higher frame rate and a low power consumption). In C2C communications, this feature can be beneficial because when the link span increases, the camera can limit its active area to increase the frame rate. Moreover, CMOS cameras are cheaper, which has motivated car manufacturers to adopt them for the dash and rear cameras. Therefore, in this thesis, a CMOS-based image sensor is employed. The drawback associated with CMOS cameras compared to CCD is that they have smaller optical sensitive active area, which results in a low SNR. Moreover, having an individual amplifier on each pixel yields more circuit noise and fixed pattern noise.

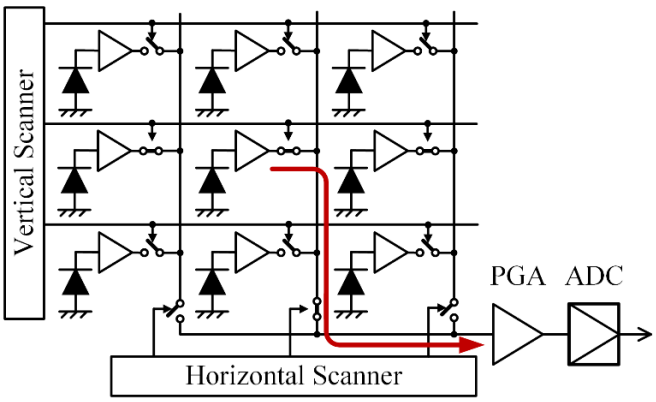

Figure 3.9: CMOS architecture with the X-Y addressing readout method (recreated from [144]).

3.2.3.2.3 Rolling Shutter and Global Shutter

In global shutter cameras, all pixels are exposed to the light at the same time, while in a RS camera, the reset and readout pulses are sent to each row sequentially (see Fig. 3.10(a)). In very fast movements, RS cameras present a distorted shape of the object in the image, which is unpleasant for photography purposes. However, RS cameras can be utilized to increase the data reception rate. By employing a high frequency transmitted signal, each row of the image is exposed with a different level of light throughout the shape of the object if the exposure time is set to a very low value (see Fig. 3.10(b)). As explained earlier, RS-based OCC is not compatible with ITS. Therefore, in this thesis, a NRS-based approach is employed.

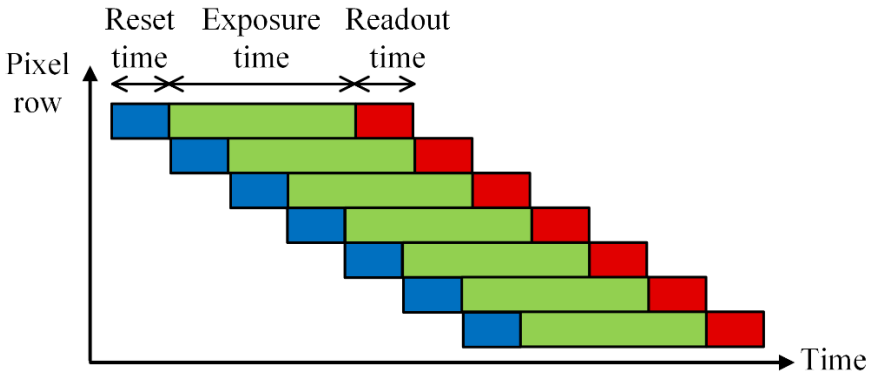

(a)

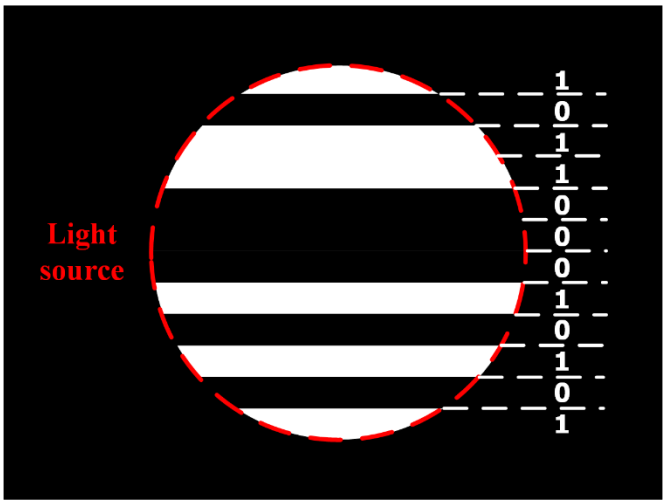

(b)

Figure 3.10: (a) RS timing, and (b) RS-based data reception

3.2.3.2.4 Bayer Pattern

In digital cameras, a very popular approach to record the colour information of objects is to use a colour filter array (CFA). CFAs consist of an array of alternating colour filters, each located in front of a PD. Thus, a different colour band, usually red, green, and blue, illuminates each PD. The most popular CFA pattern is the Bayer pattern, where the number of green filters is double the number of red and blue filters. The reason behind this arrangement is that the human eye is more sensitive to the green colour, hence the need to have precise green information (see Fig. 3.11(a)) [146]. Figure 3.11(b) illustrates a RGBG Bayer pattern. In order to retrieve the information of other colours at each pixel, a demosaicing algorithm is required. This algorithm can be as simple as a linear interpolation, or can involve complex non-linear interpolators [147].

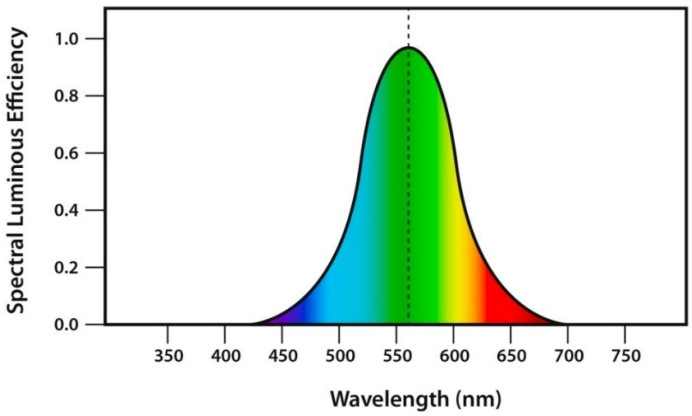

(a)

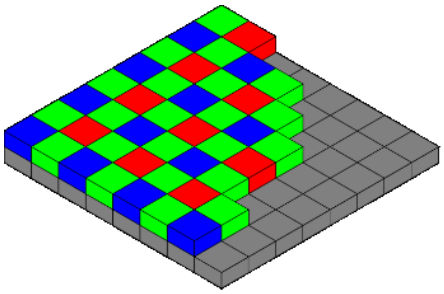

(b)

Figure 3.11: (a) Spectral efficiency of the human eye as a function of wavelength [148], and (b) Bayer pattern colour filter array [149].

The available LED-based streetlights and head and taillights are single tone (i.e., either white LEDs made from a blue LED coated by a yellow phosphorescence or red LEDs). Accordingly, in this thesis, colour division multiplexing and CSK are not considered. Therefore, before processing the frames of the video stream, it is converted to grayscale as advised in the BT.601-7 recommendation [150]:

$$\widetilde{\mathbf{Y}} = 0.2989 \times \widetilde{\mathbf{Y}}^{\mathrm{R}} + 0.5870 \times \widetilde{\mathbf{Y}}^{\mathrm{G}} + 0.1140 \times \widetilde{\mathbf{Y}}^{\mathrm{B}}, \tag{3.5}$$

where $\widetilde{\mathbf{Y}}^{\mathrm{R}}$, $\widetilde{\mathbf{Y}}^{\mathrm{G}}$, and $\widetilde{\mathbf{Y}}^{\mathrm{B}}$ are the red, green and blue components of the image, respectively.

3.2.3.3 Noise in Image Sensors

The noise in ISs can be categorised as either temporal or spatial noise.

3.2.3.3.1 Spatial Noise

The spatial noise is known as the fixed pattern noise (FPN). In a CMOS image sensor, FPN in dark conditions is mainly due to the dark current non-uniformity, whereas under illumination, it is a result of the gain variation of the active transistors inside each pixel. The number of dark current charges can be calculated via [144]:

$$\sigma_{\mathrm{dark}}^2 = N_{\mathrm{dark}} = \frac{I_{\mathrm{dark}} T_{\mathrm{exp}}}{q}, \tag{3.6}$$

where I_{dark} is the dark current produced in the PD, T_{exp} is the exposure time, and q is the electron charge.

3.2.3.3.2 Temporal Noise

The main temporal noise sources in an image sensor are thermal noise, photocurrent shot noise, and flicker noise.

- Thermal noise in a camera mostly occurs in the form of readout and reset noise and is a result of thermal agitation of electrons in the resistance of the circuits in a Bandwidth of B. The variance of the thermal noise can be calculated as follows [144]:

$$\sigma^2_{\text{thermal}} = 4KTB\left(R + \frac{1}{4C} + \frac{\varpi}{g_{\text{m}}}\right), \tag{3.7}$$

where K is Boltzmann's constant, T is the temperature in kelvin, R is the resistance, C is the capacitance at the reset gate, g_{m} is the transconductance of the MOS transistor and ϖ is a coefficient, which depends on the modes of the MOS transistor operation.

- Photocurrent shot noise occurs mainly due to the stochastic nature of the photo conversion process in the PD. The probability that N_e number of photoelectrons released in a T_{exp} time interval has a Poisson distribution with a mean of $\overline{N_e}$ is [144]:

$$P_{N_e} = \frac{\overline{N_e}^{N_e} \exp(-\overline{N_e})}{N_e!}. \tag{3.8}$$

Hence, the variance of the photocurrent shot noise $\sigma^2_{\text{shot}} = \overline{N_e}$.

- In MOS transistors, there is another source of noise called flicker noise (also referred to as $1/F$ noise) and is calculated via [144]:

$$v^2_{1/F} = \frac{K_F}{C_{ox} W_{\text{mos}} L_{\text{mos}}} . \frac{\Delta F}{F}, \tag{3.9}$$

where K_F is a constant which depends on the device parameters such as transistor size, F is the frequency, ΔF is the bandwidth, and C_{ox}, W_{mos}, and L_{mos} denote the gate capacitance, width and length of the MOS gate,

respectively.

3.2.3.4 ***Exposure***

In a camera, three main parameters control the brightness level in the picture: exposure time, ISO, and the aperture. Here, each parameter is discussed in terms of the role it plays in the quality of the picture.

3.2.3.4.1 ISO

In ISs, sensitivity is defined as the ratio of the output signal of the image sensor to the exposure level, which is the product of illuminance and T_{exp} [144]. In a photographic system, the ISO indicator shows the adequate exposure and can be obtained via:

$$S_{\text{ISO}} = \frac{K_{\text{ISO}}}{E}, \tag{3.10}$$

where K_{ISO} is a constant, which according to the standard ISO 2240 and ISO 2721 can be set to 10, and E is the exposure measured in lux-seconds (i.e., ISO 100 is equivalent to $E = 0.1$ (lux-s)). After sampling, a programmable gain amplifier (PGA) is used to effectively utilize the input range of the analogue to digital converter (ADC) (see Fig. 3.8). The PGA controls the ISO speed, where with every doubling in ISO speed, the brightness of the image is doubled [144].

3.2.3.4.2 Aperture

The aperture is a device, similar to a pupil, installed in the lens system of the camera to control the amount of light coming through the lens system. It usually consists of a number of blades that form a circular shape (see Fig. 3.12(a)). A parameter called the

f-number usually represents the diameter of the aperture:

$$f_{\#} = \frac{f}{D_{\text{lens}}} \tag{3.11}$$

where D_{lens} is the diameter of the aperture. For example, for a given f the area of an aperture with an f-number of $f/5.6$ is double the area of an aperture with an f-number of $f/4$. Although, larger apertures yield higher SNRs, they decrease the depth of field, which is defined as the range of distance from the plane of focus, where objects look reasonably sharp in the image. The out-of-focus objects look unclear, which is due to the image of the object being created in another plane other than the image sensor plane. In this situation, every point on the clear image of the object is convoluted by a circle of confusion (CoC), which has the same shape as that of the aperture surface. The concept of the circle of confusion is illustrated in Fig. 3.12(b).

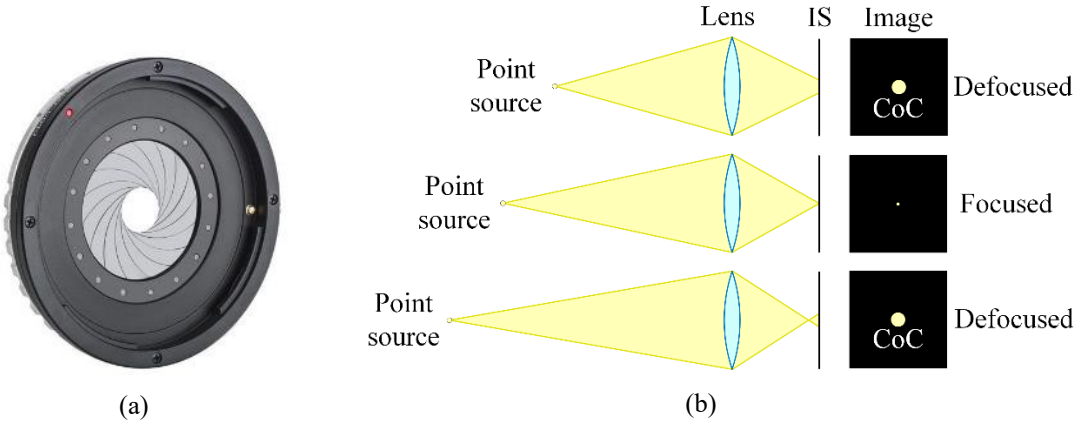

Figure 3.12: (a) An aperture, and (b) circle of confusion: when the point source is too close or too far to the camera.

3.2.3.4.3 Exposure time

As explained earlier, before exposing the PDs to the light, each pixel needs to be reset. Due to the parasitic capacitance C of the PD, the resetting duration is T_{res}. In the time interval between when the pixel is reset and when it is ready to be read-out (also known as the exposure time T_{exp}), the PD is exposed to the light and accumulates

the photoelectrons. Accordingly, the read-out circuit at time $t = kT_{\mathrm{fr}} + T_{\mathrm{res}} + T_{\mathrm{exp}}$ reads and samples the signal, where T_{fr} is the frame duration. The CMOS APS pixel can be modelled as a linear shift-invariant (LSI) system [151]. Thus, the output signal of pixels can be calculated as:

$$\begin{aligned}\mathbf{Y}(t) &= \left(x_{\mathrm{op}}(t) \times \mathbf{H}_{\mathrm{ch}}(t) + \mathbf{N}(t)\right) \otimes \mathbf{H}_{\mathrm{cam}}(t) \\ &= \mathbf{A}\int_{t-T_{\mathrm{exp}}}^{t} \left(x_{\mathrm{op}}(\tau) \otimes \mathbf{H}_{\mathrm{ch}}(\tau) + \mathbf{N}(\tau)\right) d\tau\end{aligned} \tag{3.12}$$

where $\mathbf{H}_{\mathrm{cam}}(t)$ and $\mathbf{N}(t)$ denote the integrator impulse response and the noise of the image sensor, respectively. $\otimes$ denotes the convolution operator. $\mathbf{A} = -\left[\frac{g_{\mathrm{PIX}}(u,v) g_{\mathrm{b}} \mathcal{R}(u,v)}{C}\right]_{U\times V}$, where g_{PIX} and g_b are the gain of the (u, v)-th pixel amplifier and PGA, respectively, $\mathcal{R}(u, v)$ is the quantum efficiency of the PD, and C is the capacitance at the (u, v)-th pixel's PD. If the integrator starts sampling at $t = kT_{\mathrm{fr}} + T_{\mathrm{res}}$, then we have:

$$\mathbf{Y}[kT_{\mathrm{fr}}] = \mathbf{A}\int_{kT_{\mathrm{fr}}+T_{\mathrm{res}}}^{kT_{\mathrm{fr}}+T_{\mathrm{res}}+T_{\mathrm{exp}}} x(\tau) d\tau, \tag{3.13}$$

where $T_{\mathrm{fr}} = 1/R_f$ is the time interval between two frames. If the received signal remains unchanged during the exposure time, then we have [151]:

$$\mathbf{H}_{\mathrm{cam}}(t) = \mathbf{A}\left(\Gamma(t) - \Gamma\left(t - T_{\mathrm{exp}}\right)\right), \tag{3.14}$$

where $\Gamma(t)$ is Heaviside step function. The frequency response of $\mathbf{H}_{\mathrm{cam}}(t)$ can be expressed by applying a Fourier transform [151]:

$$\mathbf{H}_{\mathrm{cam}}(\omega) = \mathbf{A}\exp\left(-\frac{j\omega T_{\mathrm{exp}}}{2}\right)\frac{2\sin\left(\omega T_{\mathrm{exp}}/2\right)}{\omega}, \tag{3.15}$$

where $j = \sqrt{-1}$ and ω is the angular frequency. Accordingly, the -3 dB bandwidth of

the integrator is $B \approx \frac{3.791}{T_{\text{exp}}}$. This means that, if the bandwidth of the RS signal is more than B, the output signal will be distorted. In addition, it can be concluded that under long exposures times, it is more likely that motion blur may occurs due to movement of the camera or objects within its FoV.

3.2.3.5 ***Gamma Correction***

The human eye's response to brightness follows a logarithmic law, known as the Weber-Fechner law, which is given by [152]:

$$I_{\text{ab}} = \chi \log\left(\frac{I_{\text{b}}}{I_{\text{b,th}}}\right), \qquad I_{\text{b}} > I_{\text{b,th}}, \tag{3.16}$$

where I_{b}, $I_{\text{b,th}}$, and I_{ab} denote the magnitude of the brightness, the threshold brightness, and the apparent brightness, respectively and χ is a constant. Ideally, the brightness of a picture taken with a camera should follow the logarithmic curve of the human eye. As such, cameras change the brightness of the pictures in the JPEG format on a logarithmic scale as follows:

$$\mathbf{Y}_G(kT_{\text{fr}}) = [y_G(kT_{\text{fr}})]_{M\times N} = G(\mathbf{Y}(kT_{\text{fr}})) = \mathbf{Y}(kT_{\text{fr}})^{\gamma}, \tag{3.17}$$

where $G(.)$ is a logarithmic function intensity and γ is the gamma factor. This process is known as the gamma correction or the tone curve correction. However, different cameras may have slightly different curves. For instance, Canon cameras apply an S-shape gamma curve shown in Fig. 3.13. This means that in the logarithmic scale, the slope of the curve might change with the input intensity.

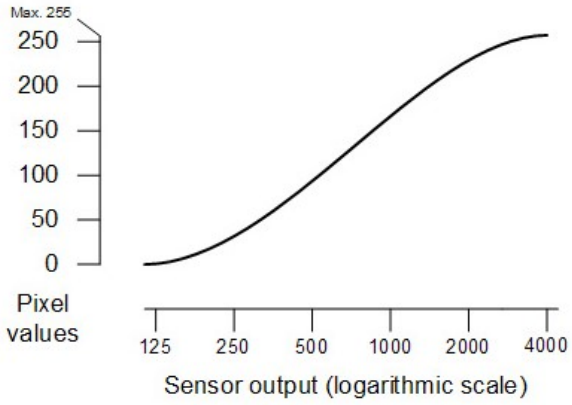

Figure 3.13: The gamma correction curve for Canon cameras [153].

3.2.3.6 ***Combining Techniques in OCC***

In a camera, each pixel can be employed as an independent Rx to record independent information (i.e., a few million independent Rxs). Accordingly, the camera can be employed as a diversity Rx. In order to exploit the information at the diversity Rxs in a SIMO systems, there are a number of combining techniques available, including selection combining (SC) and gain combining [154]. The output signal y in the gain combining technique is simply a linear combination of the received signals as given by [154]:

$$Z(kT_{\mathrm{fr}}) = [\mathbf{Y}_G(kT_{\mathrm{fr}})]^{\mathrm{T}}_{N_r\times 1}\mathbf{w}_{N_r\times 1} = \sum_{n=1}^{N_r} w_n y_{G,n}(kT_{\mathrm{fr}}), \tag{3.18}$$

where $\mathbf{w}_{N_r\times 1} = [w_n]_{N_r\times 1}$ is the matrix of combining weights (see Fig. 3.14). Depending on these weights, different combining techniques can be defined. In SC, the Rx compares the SNR, absolute power, or error rate of different branches and chooses the branch with the highest quality. In the case of equal noise levels on all branches, the SC detector selects the branch with the largest received amplitude. Therefore in $\mathbf{w}_{N_r\times 1}$, only one of the elements is 1 and the rest are zero.

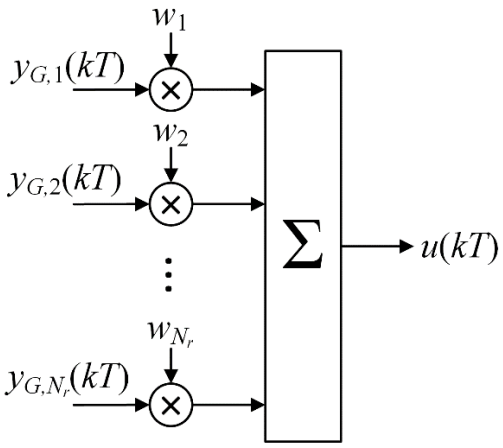

Figure 3.14: The general diagram of combining methods.

The simplest gain combining method is the equal gain combining (EGC), where all the weights are unity. In this case, the received signal can be expressed as:

$$Z(kT_{\mathrm{fr}}) = [\mathbf{Y_G}]^{\mathrm{T}}_{N_{\mathrm{r}}\times 1} \times \mathbf{1}_{N_{\mathrm{r}}\times 1} = \sum_{n=1}^{N_r} y_{G,n}\,(kT_{\mathrm{fr}}). \tag{3.19}$$

where $\mathbf{1}_{N_{\mathrm{r}}\times 1}$ is the matrix of unity. Another combining method is the maximal ratio combining (MRC) method, where $\mathbf{w}_{N_{\mathrm{r}}\times 1} = \mathbf{H}^{\mathrm{H}}_{N_{\mathrm{r}}\times 1}$ and $\mathbf{H}^{\mathrm{H}}_{N_{\mathrm{r}}\times 1} = \left[H^{\mathrm{H}}_{k}\right]_{N_{\mathrm{r}}\times 1}$ is the Hermitian transform of $\mathbf{H}_{N_{\mathrm{r}}\times 1} = [\mathbf{H}_{\mathrm{cam}}]_{N_{\mathrm{r}}\times 1} \otimes [\mathbf{H}_{\mathrm{ch}}]_{N_{\mathrm{r}}\times 1}$, hence [154]:

$$Z(kT_{\mathrm{fr}}) = [\mathbf{Y_G}]^{\mathrm{T}}_{N_{\mathrm{r}}\times 1} \times \mathbf{H}^{\mathrm{H}}_{N_{\mathrm{r}}\times 1}, \tag{3.20}$$

This scheme maximizes the average output SNR [155]. It is also possible to use a hybrid selection/MRC (HS/MRC) or a hybrid selection/EGC (HS/EGC) method. In these methods, at each time instant, $N'_{\mathrm{r}} < N_{\mathrm{r}}$ Rxs with the largest SNRs are chosen among N_{r} Rxs, and then the EGC or MRC techniques are applied to the selected Rxs. The advantage of using HS/MRC and HS/EGC is enabling the use of only $N_{\mathrm{r}}{}'$ Rxs to extract the full diversity and a large array gain. In this thesis, HS/EGC and HS/MRC are adopted to extract information from a video stream in the presence of interference sources.

While SC is the most popular method in the OCC literature, EGC and MRC help to further improve the SNR of the received signal. In [32], MRC, EGC, and SC schemes were demonstrated for the proposed model of a single LED to camera communications. In [6] and [9], a customized IS was used, where each pixel was equipped by a low-frame-rate camera pixel and a high speed μ-scale PD to receive high frequency information. A special SC method was developed to use the camera pixel to find the location of the Tx and activate the neighbour PDs. In [156] and [157], a SC scheme was used to recover the intensity of the Tx in a SIMO RS-based OCC, where the best column of the picture (i.e., the column with the most number of ribbons) was selected. In [27] and [158], a HS/EGC method was employed for a RS-based OCC to increase the SNR, and a correction method was proposed to correct the shape distortion. In Chapters 4 and 5, HS/EGC is adopted to extract the information from video frames under low to medium levels of interference. However, in Chapter 6, the performance of HS/EGC, HS/MRC and ZFE are compared under high levels of interference.

In the demodulator, the combined signal is demodulated in order to recover the estimated data $\hat{d}$.

3.3 Summary

In this chapter, a typical OCC system block diagram was presented. Furthermore, different modulation formats proposed in the literature for OCC in order to avoid flickering were reviewed. A channel model for LOS OCC was also introduced, and the research conducted in the literature on NLOS OCC was highlighted. A typical camera structure was subsequently illustrated, and the roles of the main part of the

camera (i.e., lens system, aperture, and image sensor) were discussed. In addition, different parameters that affects the exposure in a camera were explained in detail. A correction factor in the camera, namely the gamma curve, was also introduced. Moreover, noise sources in image sensors were discussed, and finally, combining techniques adopted in the literature were reviewed.

Chapter 4 SPACE DIVISION MULTIPLEXING HYBRID SELECTION/EQUAL GAIN COMBINING

4.1 Introduction

As discussed earlier, the OCC offer new possibilities for the use of VLC systems in a number of applications including display based transmission, D2DC - as part of the internet of things, and vehicular communications where the camera based Rx will offer multiple functionalities including vision, data transmission, localization and range measurement. A camera-based Rx in OCC, which is composed of an imaging lens and IS has many unique features including a wide FoV due to the PD array, as well as spatial and wavelength separation of light beams.

Most OCC systems reported are based on the LOS transmission mode. However, in some scenarios the Txs are not within the LOS's FoV. Figure 4.1(a) illustrates two vehicles approaching a crossroad, where the vehicle B is not in the FoV of the vehicle

A but the light beams and its reflections from the road surface are. Note, the blue area within the dashed lines is where the camera can see. Another example is when two vehicles travel on a motorway side-by-side where the camera can only pick the reflections of the headlight of the other car from the road surface (see Fig. 4.1(b)). In addition to car-to-car scenarios, the LOS link may not be available for car to infrastructure communications. For example, (*i*) lampposts in highways, which can be outside the camera's FoV, where light reflections from the road surface can be picked up by the camera (see Fig. 4.1(c));(*ii*) a heavy goods vehicle blocking the LOS of the vehicle behind, see Fig. 4.1(d), where the camera can pick up off-axis projected optical illuminations induced reflections; (*iii*) in urban areas tall trees might block the streetlights as depicted in Fig. 4.1(e), where camera can only capture the reflected lights.

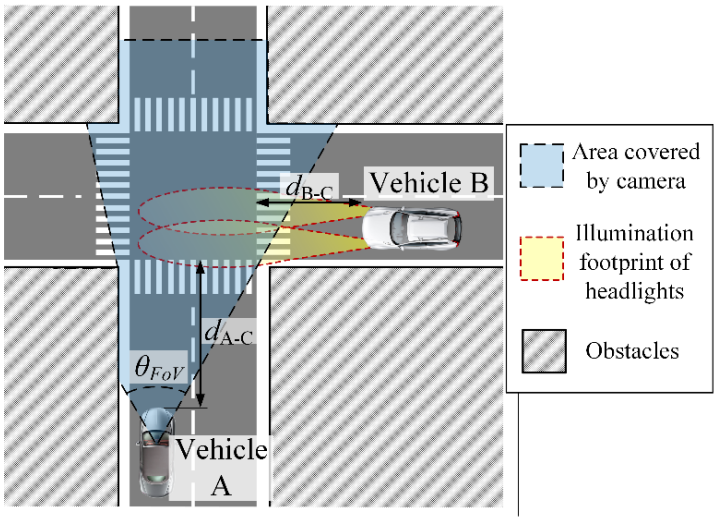

(a)

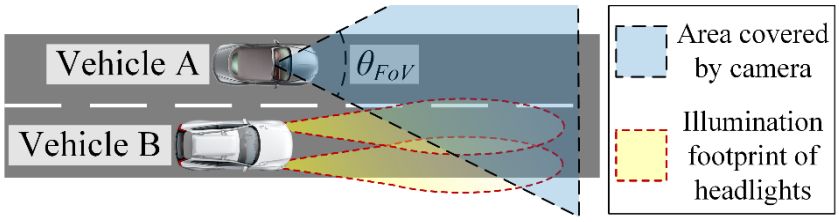

(b)

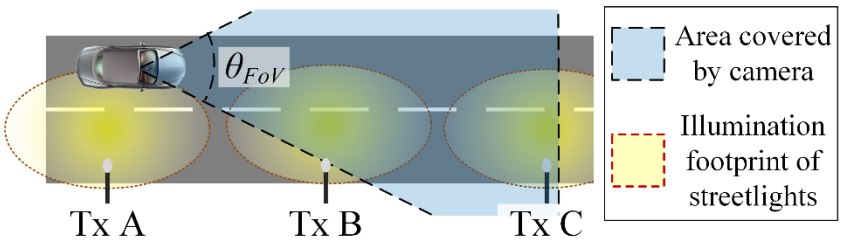

(c)

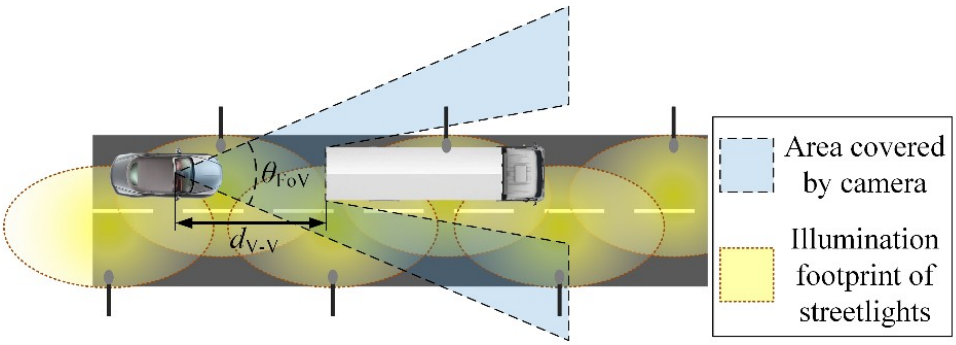

(d)

(e)

Figure 4.1: Different scenarios where there is no LOS between the transmitter and Rx in C2C OCC: (a) two vehicles approaching a cross road, (b) two vehicles driving side-by-side in a highway, (c) Streetlight being out of FoV of the camera, (d) a truck blocking the LOS link, and (e) tall trees blocking the LOS link in urban areas [159].

In order to reduce the impact of channel crosstalk, different multiple access/multiplexing techniques based on time, frequency, space, wavelength and code have been proposed in VLC. These techniques include frequency division multiple access (FDMA)/multiplexing (FDM) [160], time division multiple access (TDMA)/multiplexing (TDM) [161], code division multiple access (CDMA) [162],

space division multiple access (SDMA)/multiplexing (SDM) [163], wavelength division multiplexing (WDM) [164], orthogonal frequency division multiple access (OFDMA)/multiplexing (OFDM) [165], non-orthogonal multiple access (NOMA) [166], etc. In RS-based OCC, FDMA/TDMA was adopted in [47] as multiple access techniques in a hybrid VLC system for camera and low-power embedded devices using high spatial frequency components of the RS signal and achieved a data rate of >10 bps with a 30-fps camera. In [58], CDMA together with CSK were used to achieve a data rate of 15 bps for a spreading factor of 4, with a frame rate of 30 fps and a bit per symbol of 2. An OFDM-like transmission scheme was proposed in [167], which encodes the data in spatial frequencies in a liquid crystal display (LCD)-based camera communications, with a data rate of ~15 Mbps over a distance of 5 m, i.e., >13 Mbps more data rate compared to quick response (QR) codes. WDM for OCC was presented in [168], which used an RGB LED and RS effect to achieve a data rate of 2.88 kbit/s.

The most popular multiplexing/multiple access technique is SDM/SDMA due to a massive built-in matrix of Rxs in the camera, thus effecting MIMO or MU-MIMO Rx camera abilities. In [169], SDMA was adopted to provide multiple access for a two-way OCC for mobile objects and using a synchronisation algorithm demonstrated a measured data rate of 25 fps with a 30-fps camera. SDM was adopted in [170], to spatially separate the link between an 8×8 array of LEDs and a camera with a frame rate of 30 fps, which could achieve a data rate of 1280 bps and support camera rotation compensation.

Among these multiple access/multiplexing techniques, FDMA and OFDMA require either RS-based OCC or LCD as the Tx. Therefore, due to the low frame rate of the camera, in NRS-based LED to camera OCC only WDMA, TDMA, SDMA and NOMA can be adopted. Since the available LED-based street lights are single colour,

we do not consider WDMA in this work. Moreover, since the streetlights are positioned at a distance of >20 m from each other and in a mobile system the view of the camera is changing constantly, applying NOMA is very complex. Accordingly, in this Chapter we employ SDM and in Chapter 5 we investigate the SDM-TDM technique.

In this chapter, we considered the scenario where there is no LOS from streetlight to the vehicle. An end-to-end NLOS $2 \times N_{\mathrm{r}}$ OCC system is proposed, which is based on a combination of successive frame subtraction and differential signalling schemes for detection and transmission, respectively. Moreover, two combining techniques of HS/EGC and HS/MRC are adopted and their results are compared. Note, in the literature SC is also known as block matching [50]. A unique non-standard packet structure is suggested for the proposed system and a new detection algorithm is also given. We experimentally investigate the system BER performance and show that it can be improved by increasing both the ISO and the exposure time T_{exp} of the camera. We show that, the BER performance of HS/MRC is very similar to HS/EGC, which we attribute this to the fact that in the region of interest the intensity of the pixels does not vary significantly. We also show that, a very low transmit power of 16 mW per Tx is needed to achieve a BER of 10^{-3}, which is below the 7% forward error correction (FEC) limit of 3.8×10^{-3}, over a link span of 5 m. Moreover, we investigate the impact of interference from other nearby Txs on the link performance and we show that, with two Txs if the overlapping area of optical footprints is more than 50% of the total footprint of a single Tx then the signal cannot be fully recovered.

4.2 Theory

Assuming a linear shift-invariant channel and considering a single light reflection, the received optical signal is given by:

$$\mathbf{Y}_l(t) = P_{\mathrm{t},l}\Re g_{\mathrm{lens}} x_{\mathrm{op},l}(t) \otimes \mathbf{H}_l(t) + \mathbf{N}(t) + \mathbf{I}(t), \tag{4.1}$$

where $P_{\mathrm{t},l}$ is the transmit power of the l-th Tx located at $(x_{\mathrm{t},l}, y_{\mathrm{t},l}, H_{\mathrm{t},l})$, $\Re$ is the responsivity of the IS array with a size of $U \times V$, where U and V are the number of rows and columns in the image, respectively and g_{lens} presents the gain of the camera lenses. $x_{\mathrm{op},l}(t)$ is the transmitted optical signal of the l-th Tx, which is a scalar number, and $\mathbf{N}(t)$ is the noise, which is modeled as a Gaussian distributed random variable (GDRV) with the mean of μ_{N} and variance of σ_{N}^2 [171]. $\mathbf{I}(t)$ is the interference from other Txs. Note, $\mathbf{H}_l(t) = \mathbf{H}_{\mathrm{ch},l}(t) \otimes \mathbf{H}_{\mathrm{cam}}(t)$, which is a matrix of size $U \times V$, where $\mathbf{H}_{\mathrm{ch},l}(t)$ is the impulse response of the channel, and $\mathbf{H}_{\mathrm{cam}}(t)$ is the impulse response of the CMOS with an active pixel matrix given by [151]:

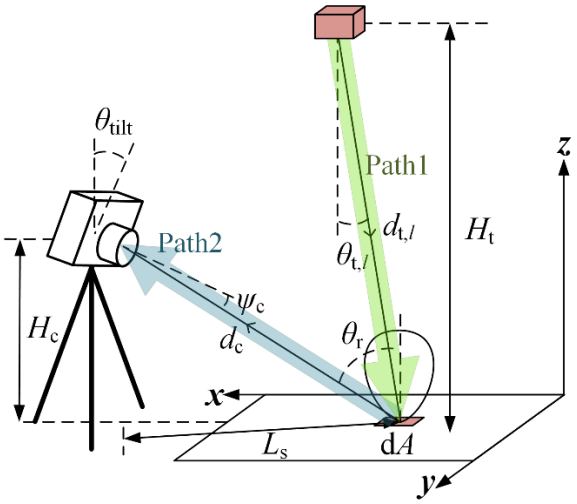

Figure 4.2: Configuration of the proposed system.

$$\mathbf{H}_{\mathrm{cam}}(\omega) = \mathbf{G}e^{-\frac{j\omega T_{\mathrm{exp}}}{2}}\left(\frac{2\sin\left(0.5\omega T_{\mathrm{exp}}\right)}{\omega}\right), \tag{4.2}$$

where $\mathbf{G}$ is the gain matrix of the preamplifiers and ω is the angular frequency. Here, $\otimes$ denotes the convolution operation, which acts element-wise on the matrix.

In the proposed NLOS model, see Fig. 4.2, the trajectory of light beams to the camera located at $(x_{\mathrm{c}}, y_{\mathrm{c}}, H_{\mathrm{c}})$ can be divided into two LOS paths i.e., Path1 and Path2, which exist between the Tx and the floor, and between the element of area $\mathrm{d}A = \mathrm{d}x\mathrm{d}y$ on the floor and the camera, respectively. Note, the light intensity in $\mathrm{d}A$ is assumed to be constant. The overall received power from the l-th Tx at the pixel (i, j) of the camera is given by [139]:

$$h_{\mathrm{ch},l}(u,v) = \int_{x_{u-1}}^{x_u} \int_{y_{v-1}(x)}^{y_v(x)} R_{\mathrm{t},l}(x,y) \frac{\mathrm{d}A}{d_{\mathrm{t},l}^2(x,y)} \times R_{\mathrm{r}}(x,y) \frac{A_{\mathrm{lens}}}{d_{\mathrm{c}}^2(x,y)} \rho \times \cos\big(\psi_{\mathrm{c}}(x,y)\big), \quad u = 1, \dots, U, \quad v = 1, \dots, V. \tag{4.3}$$

where $A_{\mathrm{lens}} \approx \frac{\pi}{4}\left(\frac{f}{f_{\mathrm{stop}}}\right)^2$ and f are aperture area and the focal length of the lens, respectively, f_{stop} is the f-stop number for the aperture and ρ is the reflection coefficient of the surface. $d_{\mathrm{t},l}(x,y)$ and $d_{\mathrm{c}}(x,y)$ are the distances between the l-th Tx and the $dA(x,y,0)$, and between the camera and dA, respectively defined as [139, 172]:

$$d_{\mathrm{t},l}(x,y) = \sqrt{\big(x - x_{\mathrm{t},l}\big)^2 + \big(y - y_{\mathrm{t},l}\big)^2 + H_{\mathrm{t},l}^2}, \tag{4.4}$$

$$d_{\mathrm{c}}(x,y) = \sqrt{(x - x_{\mathrm{c}})^2 + (y - y_{\mathrm{c}})^2 + H_{\mathrm{c}}^2}. \tag{4.5}$$

$R_{\mathrm{t},l}(x,y)$ and $R_{\mathrm{r}}(x,y)$ are LED beam profile and Lambertian radiation pattern of $\mathrm{d}A$, respectively, which is given by [139]:

$$R_{\mathrm{t},l}(x,y) = \frac{m_{\mathrm{t},l} + 1}{2\pi} \cos^{m_{\mathrm{t},l}}\Big(\theta_{\mathrm{t},l}(x,y)\Big), \tag{4.6}$$

$$R_{\mathrm{r}}(x,y) = \frac{m_{\mathrm{r}} + 1}{2\pi} \cos^{m_{\mathrm{r}}}\big(\theta_{\mathrm{r}}(x,y)\big). \tag{4.7}$$

where $m_{\mathrm{t},l}$ and m_{r} are Lambertian order for the l-th LED and the reflected beam

profile, respectively. $\theta_{\mathrm{t},l}(x,y)$ and $\theta_{\mathrm{r}}(x,y)$ are emission angles of the Tx and the reflection to the Rx, respectively given as:

$$\theta_{\mathrm{t},l}(x,y) = \tan^{-1}\left(\frac{\sqrt{\left(x-x_{\mathrm{t},l}\right)^2+\left(y-y_{\mathrm{t},l}\right)^2}}{H_{\mathrm{t},l}}\right), \tag{4.8}$$

$$\theta_{\mathrm{r}}(x,y) = \tan^{-1}\left(\frac{\sqrt{(x-x_{\mathrm{c}})^2+(y-y_{\mathrm{c}})^2}}{H_{\mathrm{c}}}\right). \tag{4.9}$$

In (4.7), the incident angle of the camera $\psi_c(x,y) = \cos^{-1}(\overrightarrow{n_l}.\overrightarrow{n_c})$ where $\overrightarrow{n_l} = (x-x_c, y-y_c, -H_c)$ and $\overrightarrow{n_c} = (-\cos(\phi_{\mathrm{tilt}})\cos(\theta_{\mathrm{tilt}}),\ \sin(\phi_{\mathrm{tilt}})\cos(\theta_{\mathrm{tilt}}),\ -\sin(\theta_{\mathrm{tilt}}))$ denote the unitized incident beam and the camera plain normal vector, respectively and the dot denotes the inner product. Here, ϕ_{tilt} and θ_{tilt} are azimuth and elevation tilting angles of the camera, respectively, see Fig. 4.2.

In (4.7), the integral limits of x_u and $y_v(x)$ are the boundaries of the area, which the pixel (u,v) cover in the x and y dimensions on the floor surface. Fig. 4.3(a) illustrated the boundaries that each pixel covers on the floor plane in the $\vec{y}$ direction, which can be obtained as:

$$x_u = H_{\mathrm{c}} \times \tan\left(\sum_{i=0}^{u}\theta_i\right) + x_{\mathrm{c}}. \tag{4.10}$$

where x_{c} and H_{c} are the camera position in the y direction and its height from floor, respectively. Here, $\theta_0 = \theta_{\mathrm{T}} - \frac{\theta_{\mathrm{FoV}}}{2}$ is the angle between the normal line to the floor that passes the center of the lens and lower boundary of FoV.

$$\sum_{i=0}^{u}\theta_i = \theta_{\mathrm{T}} + \tan^{-1}\left(\frac{\left(u-\frac{U}{2}\right)a}{f}\right), \qquad 1 \le u \le U, \tag{4.11}$$

where $\theta_{\mathrm{T}} = \frac{\pi}{2} - \theta_{\mathrm{tilt}}$, a is the width of the pixel. Ultimately, the boundaries can be calculated as:

$$x_u = x_{\mathrm{c}} - H_{\mathrm{c}} \times \frac{\left(u - \frac{U}{2}\right) a \cos(\theta_{\mathrm{T}}) + f \sin(\theta_{\mathrm{T}})}{f \cos(\theta_{\mathrm{T}}) - \left(u - \frac{U}{2}\right) a \sin(\theta_{\mathrm{T}})}. \tag{4.12}$$

Fig. 4.3(b) shows a 3D illustration of the areas covered by each pixel. $A'B'C'D'$ is a rectangle proportional to and in parallel with $ABCD$, with the lower side touching the floor plane and the line connecting the centre of $ABCD$ and the centre of $A'B'C'D'$ crosses O. Since $\overline{AB} || \overline{CD}$, according to the proportionality theorem $\frac{\overline{A'B'}}{\overline{EF}} = \frac{\overline{OT'}}{\overline{OG}}$. Since $OQ'T'$ is an isosceles triangle, $\overline{OT'} = \overline{OQ'} = \frac{H_{\mathrm{c}}}{\cos(\theta_{\mathrm{T}} - \theta_{\mathrm{FoV}}/2}$ and $\overline{OG} = \frac{H_{\mathrm{c}}}{\cos(\theta_{\mathrm{T}} + \theta_{\mathrm{FoV}}/2}$. Accordingly, if the length of $\overline{A'B'}$ is α then the length of $\overline{EF}$ is given by:

$$\beta = \frac{\cos\left(\theta_{\mathrm{T}} + \frac{\theta_{\mathrm{FoV}}}{2}\right)}{\cos\left(\theta_{\mathrm{T}} - \frac{\theta_{\mathrm{FoV}}}{2}\right)} \alpha. \tag{4.13}$$

Knowing that the length of $\overline{OT}$ is $g = \sqrt{(aU/2)^2 + f^2}\}$, and due to proportionality of OTQ and $OT'Q'$ we have:

$$\alpha = \frac{V H_{\mathrm{c}}}{g \cos(\theta_{\mathrm{T}} - \theta_{\mathrm{FoV}}/2)} a, \tag{4.14}$$

where V is the number of photodetectors in a row of the camera sensor.

The area boundary on the floor plane, which each photodetector covers in $\vec{x}$ direction, is given by:

$$y_v(x) = \frac{v(\beta - \alpha)}{V x_U} (x - x_0) + \frac{v\alpha}{V}, \qquad -\frac{V}{2} \le v \le \frac{V}{2}. \tag{4.15}$$

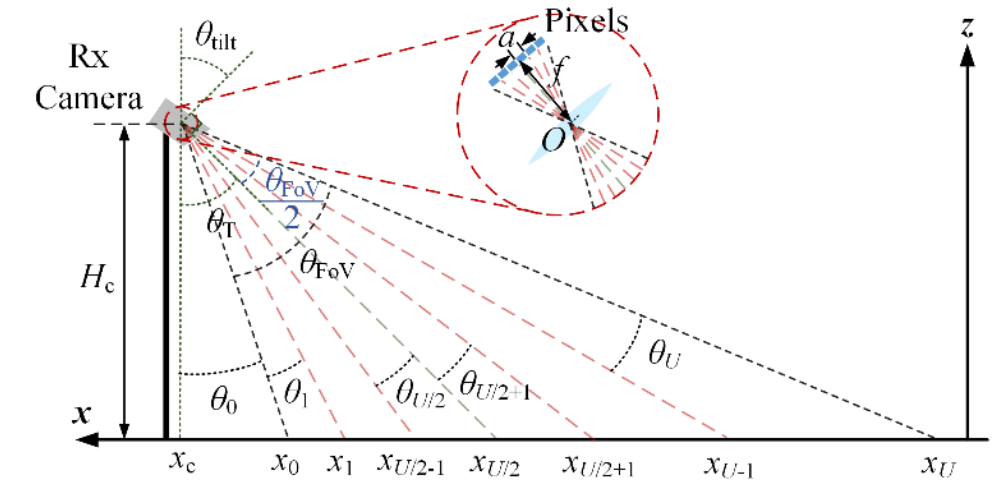

(a)

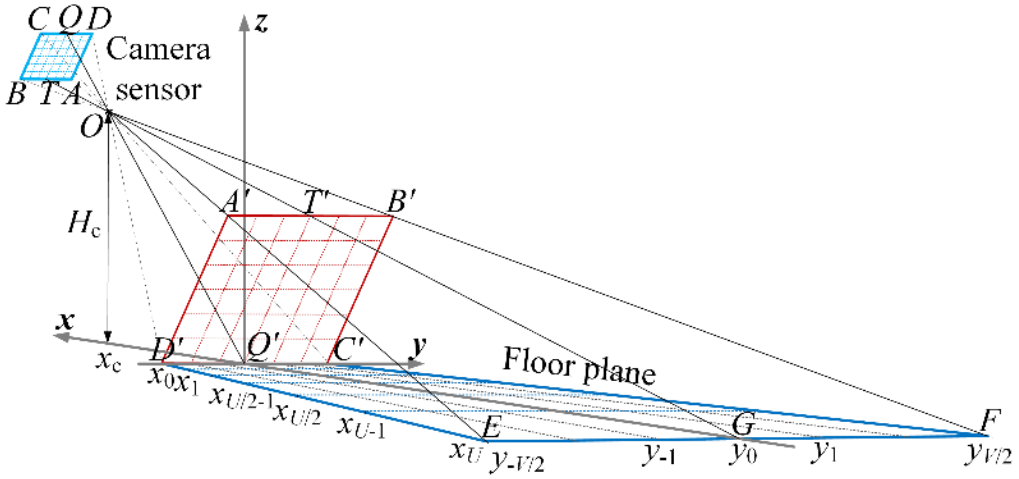

(b)

Figure 4.3: (a) Side view of areas that each photodetector covers, and (b) 3D view of areas covered by PD.

In this work, the main noise sources considered are the photocurrent shot noise, readout noise (i.e., the thermal noise in the readout circuit), dark current shot noise, and fixed pattern noise[173, 174], which are modelled as an additive GDRV [171]. Note that, in IS-based Rxs the dark current and quantization noise sources are negligible and therefore are ignored and only the shot and reset noise sources are considered. Hence, the total noise $\sigma_N^2 = \sigma_{res}^2 + \sigma_{shot}^2$. Here, we consider the OOK-

NRZ signal format, where the BER is defined as:

$$\text{BER} = Q\left(\frac{\mu_1 - \mu_0}{\sigma_1 + \sigma_0}\right), \tag{4.16}$$

where $Q(.)$ is Gaussiang Q-function, μ_1 and μ_0 are the mean of bit "1" and "0", respectively, and $\sigma_1 = \sqrt{\sigma_{\text{res}}^2 + \sigma_{\text{shot}}^2}$ and $\sigma_0 = \sigma_{\text{res}}$ are the variance of bit "1" and "0", respectively.

Given thatthe desired Tx is the l-th, lights from other Txs can results in crosstalk due to overlapping optical footprints, which will affect the link performance depending on the size of the overlapping area. The overall received signal at the IS with crosstalk from $M-1$ interfering sources is given by:

$$\begin{aligned} I(u,v) = \int_{x_{u-1}}^{x_u} \int_{y_{v-1}(x)}^{y_v(x)} \sum_{q=1, q\neq l}^{M} P_{\text{t},q} x_{\text{op},q} R_{\text{t},q}(x,y) \\ \times \frac{\mathrm{d}A}{d_{\text{t},l}^2(x,y)} R_{\text{r}}(x,y) \frac{A_{\text{lens}}}{d_{\text{c}}^2(x,y)} \cos\big(\psi_{\text{c}}(x,y)\big). \end{aligned} \tag{4.17}$$

From (4.19) we can see that, since a fixed level of illumination for streetlights is expected only two parameters can be used to reduce the level of interference, i.e., the distance between Txs and the viewing angle of the Txs. By increasing the spacing between the desired and the interfering Tx, the term $\alpha_{\text{t-f},l}(x,y)$ decreases, hence reducing the interference level.

4.3 System Model

In this chapter, we consider a $2 \times N_{\text{r}}$ OCC system as a simplified version of the real system, the results of which can be applied to an $N_{\text{t}} \times N_{\text{r}}$ system. In addition, this

system represent the scenarios where only two Txs interfere such as: (*i*) two vehicles approaching a crossroad (see Fig. 4.1(a)), where only headlights of vehicles A and B interfere; and (*ii*) in urban areas where the streetlights might are blocked by tall trees (see Fig. 4.1(e)) where the footprint of the streetlight only interferes with the vehicle's headlight, etc. The schematic block diagram of the proposed system is shown in Fig. 4.4(a).

At the Tx, a OOK-NRZ input data stream d_l , where l = 1, 2, is applied to the packet generator (see Fig. 4.4(c)); the output of which is differentially encoded with $x_{k,l} = x_{k-1,l} \oplus b_{k,l}$ prior to intensity modulation of LEDs (see Fig. 4.4(a) in order to enable frame subtraction at the Rx side. Here, $\oplus$ represents the modulo-2 addition, $b_{k,l}$ is the output of packet generator block and $x_{k,l}$ is the output of differential signalling block. Note that, the initial state of modulo-2 addition x_0 is set to 0, and R_b is set to half of the camera frame rate R_f. Two rectangular boxes (RB_1, RB_2) located in front of LEDs are used to project a desired illumination patterns on to the floor for the propose of experimental investigation in this research work, see Fig. 4.4(a). For each Tx, the LED light source create a beam angle of $\phi_l = 2 \times \tan^{-1}\left(\frac{w_{RB,l}}{2H_{RB,l}}\right)$, where $w_{\mathrm{RB},l}$ and $H_{RB,l}$ represent the width and height of boxes, respectively, and l = 1, 2. Fig. 4.4(c) illustrates a proposed packet structure, which is composed of *preamble* (64-bit), *pilot* (N_t-bit), where N_t is the number of Txs, and *payload* (1000-bit) as in [9]. Note that, a common *preamble* for both Txs can be used since LEDs are synchronized. The *pilot* is used as a mask to determine the position of the reflected light beams from the floor, and its length depends on the number of Txs. Here, we have used two sequences of [0, 1} and [0, 0} for Tx_1 and Tx_2, respectively, which also represent the Tx's identity.

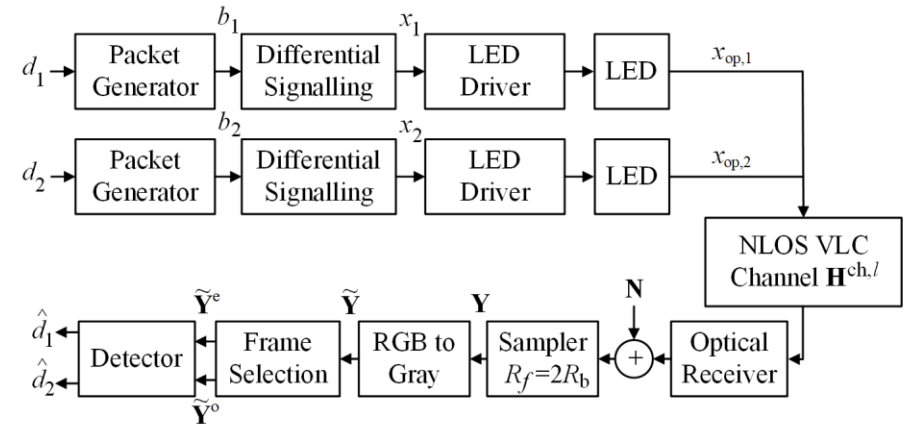

(a)

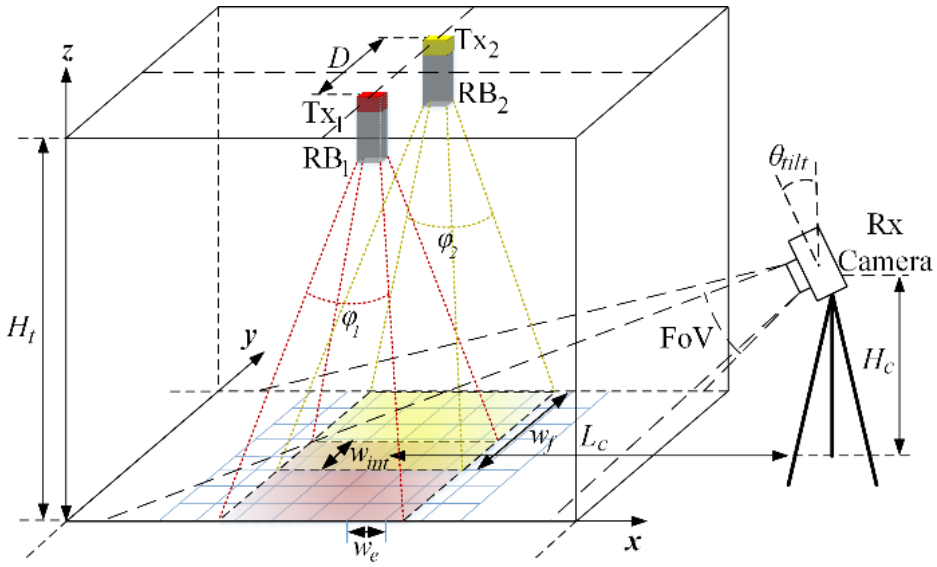

(b)

(c)

Figure 4.4: Proposed OCC system: (a) schematic block diagram, (b) system orientation with LEDs' illumination patterns, and (c) proposed packet format. The camera is used to capture reflected lights.

At the Rx, a typical digital camera is used to capture temporal samples of the reflected lights from the floor at a sampling frequency equal to the frame rate $R_{\mathrm{f}} = 2R_{\mathrm{b}}$. Each frame is an 8-bit matrix with dimensions of $U \times V$ per primary colour, where U and V are the numbers of pixels of the frame in vertical and horizontal directions, respectively. Note that, the sampling duration is equal to T_{exp}.

A time frame of the system is depicted in Fig. 4.5. The bit duration of the OOK modulation is set to $T_{\mathrm{b}} = \frac{2}{R_{\mathrm{f}}}$ in order to avoid inter-symbol interference (ISI), hence each bit is sampled twice to ensure that we always have a sample of the signal between the rise and fall edges (see Fig 4.5(c)). Accordingly, we define the samples in terms of two sets of odd and even samples prior to applying the detection process independently (see Figs. 4.5 (d) and (e)). Note that, the set with a lower BER is considered.

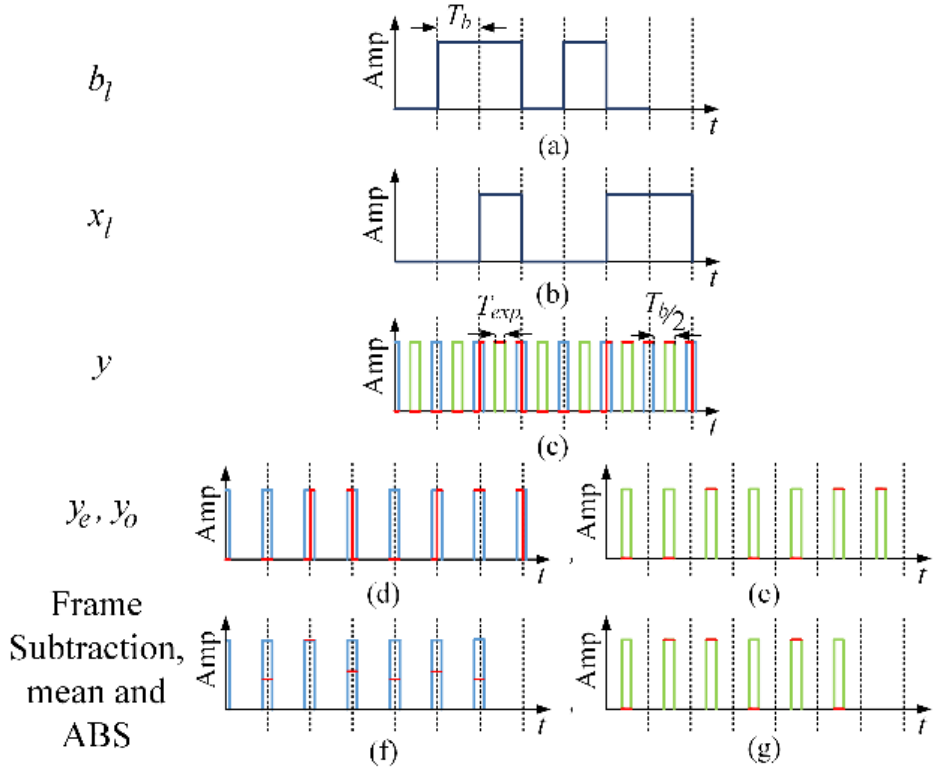

Figure 4.5: A time frame of the system showing the procedures taking place on the input signal in each stage: (a) output of the packet generator, (b) differentially encoded data, (c) sampled data at $R_{\mathrm{f}} = 2R_{\mathrm{b}}$ using the camera, (d) even frames of the sampled data, (e) odd frames of the sampled data, (f) absolute value of the mean of subtracted even frames, and (g) absolute value of the mean of subtracted odd frames. Red lines show the value of the sampled data with the time.

4.4 Detection Algorithm

The detailed detection process at the Rx is best illustrated by a flowchart in Fig. 4.6.

Following grayscale conversion, frame subtraction is first carried out for all odd frames followed by the even frames for the entire video frame (i.e., $U \times V$ pixels) as given by:

$$\boldsymbol{\Delta}\widetilde{\mathbf{Y}}_k^{\mathrm{o}} = \widetilde{\mathbf{Y}}_k^{\mathrm{o}} - \widetilde{\mathbf{Y}}_{k-1}^{\mathrm{o}}, \tag{4.18}$$

where $\mathbf{Y}_k^{\mathrm{o}}$ and $\mathbf{Y}_{k-1}^{\mathrm{o}}$ are the subsequent frames. The absolute values of the mean of $\boldsymbol{\Delta}\widetilde{\mathbf{Y}}_k^{\mathrm{o}}$ for the entire array is given by:

$$S_k = \left|\underset{i,j}{\mathrm{mean}}\left(\boldsymbol{\Delta}\widetilde{\mathbf{Y}}_k^{\mathrm{o}}(i,j)\right)\right|, \qquad i = 1, \dots, U, \qquad j = 1, \dots, V. \tag{4.19}$$

Next, S_k is compared with a threshold level th_{pr} to regenerate the *preamble* sequence, which is then correlated *preamble* bits. On achieving pattern matching, $Flag_{\mathrm{pr}}$ is set to 1, and a pixelated version of the mask frames is created based on averaging over blocks of $m \times n$, where $m = n = 10$ pixels, which is given by:

$$\begin{gathered} \Delta y'_{\mathrm{pi},l}(u,v) = \underset{u,v}{\mathrm{mean}}\big(\Delta y_l(u,v)\big), \\ u = (\xi - 1)m + 1, \dots, \xi m, \qquad v = (\zeta - 1)n + 1, \dots, \zeta n, \\ \xi = 1, \dots, I/m, \qquad \zeta = 1, \dots, J/n. \end{gathered} \tag{4.20}$$

Based on the mask two strategies can be pursued:

- **HS/EGC:** In HS/EGC algorithm, every element of $\Delta y'_{\mathrm{pi},l}(u,v)$ is binarized to form a $U \times V$ matrix. The (u,v)-th pixel binary value of the l-th mask frame is given by:

$$\begin{gathered} y_{\mathrm{pi},l}(i,j) = \begin{cases} 1, & \Delta y'_{\mathrm{pi},l}(i,j) \geq th_{\mathrm{pi}} \\ 0, & \Delta y'_{\mathrm{pi},l}(i,j) < th_{\mathrm{pi}} \end{cases} \\ l = 1, \dots, N_{\mathrm{pi}}, \qquad u = 1, \dots, U, \qquad v = 1, \dots, V, \end{gathered} \tag{4.21}$$

  where th_{pi} is the threshold level for the mask.

- **HS/MRC:** Unlike HS/EGC, here there is no need for binarization, i.e., each mask is employed in the current form.

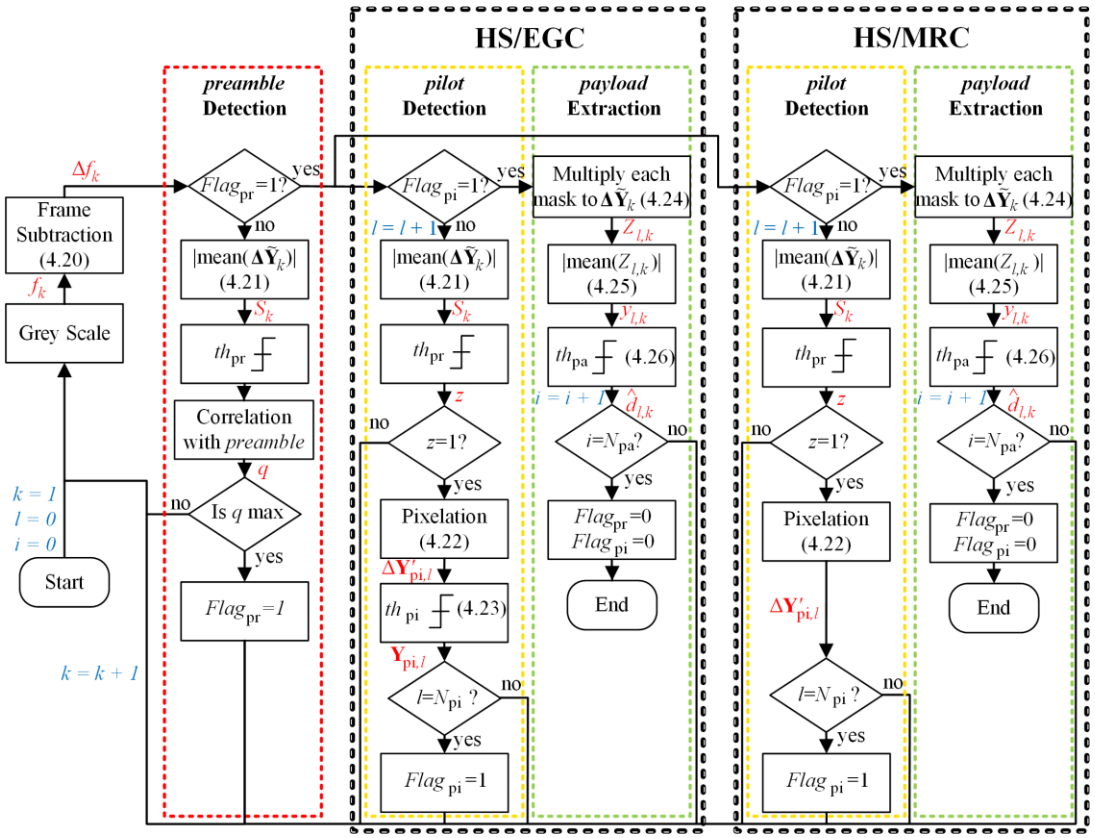

Figure 4.6: A flowchart illustrating the detection process to recover the data.

Finally, for data recovery part of the subtracted frame is multiplied by a $U \times V$ mask matrix for Tx_1, so that all non-illuminated pixels are set to zero as given by:

$$\mathbf{Z}_{l,k} = \left(\Delta\tilde{\mathbf{Y}}_k^{\mathrm{o}}.\right)\mathbf{Y}_{\mathrm{pi},l}, \tag{4.22}$$

where dot represents the elementwise product of matrices. This procedure is performed for $N_{\mathrm{pi}} = 2$ times in this case and then the pilot extraction stage flag, $Flag_{\mathrm{pi}}$, is toggled to one. The mean of $\mathbf{Z}_{l,k}$, which is a scalar number, is given by:

$$y_{l,k} = \underset{u,v}{\mathrm{mean}}\left(Z_{l,k}(u,v)\right). \tag{4.23}$$

$y_{l,k}$ is then compared with a threshold level th_{pa} to regenerated the transmitted data

stream as given by:

$$\hat{d}_{l,k} = \begin{cases} 1, & y_{l,k} \geq th_{\text{pa}} \\ 0, & y_{l,k} < th_{\text{pa}} \end{cases}. \tag{4.24}$$

4.5 Experimental Results

Fig. 4.7 shows the experimental setup for evaluation of the proposed system. According to [175], to ensure a confidence level CL for a target BER, the number of bits required to be transmitted can be calculated as:

$$N_{\text{pa}} = \frac{-\ln(1-CL)}{\text{BER}}. \tag{4.25}$$

Therefore, to achieve a *CL* of 99.99% and meet the 7%-overhead FEC limit of 3.8×10^{-3}, ten packets each contained a pseudo random OOK-NRZ pattern of length 1000 bits as payload, i.e., a total of 10000 *payload* bits, was generated using a TTi TGA12104 arbitrary waveform generator.

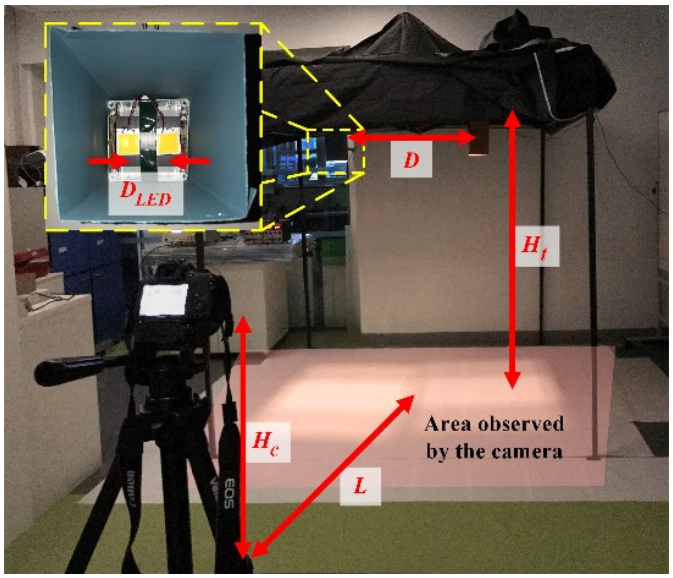

Figure 4.7: Experimental setup for the proposed system and the light source shown in the inset. The floor surface is covered by sheets of white paper and the red-highlighted area is the area that the camera observes.

Two identical light sources each composed two LUSTREON 4W 48led chip-on-board LEDs (COB-LEDs) mounted on a heat sink were placed within the tent at a height of 1.8 m and a distance of 1 m from each other. The illumination profiles of the light sources were similar to Lambertian emission pattern of $R_{\mathrm{t}}(\theta) = \frac{(m_{\mathrm{t}}+1)}{2\pi}\cos^{m_{\mathrm{t}}}(\theta)$, where $m_{\mathrm{t}} = 1$ and $2/3$ in y and x directions, which is equivalent to the viewing angles of $\varphi_{\mathrm{y},l} = 60^{\mathrm{o}}$ and $\varphi_{\mathrm{x},l} = 70^{\mathrm{o}}$, respectively, see Fig 4.8. The LEDs have linear optical power-current characteristics with a wide current dynamic range of 300 mA. A rectangular box (RB) was placed on each Tx to control the viewing angle in order to comply with different realistic scenarios. The floor surface was covered by sheets of white paper. Fig. 4.9(a) shows the light source's normalized illumination footprint on the floor plane, which is measured using an optical power meter. Note, since the optical power meter is calibrated on a narrow range of wavelengths, a blue filter was mounted on the LED to measure the blue part intensity of the light. Then, a spectrometer was used to measure the spectrum of the light with and without blue filter and hence calibrating the measurements for the white light. Note that, the illumination level of reflected and diffracted light from the RBs and their edges, respectively were about 10% of the maximum illuminance level of the light source. The floor surface area of 130×130 cm is divided into a number of segments of size of 3×3 cm, and the normalized measured reflection pattern of light reflected from each segment at a distance of 50 cm in the polar plot is depicted in Fig. 4.9(b), which matches with the normalized 1$^{\mathrm{st}}$ order Lambertian emission pattern. Note, in order to minimize the reflection from the unwanted surfaces, the aforementioned piece of white paper was placed on a large sheet of black fur. We observed the same profile in every segments.

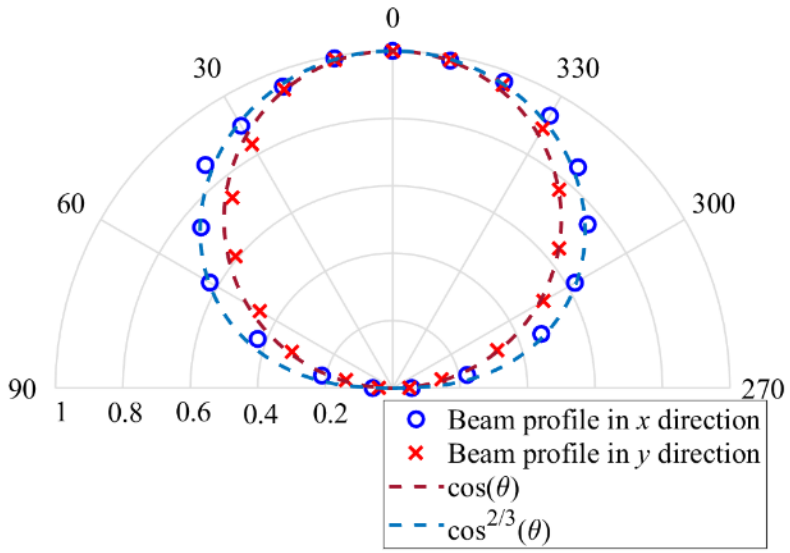

Figure 4.8: Normalized beam profile of the light source in x and y dimension and the fitted Lambertian curves with m = 1 and m = 2/3.

A camera (Canon Rebel SL1 EOS 100D) is used to capture a 5.8 minutes long video stream at the RGB-coloured HD resolution (i.e., 1280×720), and at 60 fps. Each video file is composed of 10 packets of 1066-bit long, which corresponds to a 5.8 minutes video stream. The captured video is then processed off-line in the Matlab, where subtracted frames are pixelated over blocks of 10×10 pixels in order to detect the mask. By this approach, we reduce the noise variance by ~100, thus leading to a clearer mask. As discussed in Chapter 3, three parameters determine the exposure level of pixels: (*i*) the shutter speed or T_{exp}; (*ii*) ISO – which determines the sensitivity of the IS; higher ISO leads to increased brightness of the captured image, thereby increasing the level of perceptible shot noise; and (*iii*) the aperture – which controls the amount of light being captured and limits or widens the depth of field. Consequently, objects located outside this range will appear hazy in the image. In NRS-based OCC, the transmission rate is usually limited to R_{f} (in this work it is limited to half of R_{f}). All the key system parameters are shown in Table 4.1.

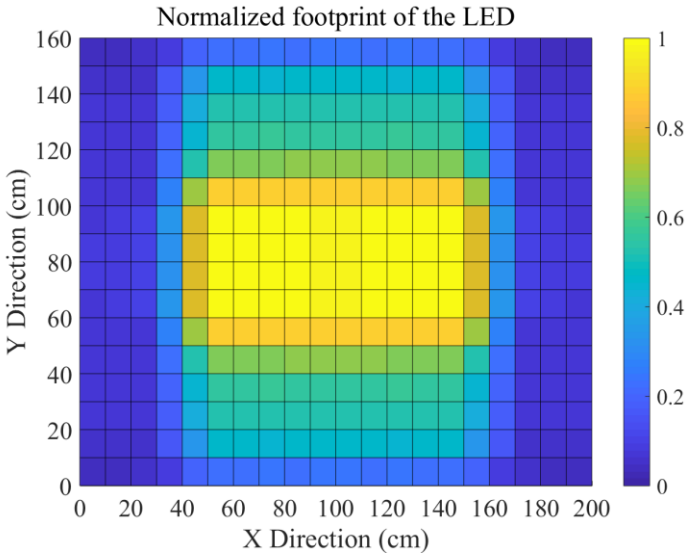

(a)

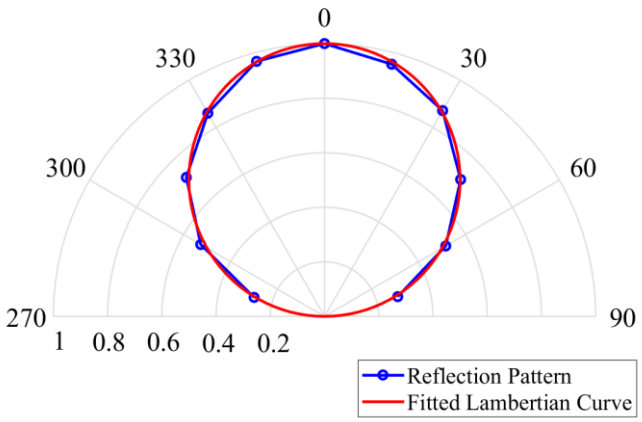

(b)

Figure 4.9: Normalized: (a) footprint of the LED on the floor plane, and (b) reflection beam profile.

Table 4.1. System Parameters

Symbol	**Description**	**Value**
H_t	Height of the Tx	1.8 m
D	Distance between two Txs	1 m
N_{pa}	Number of payload data bits	1000 bits
N_{pi}	Number of mask bits	2 bits
N_{pr}	Number of *preamble* bits	64 bits
D_{LED}	Distance between two COB-LED	6 cm
R_b	Transmitter bit rate	30 bps
L_s	Link ground span	3 m

ρ	Reflection coefficient of the floor	0.67
H_{c}	Height of the camera	1.3 m
R_{f}	Camera frame rate	60 fps
θ_{tilt}	Tilt angle	20°
f	Camera focal length	18 mm
L_{RB}	Length of the box	18 cm
w_{RB}	Width of the box	13 cm
A_{pixel}	Pixel area	18.4 μm^2
A_{IS}	Image sensor area	22.3×14.9 mm
$U \times V$	Camera frame resolution	1280×720

Fig. 4.10 shows the measured BER as a function of the transmit power for different values of ISO, HS/EGC, HS/MRC, and simulation results for HS/EGC, an aperture of $f/4$, a shutter speed of $1/100$ s, a L_{s} of 5 m, and a camera tilt angle of 20°. At a BER of 3.8×10^{-3} (i.e., the FEC limit) the power penalties are ~3 and ~6 dB for ISOs 3200 and 1600, respectively compared to ISO 6400. This is because in JPEG format at low illumination levels, the intensities below a certain value are set to 0, i.e., the signal will be clipped from the lower side, hence reduced SNR (on average). Therefore, when the signal was amplified before ADC using ISO levels, the signal moved away from the clipping point that resulted in increased SNR compared to the first ISO level. Moreover, the results of HS/MRC are very close to HS/EGC, which is attributed to the fact that the intensity of the pixels in the region of interest did not vary significantly.

In order to perform simulation, we first set the camera 0.5 m away from and on the axis of a Luxeon rebel LED on a defocused mode. We took an average over the circle of confusion of 50 images of RAW and JPEG formats. We also measured the received power at the same point using a power meter along with blue filter and a spectrometer and rescaled using the ratio of the aperture area of the camera to the effective photosensitive area of the power meter. Figure 4.11(a) demonstrates the output

intensity after ADC for RAW and JPEG images against the received power per pixel for the ISO of 800, $T_{\text{exp}} = 0.004$, $f = 18$ mm and aperture stop of $f/5.6$. We performed this experiment for different cameras settings.

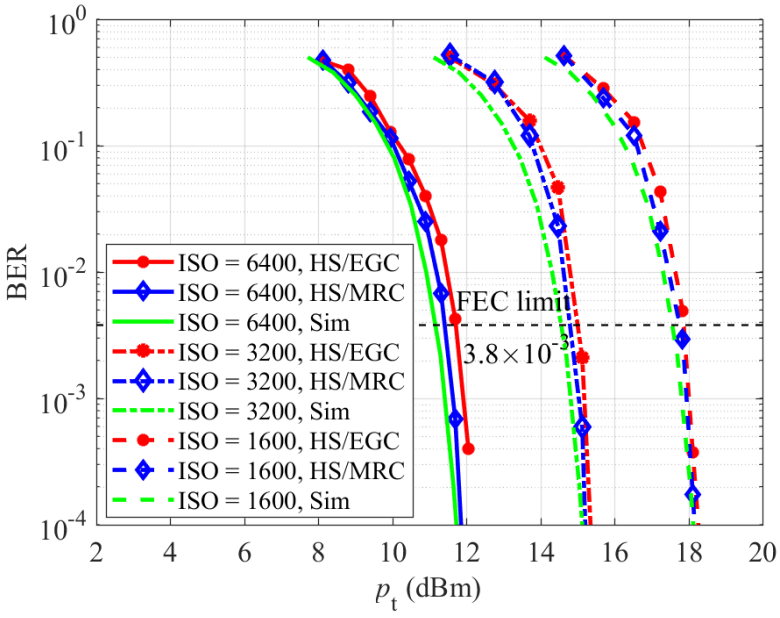

Figure 4.10: BER vs. the transmit power for different values of ISO, an aperture of f 4, a link span of 5 m, and an exposure time of 1/100 s in the focused mode.

To evaluate the variance of the noise as a function of the mean value of the pixels, we performed an experiment using an OSRAM Orbeos OLED panel at a very close range from the camera. The camera was defocused to reduce the impact of cell borders of the OLED panel. ISO, T_{exp}, and aperture was set to 6400, 1/100 ms, and *f*/5.6, respectively. The input current of the OLED was increased gradually and for each current setting 20 RAW images were captured. For each RAW image, an area of 1000×1000 pixels was chosen at the centre of the picture, i.e., 2e+7 samples were chosen in total. A Gaussian curve was fitted to the histogram of the pixel intensities and the variance of the noise was estimated. The experiment was performed for a range of camera parameters. Figure 4.11(b) shows the variance of the noise as a function of mean value of the pixels and a linear-fitted curve. The results show a close match with

the linear curve, where at $\mu = 0$ the variance is not zero. Hence, the dominant noise in low exposures is the signal independent noise sources (i.e., readout noise and reset noise) whereas in high exposures signal-induced noise (i.e., photocurrent shot noise) is dominant.

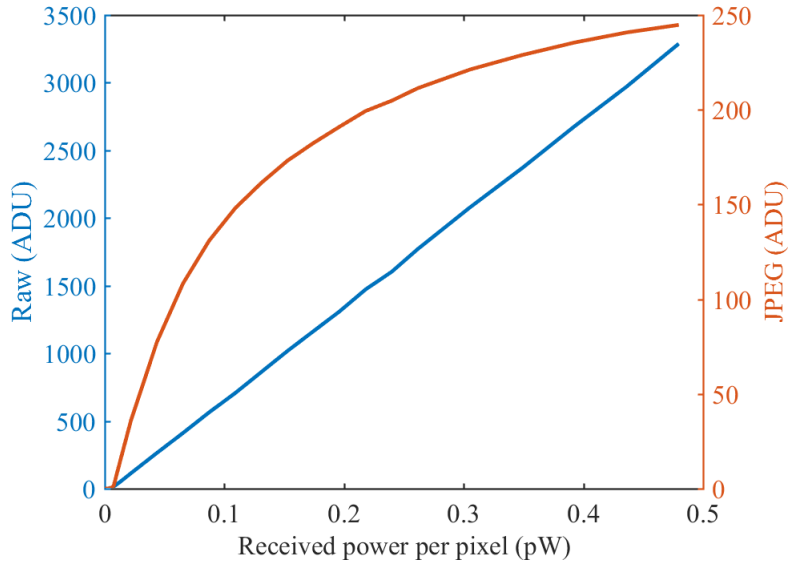

(a)

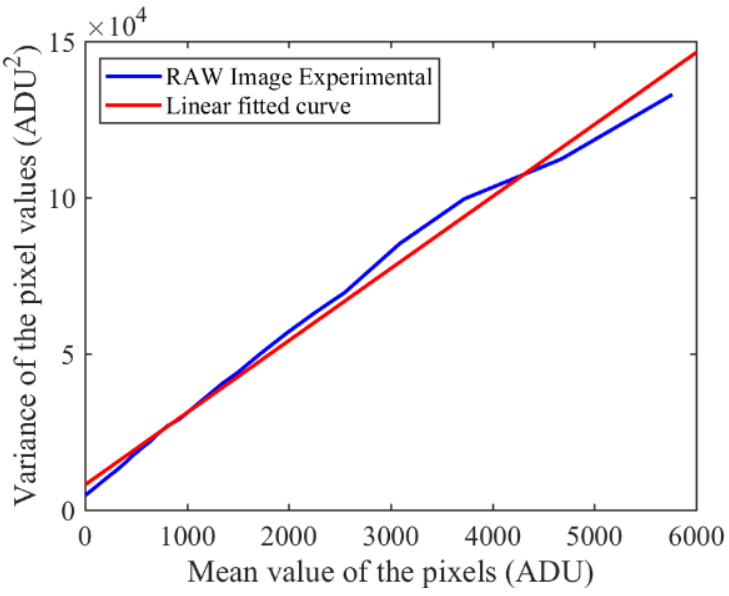

(b)

Figure 4.11: (a) Output intensity value of the pixel after ADC in RAW and JPEG format, and (b) variance of the pixel intensity as a function of the mean intensity of the pixel at ISO of 6400 for RAW images.

Next, we considered T_{exp} of the camera for a given ISO and under the focused condition. Figure 4.12 depicts the BER against the transmit power for a range of T_{exp} (i.e., 1/100, 1/200, and 1/400 s) and for an aperture of $f/4$. At a BER of 10^{-3}, we observe a 3 dB power penalty for every doubling of T_{exp} toward T_{exp} of 1/100. Note that, increasing and decreasing T_{exp} can lead to a higher chance of capturing the rise and fall time edges of OOK-NRZ and decreasing the exposure level of the recorded image, respectively. The same trend in the BER performance is also observed for a range of camera aperture of $f/4$, $f/5.6$, and $f/8$ at $T_{\text{exp}} = 1/100$ s.

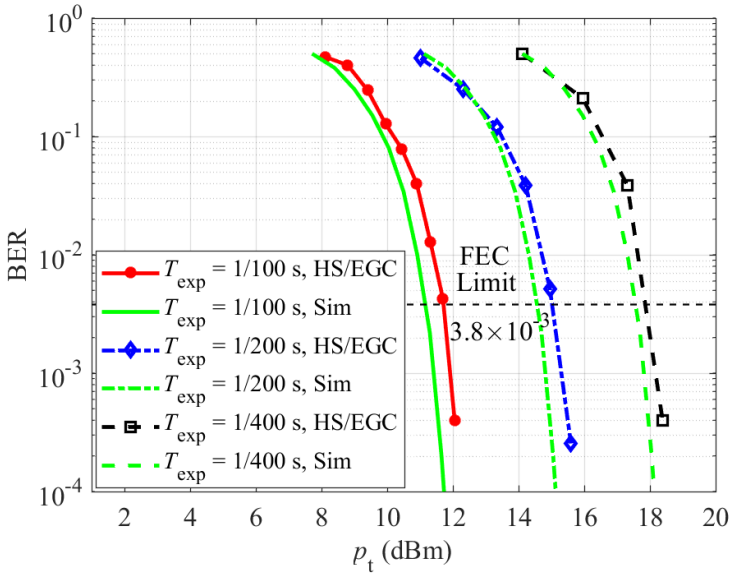

Figure 4.12: BER vs. the transmit power for different exposure times, an aperture of *f*/4, a link span of 5 m, and ISO of 6400 in the focused mode.

To find the impact of interference from other sources, we used the following parameters for the camera $T_{\text{exp}} = 1/100$ ms, aperture of $f/4$ and ISO of 6400. Here, we define the intersection ratio $r_{\text{int}} = A_{\text{int}}/A_{\text{f}}$, where A_{int} and A_{f} denote the intersecting and footprint area, respectively. We set the transmit power P_{t} to 25 dBm per the Tx. Fig. 4.13 shows the BER performance of the proposed link as a function of r_{int}. Note that, for $r_{\text{int}} > 0.5$, the BER is higher than the FEC limit, and therefore a reliable link cannot be established.

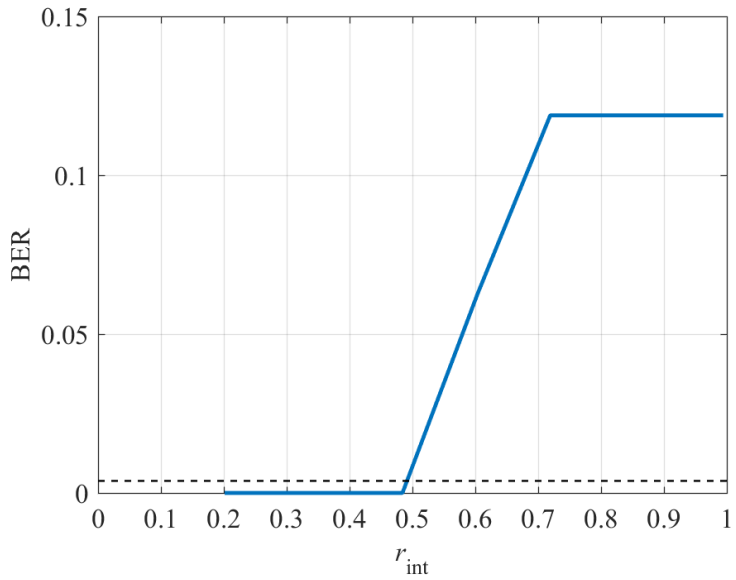

Figure 4.13: BER vs. width of intersection ratio , r_{int} when two transmitters are 1 m apart for ISO of 6400, aperture of f/3.5, exposure time of 1/100 s and P_t = 25 dBm.

4.6 Summary

In this chapter, we reported for the first time a novel $2 \times N_{\text{R}}$ OCC system, which extracts the data information from the NLOS beams. We suggested a comprehensive channel model for NLOS OCC in ITS, and proposed a dedicated packet structure and a detection methodology for extracting the data from the recorded video streams. Using an experimental test bed was developed for the proposed system, we showed that higher ISO levels and exposure times led to a reduced transmit power level by up to 6 dB for ISO of 6400 compared to ISO of 1600, and 3 dB for every doubling of the exposure time at a BER of 10^{-3}. We also showed that, the proposed system works well for the intersection ratio lower than 0.5.

Chapter 5 SPACE-TIME DIVISION MULTIPLEXING FOR NLOS VLC

5.1 Introduction

In the previous chapter, a $2 \times N_r$ NLOS OCC system with a small overlap illumination region was proposed for streetlight to vehicle communications. It was shown that, for an overlap level above a certain limit (i.e. 50%), the information could not be extracted. Hence, in scenarios where the overlap level increases (see Fig. 5.1(a)), if all the lights transmit data simultaneously then the information cannot be retrieved successfully.

One solution to this problem is to adopt the TDM scheme, where each streetlight is allocated a dedicated time slot along with SDM. Figures 5.1(a) and (b) depict the first and second time slots for the TDM-based approach in which only the first and the second groups can transmit information, respectively. Within the context of VLC systems, TDM is used for two reason of data communications [176], and visible light positioning system (VLPS) in indoor environments [177, 178]. In [179], the TDM was considered as an access scheme for the uplink in a full-duplex VLC local area network,

in which four time slots were assigned to each user and a time domain schedule was used to determine the source of the data. In [180] and [181], TDM was utilized to avoid inter-cell interference (ICI) in a VLPS. However, for a large-scaled VLC system, TDM is not an efficient technique due to increased level of delay (i.e., the latency), which is not desirable in data communications. To reduce the transmission delay in [182], a novel STDM technique was employed in a form of block encoding TDM, where LEDs lights within the room were grouped together in order to reuse the allocated time-slots, with each group transmitting data information in only one time slot.

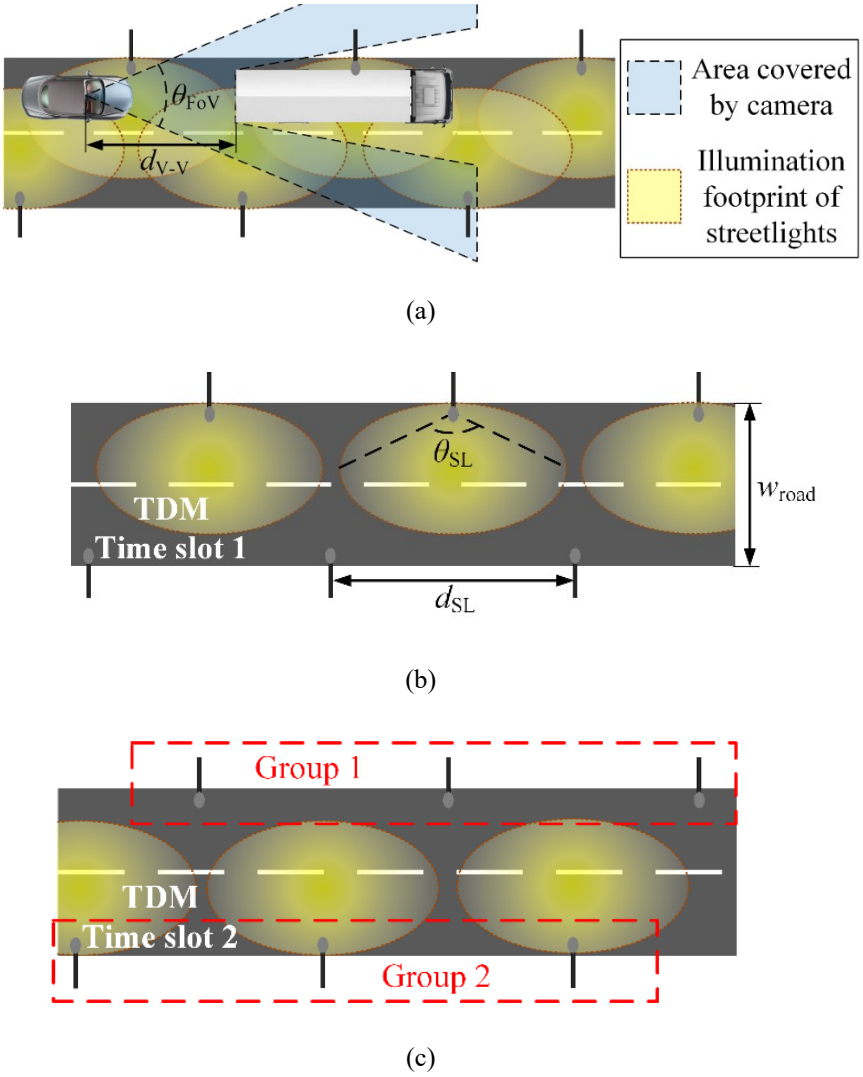

Figure 5.1: Arrangement of streetlights: (a) increased level of overlap, (b) TDM in the first time slot, and (c) TDM in the second time slot.

In this chapter, a method based on STDM for a $N_t \times N_r$ MIMO NLOS OCC is proposed and investigated, where light sources acting as Txs illuminate the floor surface in a grid form with some overlapping areas. In order to recover the transmitted data stream at the Rx from the captured images of light sources for both LOS and NLOS configurations we have developed and adopted the followings steps:

(i) Differential modulation and the frame subtraction schemes - at the Tx and the Rx, respectively in order to remove the unwanted background objects within frames;

(ii) Mask matching - to determine the optical footprint of the desired Tx in a given frame;

(iii) MIMO-based SDM and TDM schemes - are employed to spatially separate the Txs and recover the transmitted data;

(iv) EGC - to improve the SNR and the BER performance.

The proposed system is experimentally implemented and evaluated under different channel conditions. We show that, for link span L_s of 5 m, the transmit power P_t levels of 100 mW and 10 mW with and without the ambient light, respectively are required to achieve a BER of 10^{-3}, which is just below the forward error correction limit of 3.8×10^{-3}. In addition, we show that, there is no need for the Txs to be placed in focus, hence larger aperture sizes can be used. Moreover, we show that, in the MIMO system a power penalty of ~2 dB is imposed to the system.

5.2 System Model

The block diagram of the proposed system is shown in Fig. 5.2(a). In Chapter 4, it

was shown that, if the overlapping area of optical footprints is $> 50\%$ of the area of each optical footprint, the full recovery of the signal using a camera was not possible. Therefore, here we consider a TDM-based scheme where the Txs are divided into groups.

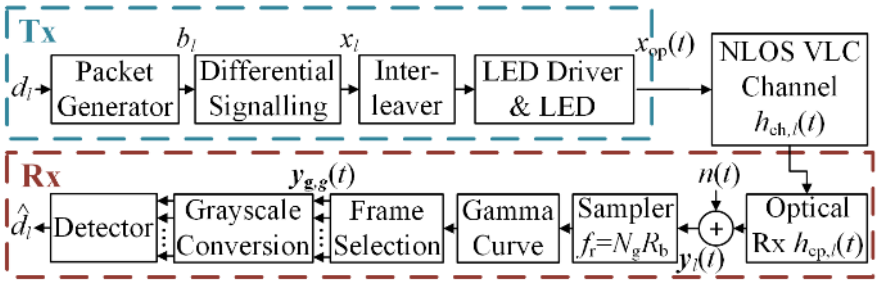

(a)

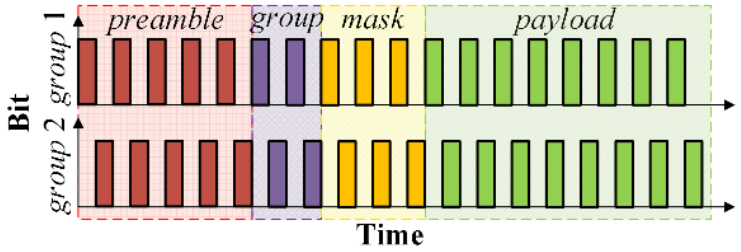

(b)

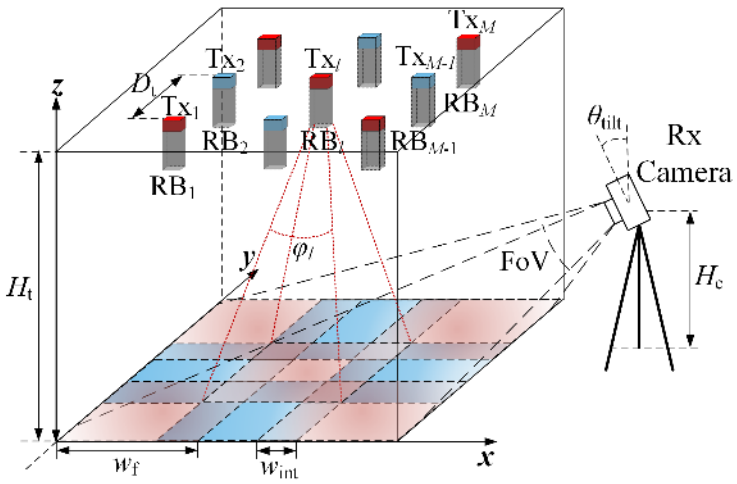

(c)

Figure 5.2: Proposed OCC system: (a) schematic block diagram, (b) proposed packet structure, and (c) system orientation with Txs optical footprints with two groups of Txs. The camera is used to capture reflected lights.

5.2.1 *Packet Generator*

To mark the beginning of the packet, a *preamble* sequence N_{pr} is added to N_{t} independent pseudo-random sequences of data (i.e., *payload*) d_l of length N_{pa} where $l = 1, \dots, N_{\mathrm{t}}$, using the packet generator block, see Fig. 5.2(b). Note, N_{p} length should be selected such that both the overhead and the likelihood of appearing in the *payload* which can be obtained as:

$$P_X(P \in D) = \sum_{i=1}^{\left\lfloor \frac{N_{\mathrm{pa}}}{N_{\mathrm{pr}}} \right\rfloor} \sum_{j=1}^{N_{\mathrm{pa}} - iN_{\mathrm{pr}}} \frac{\left(N_{\mathrm{pa}} - i\left(N_{\mathrm{pr}} - 1\right)\right)}{\left(N_{\mathrm{pa}} - iN_{\mathrm{pr}} - j\right)!\, i!\, j!}, \tag{5.1}$$

are reduced.

For a payload of length 1000 bits, a 64-bit *preamble* will give $P_X(P \in D) = 5 \times 10^{-17}$. The field *group* and *mask* are used for the Txs's group ID, and their positions, respectively as well as representing the Tx's ID, see Fig. 5.2(b).

5.2.2 *Differential Signalling and Interleaver*

The output of packet generator $b_{k,l}$ is differentially encoded with $x_{k,l} = x_{k-1,l} \oplus b_{k,l}$, where $\oplus$ denotes the modulo-2 addition, $x_{k,l}$ is the output of differential signalling block, and $x_{0,l} = 0$. To reduce the flickering effect, a bit by bit-based interleaver is used, in which the i-th bit of g-th group of Txs is followed by the i-th bit of the $(g+1)$-th group of Txs, and the $(i+1)$-th bit of the g-th group of Txs follows the i-th bit of the $(g-1)$-th group of Tx, see Fig. 5.2(b). Accordingly, for the Txs $R_b = MR_{\mathrm{f}}/2N_{\mathrm{g}}$, where M is the number of symbols per frame (for OOK-NRZ $M = 1$) and N_{g} is the number of Txs's group. Note, we have assumed that R_{f} is fixed, but for cameras with variable R_{f} the condition of $R_{\mathrm{b}} < \min(R_{\mathrm{f}})$ must hold. However, the

additional frames captured needs to be removed by means of thresholding.

5.2.3 *Light Source, NLOS OCC Channel, and Sampler*

Array LEDs located within rectangular boxes (RBs), see Fig. 5.2(c), are used to illuminate the floor with the required rectangular optical footprints, which is give as:

$$w_{\mathrm{f},l} = \frac{w_{\mathrm{RB},l}}{H_{\mathrm{RB},l}} H_{\mathrm{t}}, \tag{5.2}$$

where H_{t} is the height of the room and $w_{RB,l}$ and $H_{\mathrm{RB},l}$ are the width and the height of the l-th RB, respectively. Note, for the l-th Tx $(x_{\mathrm{t},l}, y_{\mathrm{t},l}, H_{\mathrm{t}})$ the viewing angle $\phi_l = 2 \times \tan^{-1}\left(\frac{w_{\mathrm{RB},l}}{2H_{RB,l}}\right)$.

At the Rx, the captured video streams of the reflected lights from the floor surface are processed frame by frame in the Matlab domain in order to recover d_l. The detailed channel response of NLOS OCC were given in Chapter 4. In offline processing, following the selection of frames, the received frame first is converted to the grayscale (see Chapter 3).

5.3 Detector

5.3.1 *Frame Subtraction*

Following the selection of odd and even frames, frame subtraction is first carried out for all frames per group, and then for frames of other groups for the entire video frame (i.e., $U \times V$) in order to eliminate the background objects in the image, as given by:

$$\boldsymbol{\Delta}\widetilde{\mathbf{Y}}_{k,g} = \widetilde{\mathbf{Y}}_{k,g} - \widetilde{\mathbf{Y}}_{k-1,g}, \tag{5.3}$$

where $\widetilde{\mathbf{Y}}_{k,g}$ is the matrix of the k-th frame of the g-th group.

The operation of the detection algorithm for the proposed system is best described by the flow chart shown in Fig. 5.3. The algorithm is composed of four stages of (*i*) *preamble* detection; (*ii*) *group* detection; (*iii*) *mask* detection; and (*iv*) *payload* extraction. Note, the first three stages are controlled using three flags of $Flag_{\mathrm{pr}}$, $Flag_{\mathrm{g}}$, and $Flag_{\mathrm{pi}}$, respectively. The initial value for all flags is set to zero.

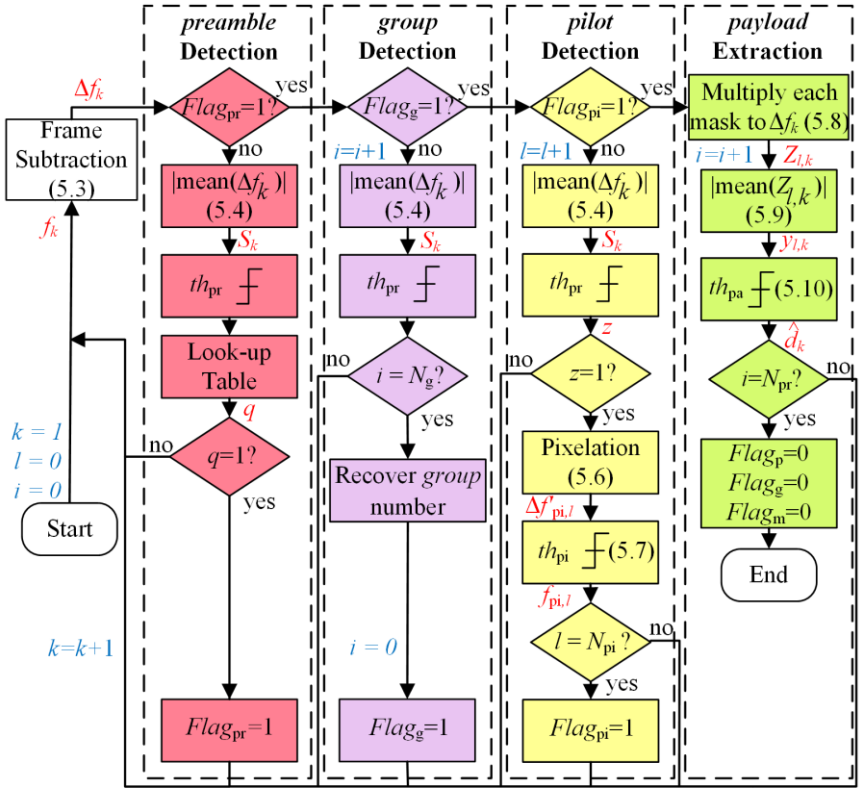

Figure 5.3: Flowchart of the proposed detection scheme composed of four stages: preamble, group, mask, and payload.

5.3.2 *Hybrid Selection/Equal Gain Combining*

In the first stage of detection, the average over the entire matrix of $\mathbf{\Delta}\widetilde{\mathbf{Y}}_{k,g}$ (i.e., EGC) is given by:

$$S_{k,g} = \left|\underset{i,j}{\text{mean}}\left(\Delta y_{k,g}(u,v)\right)\right|, \qquad u = 1,\dots,U, \qquad v = 1,\dots,V. \tag{5.4}$$

S_k is then compared with a threshold level th_{p} with the output given as:

$$R_{k,g} = \begin{cases} 1, & S_{k,g} \geq th_{\text{p}} \\ 0, & S_{k,g} < th_{\text{p}} \end{cases}, \qquad l = 1,\dots,M, \qquad i = 1,\dots,U, \qquad j = 1,\dots,V \tag{5.5}$$

$R_{k,g}$ is then correlated with preamble and when matched $Flag_{\text{pr}}$ is toggled to "1". The next step is to find the group ID, which together with the mask, represents the Tx's ID. Using (5.4) and (5.5) the detector determine N_{g} number of iterations and recovers the group number for all Txs in the same group all at the same time, and then $Flag_{\text{g}}$ is toggled to "1".

Once again S_k is compared with th_{p} to check for a mask within a particular frame. If $S_k > th_{\text{pr}}$, a pixelated version of $\mathbf{\Delta\widetilde{Y}}_k$ is generated by averaging over blocks of $m \times n$, which isgiven by:

$$\Delta y'_{\text{m},l,g}(u,v) = \underset{u,v}{\text{mean}}\left(\Delta y_{\text{m},l,g}(u,v)\right), \qquad u = (\xi-1)m+1,\dots,\xi m, \quad v = (\zeta-1)n+1,\dots,\zeta n, \quad \xi = 1,\dots,\frac{U}{m}, \quad \zeta = 1,\dots,\frac{V}{n}. \tag{5.6}$$

Lemma 1: For *N* number of independent normally distributed random variables of X_i, the mean and the variance of $Y = \frac{1}{N}\sum_{i=1}^{N} X_i$ are given by, $\mu_Y = \frac{1}{N}\sum_{i=1}^{N}\mu_X$ and $\sigma_Y^2 = \frac{1}{N^2}\sum_{i=1}^{N}\sigma_X^2$, respectively, where μ_X and σ_X^2 are the mean and variance of X_i, respectively.

Note that, with $n(t)$ considered as GRDV, from Lemma 1, it can be seen that by

taking the average over a block of pixels σ_X^2 decreases, radically. Figures 5.4(a) and (b) illustrates the probability mass function (PMF) of an arbitrary distribution of light for a row of subtraction frame before and after pixilation, respectively. For higher values of m and n, σ_X^2 decreases more, which represents a highly accurate mask. However, the resolution of the mask frame reduces, thus resulting in no detection of the signal from the Txs with footprints smaller than $(m \times n)$ pixels. Following pixelation, every element of $\mathbf{\Delta}\widetilde{\mathbf{Y}}'_{\mathrm{pi},l}$ is binarized forming a matrix of $U \times V$ as:

$$y_{\mathrm{pi},l}(u,v) = \begin{cases} 1, & \Delta y'_{\mathrm{pi},l}(u,v) \geq th_{\mathrm{pi}} \\ 0, & \Delta y'_{\mathrm{pi},l}(u,v) < th_{\mathrm{pi}} \end{cases}, \qquad l = 1, \dots, M, \\ i = 1, \dots, U, \qquad j = 1, \dots, V \tag{5.7}$$

where $y_{\mathrm{pi},l}(u,v)$ denotes the (u,v)-th pixel of the l-th mask frame.

Figure 5.4 depicts the process of mask frame extraction (c) after frame subtraction, (d) after pixelation, and (e) the output mask frame. Since masks are unique for each Tx, they also represent the Tx ID and refer to the area illuminated exclusively by the l-th Tx. Therefore, when a subtracted frame is element-wise-multiplied by the mask matrix, all pixels are set to zero if not illuminated by the l-th Tx. Otherwise, pixels remain unchanged. This procedure is performed for M frames and then the mask stage flag is toggled to "1".

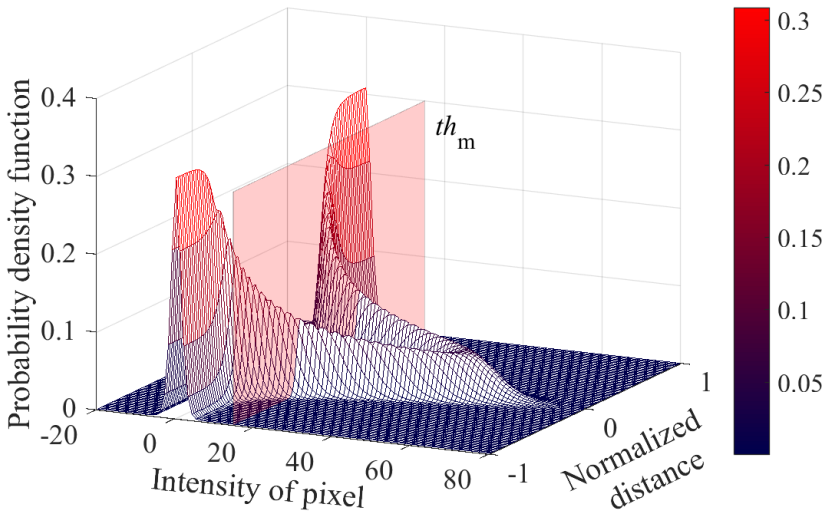
Probability density function
0.4
0.3
0.2
0.1
0
-20
0
20
40
60
80
Intensity of pixel
th_m
-1
0
1
Normalized distance
0.3
0.25
0.2
0.15
0.1
0.05

(a)

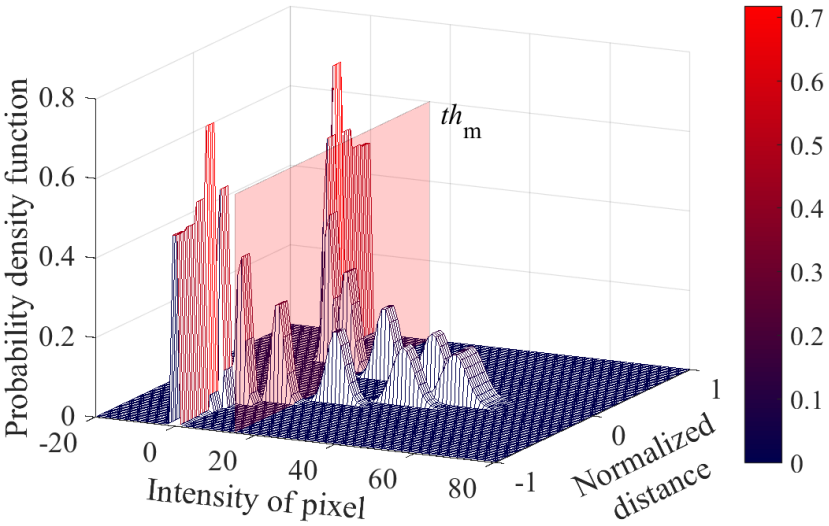
Probability density function
0.8
0.6
0.4
0.2
0
-20
0
20
40
60
80
Intensity of pixel
th_m
-1
0
1
Normalized distance
0.7
0.6
0.5
0.4
0.3
0.2
0.1
0

(b)

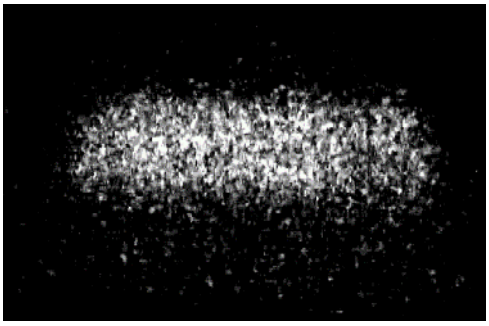

(c)

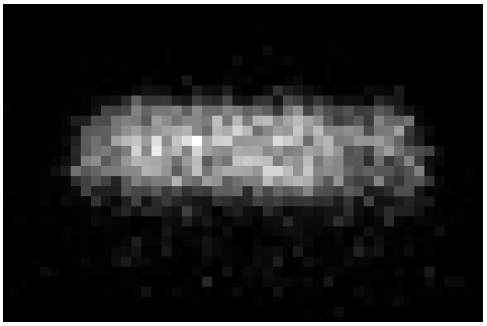

(d)

(e)

Figure 5.4: PDF of intensity of pixels of a row of the subtracted image with Lambertian Tx for pixilation: (a) before, and (b) after and mask frame extraction process: (c) frame subtraction (d) pixelation, and (e) mask frame.

5.3.3 *Mask Matching and EGC*

Finally, once masks are identified, the proceeding frames are element-wise-multiplied by all masks (i.e., SC) as given by (4.24) followed by (4.25) and (4.26). This approach increases the tolerance of the system to the noise; hence higher SNR levels.

5.4 Experimental Investigation

In this work, we investigate the impact of channel parameters on the system performance using a single Tx. Fig. 5.5 shows the experimental test-bed, which is used to evaluate the proposed system depicted in Fig. 5.2(c). For each Tx, an independent 1068-bit long packet composed of 64-bit preamble, 2-bit group, 2-bit mask, and 1000-bit payload created in Matlab was generated in the OOK-NRZ format using an arbitrary waveform generator (TTi TGA12104). For each Tx, we have used a Luxeon rebel LED positioned at the height of 1.8 m from the floor. The LED's beam have first

order Lambertian profile. An RB of the size $13 \times 13 \times 40$ cm^3 was used for each Tx to create a footprint of 0.6×0.6 m^2. The floor surface was covered by white papers with a reflection coefficient of $\rho \cong 0.67$. At the Rx, a Canon Rebel SL1 (EOS 100D) camera with a sensor size of 22.3×14.9 mm and a Canon EF-S 18-55 mm lens positioned 1.3 m above the floor level were used to record a ~5.8 minutes long RGB video stream with a 720p resolution at 60 fps. Note, The typical value of η in case of an advanced photo system sensor is ~ 0.37 [183]. The white balance was set to "off"-mode. The pixel area was 18.4 μm^2, θ_{tilt} was 20^o, and JPEG image resolution was 1280×720. The video streams were then processed off-line in Matlab. In the detection process, the mask was created by taking average over blocks of 10×10 pixels. The pixel dimensions of the CMOS-based IS are in the order of a few μm, which is far larger than the half wavelength of the LED light and thus the camera is able to serve as a spatial diversity Rx.

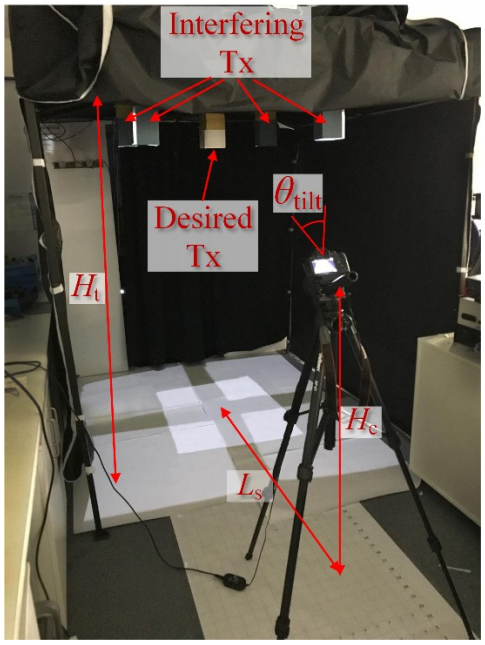

Figure 5.5: Experimental setup for the proposed system.

To assess the system BER as a function of P_t we captured video streams for $f = 18$

mm, aperture of $f/4$, $T_{\text{exp}} = 1/100$ s, ISO level of 6400, and L_{s} of 2 m, 5 m and 10 m for SIMO and $L_{\text{s}} = 2$ m for MIMO and a 40% overlap area, see Fig. 5.6. It can be seen that shorter L_{s} requires lower P_{t} for a given BER value. Note, increasing L_{s} results in reduced size of the optical footprint in the same rate as the drop in the signal level, hence the mean power in the illuminated area of the image is at a fixed level. Thus, based on Lemma 1, the power penalty due to L_{s} is related to the noise, which is averaged over a reduced number of pixels, and hence less clipping.The results also show that, a long-range and low data rate communications system can be established with a very low transmit power of ~15 dBm. Note, MIMO displays higher BER compared to SIMO, which is due to increased level of interference. Moreover, a 2 dBm power penalty was shown for the BER level of 10^{-3}. We attribute this to reduced probability of all interfering Txs being on at the same time.

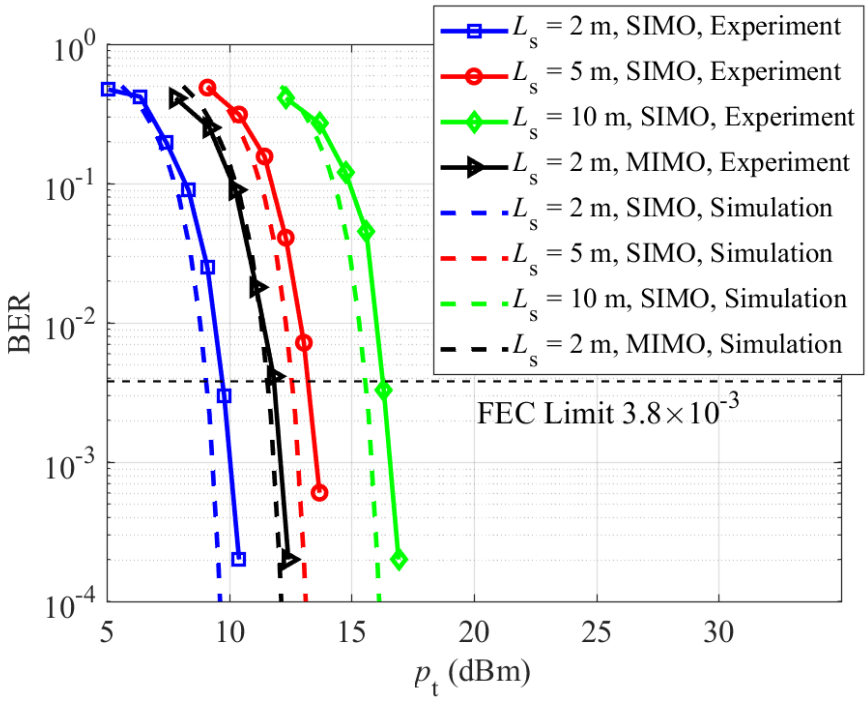

Figure 5.6: Predicted and measured BER vs. the transmit power for SIMO and MIMO and a range of L_{c}s.

Next, we located the camera at a distance of 5 m from the Tx. We measured the BER against P_{t} the transmit power for the aperture of $f/5.6$, T_{exp} of $1/100$ s, a ISO level of 6400, and f of 18 and 55 mm with and without the ambient light, see Fig. 5.7. To measure the performance of the system with ambient light, the desired Tx in Fig. 5.5 was transmitting information while the rest of the Txs were on without transmitting information with the overall intensity level of 20 dBm. For higher f the size of the reflection footprint increase covering more pixels with the aperture size become larger. Therefore, we observed no improvement in BER when zooming. The results highlight a ~10 dB improvement with the ambient light. This is due to the non-linear RAW to JPEG curve in the camera. Therefore, the ambient light does not degrade the system performance, but acts as a bias point at the Tx by shifting the signal into the linear region of the camera. Next, for the aperture of $f/5.6$, T_{exp} of $1/100$ s, and a ISO level of 6400 we measured the BER against P_{t} for focused and defocused cases with no ambient light, see Fig. 5.7. In this case, we observe a slight improvement in BER for the focused case. Changing the camera focusing distance slightly changes the focal point of the lens, but aperture remains the same. Accordingly, we observed a slight increase in the image size for the defocusing case, which resulted in light distribution over a higher number of pixels; hence lower SNR/pixel. We can, therefore, conclude that although large aperture leads to out-of-focus footprints, the system SNR performance improves. Note that, in order to reduce the frames processing time one option would be to use binning, where the image resolution is reduced by taking the average of $m \times m$ blocks [184].

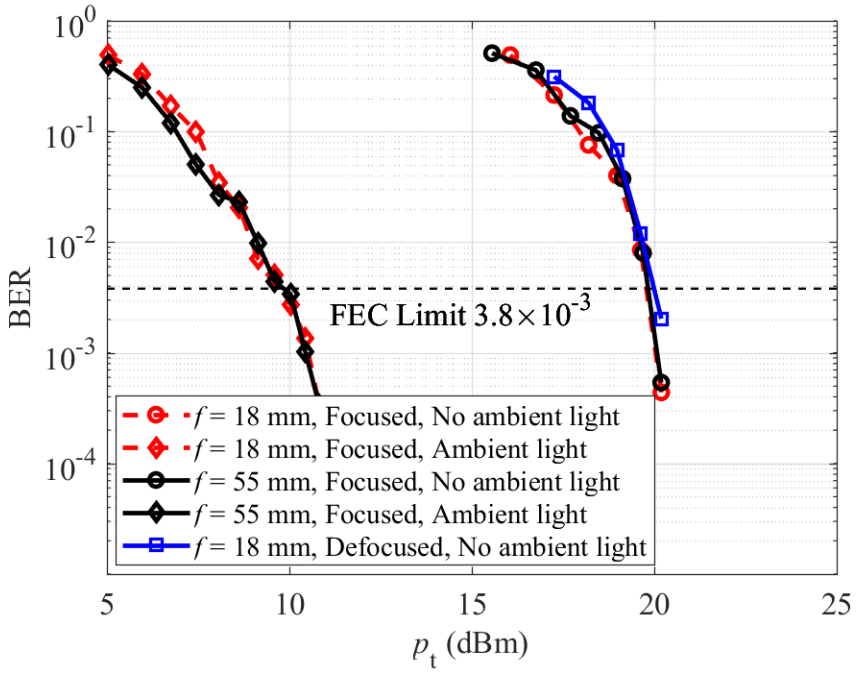

Figure 5.7: The BER vs. the transmit power for different focal lengths, ambient light levels, focused and defocused modes.

5.5 Summary

In this chapter, a novel NLOS MIMO STDM system was proposed for increased level of streetlight footprint overlap. To avoid the data loss due to crosstalk, STDM was adopted by allocating time slots to groups of Txs. We proposed a dedicated packet structure based on differential modulation in order to uniquely label the Txs and to ease the reception of the packets. A novel effective detection algorithm were proposed to effectively extract the information from video streams. In the proposed algorithm, frame subtraction and a mask were used to remove unwanted background objects, and to effectively locate reflections from a specified Tx to extract the data, respectively. An EGC technique was used to extract the data from the diversity Rx, which made the system more tolerant to the noise. The proposed system was evaluated under fixed

conditions and for different channel and camera parameters showing transmission over longer L_s under very low transmit power levels. We demonstrated that, the system performance improved in the presence of ambient light because of nonlinearity of the RAW to JPEG conversion process. Finally, we showed that, camera defocusing and FoV do not have a significant impact on the link performance, hence the camera aperture could be set to the maximum to take advantage of higher received power levels.

Chapter 6 COMPARISON OF COMBINING TECHNIQUES FOR NLOS OCC

6.1 Introduction

In Chapter 5, a detection technique employing differential signalling, STDM as the multiplexing technique and HS/EGC as the combining technique was proposed for a VLC-OCC scheme with large overlaps of the illumination footprints. However, using TDM the system throughput is reduced [185], more specifically in urban areas with a large number of light sources (i.e., streetlights, vehicles, display signs, etc.), see Fig. 6.1. In this situation, since the camera frame rate is low, selecting TDM as a multiple access technique is not the most efficient option. Considering that, in cameras the IS is a massive matrix of PDs, a zero forcing (ZF) equalization can be used as the combining technique while the channel access is SDM.

ZF, which eliminates the interference by directly forcing the interference terms to be zeros, has been investigated within the context of VLC for interference cancellation in multi-colour based MIMO and MISO links. In [186], the performance of ZF was

compared with ZF and successive interference cancellation (SIC) for a 3×3 MIMO WDM VLC system. It was shown that, when the optical band pass filter and the signal have the same full width half maximum (FWHM), the BER performance of ZF+SIC is half that of ZF. ZF was also adopted for multiuser MIMO-OFDM VLC and compared to minimum mean square error (MMSE) for a transmit power of 0 dBW offering a spectral efficiency of 0.5 bit/s/Hz or less [69]. The performance of ZF was theoretically investigated in [187] for MIMO CAP Rxs in VLC showing that for a BER of 3.8×10^{-3} combining it with optimally-ordered SIC (OSIC) improves the SNR by ~3 dB at a cost of increased complexity. In [188] a MISO downlink VLC system such as in airplane cabins, ZF was adopted showing a dynamic scenario compared to Tomlinson-Harashima precoding (THP) with the average per-user rate of ~0.3 bps/Hz lower at a 20 degrees of LED directivity. ZF was also adopted in a MU-MIMO underwater VLC system with spectral efficiency of ~15 bps/Hz compared to ~8 bps/Hz for a TDMA scheme [185].

Note, ZF is the preferred option provided the SNR is high. Under ill-conditioned channel matrix, ZF needs a large normalization factor, which will dramatically reduce the SNR [189]. Therefore, for low SNR, ZF cannot achieve a good performance since noise not the interference is dominant. Thus, the use of MMSE precoding. It is worth noting that, under higher SNR (i.e., high transmit power levels), the performance of ZF is the same as MMSE [69, 187]. Note, in linear MMSE precoding, the interference at the Rxs is not identically zero, thus the trade-off between noise and interference based their dominance at the Rx. In addition, in [190] ML detection was adopted for a generalised space shift keying signalling for an indoor MIMO VLC environment with a symbol error rate of 10^{-4} at a SNR of ~23.5 dB using 4 Rxs. A fast ML detection technique was proposed in [191] based on space-collaborative constellations, which

offers the same performance as the conventional ML detectors with a reduced complexity. However, ML detectors are too complex and since the frame rate of the camera is limited, they may introduce delay, which is undesirable in C2C communications. Therefore, in this work ZF is adopted to reduce the complexity compared to MMSE, ML, and MLSE, which is described in this chapter.

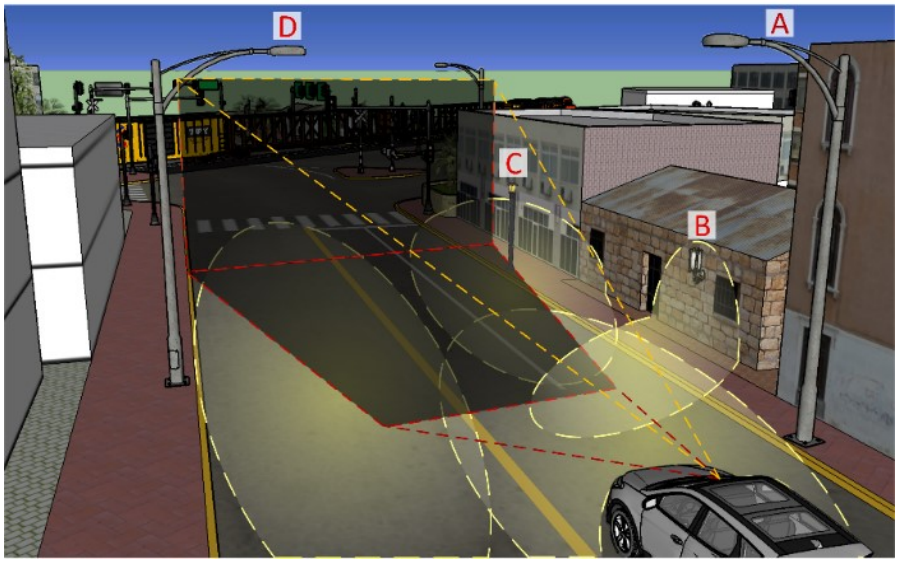

Figure 6.1: Lighthing sources in a typical urban environment showing overlapping illumination areas.

In this chapter, we propose two detection schemes of (*i*) optical simple detection and ZFE (SDZFE); and (*ii*) differential detection and ZFE (DDZFE) for NLOS MIMO-based OCC in order to mitigate the impact of crosstalk. We show that, (*i*) using these schemes an error-free transmission is possible even under a high-level of crosstalk compared to HS/EGC, see Chapter 4; (*ii*) in terms of the eye-height in the eye-diagram of the received signal, at a distance 5 m and ISO of 6400, SDZFE offers improved performance compared to HS/EGC and DDZFE by ~1.1 and 1.2 ADU/ADU, respectively at the cost of increased process time by 3; and (*iii*) for the Txs located close to each other, both DDZFE and SDZFE offer improved performance compared to HS/EGC.

The structure of the chapter is as follows: We introduce the system model used in this work with a block diagram. We then present our proposed detection algorithms of DDZFE and SDZFE. Finally, we present the evaluations of the simulation and experimental results.

6.2 System Model

The schematic system block diagram of the proposed system is illustrated in Fig. 6.2. N_{t} independent pseudo-random binary sequences $\boldsymbol{D}_{1\times N_{\mathrm{t}}} = [\mathbf{d}^{l}]_{1\times N_{\mathrm{t}}}$ of N_{pa}-bit length, where $l = 1, \ldots, N_{\mathrm{t}}$, and N_{t} is the number of Txs in the OOK-NRZ format are generated as the payload. The payload is applied to a packet generator module, where preamble and pilot bits with the lengths of N_{pr} and N_{t}, respectively are added. The generated packet streams $\mathbf{B}_{1\times N_{\mathrm{t}}} = [\mathbf{b}^{l}]_{1\times N_{\mathrm{t}}}$ are differentially encoded as $\mathbf{X}_{1\times N_{\mathrm{t}}} = [\mathbf{x}^{l}]_{1\times N_{\mathrm{t}}}$ where $x_k^l = b_k^l \oplus x_{k-1}^l$, and x_0^l is set to "0". Note that, in order to ensure interfere-free pilots, for the l-th Tx only the $2l$-th bit is assiagned "1" and remaining bits are set to "0" for the pilot signal. The output of the differential signalling block are then used for intensity modulation of the light sources for transmission over the NLOS channel. The free space channel impulse response is given by:

$$\mathbf{H}_{N_{\mathrm{r}}\times N_{\mathrm{t}}}^{\mathrm{ch}} = \left[\mathbf{H}_{N_{\mathrm{r}}\times 1}^{\mathrm{ch},l}\right]_{1\times N_{\mathrm{t}}}, \tag{6.1}$$

where

$$\mathbf{H}_{N_{\mathrm{r}}\times 1}^{\mathrm{ch},l} = \left[h^{\mathrm{ch},l}(u,v)\right]_{N_{\mathrm{r}}\times 1}, \tag{6.2}$$

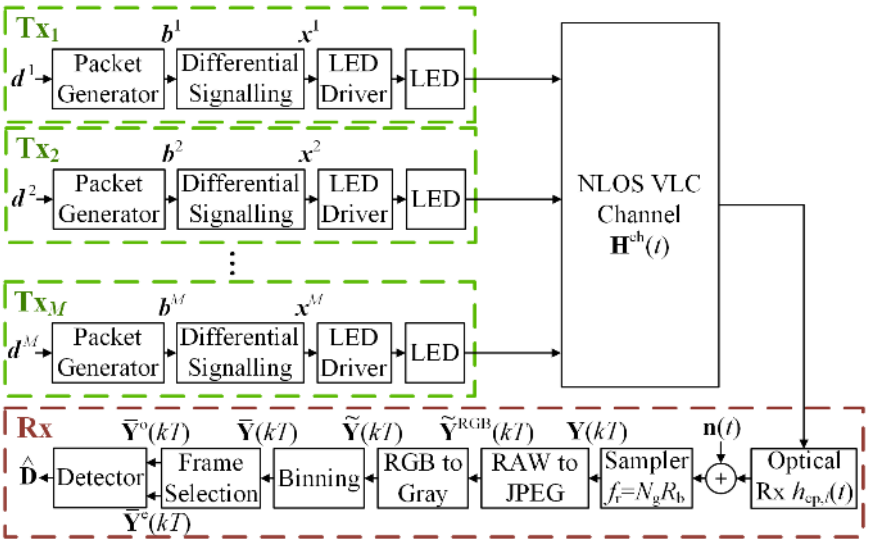

Figure 6.2: Proposed NLOS MIMO OCC system block diagram.

At the Rx, a camera is used for recording the intensity modulated light sources (i.e., capturing the changes in the light intensity) by sampling as given by [151]:

$$\mathbf{H}^{\text{cam}}_{N_\text{r}\times 1}(kT_\text{fr}) = \mathbf{G}_{N_\text{r}\times 1} \times \Big(\Gamma(kT_\text{fr}) - \Gamma\big(kT_\text{fr} - T_{\text{exp}}\big)\Big), \tag{6.3}$$

where $N_\text{r} = V \times U$, $G_{N_\text{r}} \times 1$, T_exp, $T_\text{fr} = 1/R_\text{f}$ and $\Gamma(.)$ denote the number of Rxs, gain of an array of pixels, exposure time, inter-frame time and Heaviside step function, respectively. The camera's sampling rate R_f is set to $2R_\text{b}$ in order to avoid inter-symbol interference (ISI).

The received signal is given as:

$$\mathbf{Y}_{N_\text{r}\times 1}(kT_\text{fr}) = \mathbf{H}_{N_\text{r}\times N_\text{t}}(kT_\text{fr})\mathbf{X}^\text{T}_{1\times N_\text{t}}(kT_\text{fr}) + \mathbf{N}_{N_\text{r}\times 1}(kT_\text{fr}), \tag{6.4}$$

where $\mathbf{H}_{N_\text{r}\times N_\text{t}}(kT_\text{fr}) = \big[\mathbf{H}^{l}_{1\times N_\text{r}}(kT_\text{fr})\big]^\text{T}$ and $\mathbf{N}_{N_\text{r}\times 1}(t)$ are the matrices of channel coefficients and the additive white Gaussian noise (AWGN) with the mean value μ_N and variance σ^2_N, respectively, with $l = 1, \dots, M$. $\mathbf{H}^{l}_{1\times N_\text{r}}(kT_\text{fr}) = P_\text{t}\mathbf{H}^{\text{ch},l}_{1\times N_\text{r}}.\mathbf{H}^{\text{cam}}_{1\times N_\text{r}}(kT_\text{fr})$, where P_t is the transmit power per Tx.

Note that, in this work we do not deal with the colours, therefore following the selection of odd/even frames all frames are converted to the grayscale as given by Eq. (3.5) In order to reduce the complexity of processing of the received data, we apply an $m \times n$ binning to $\widetilde{\mathbf{Y}}_{N_\mathrm{r}\times 1}(kT_\mathrm{fr})$ as given by:

$$\begin{aligned}\overline{\mathbf{Y}}_{N_\mathrm{r}\times 1}(kT_\mathrm{fr}) &= [\overline{y}_i]_{N_\mathrm{r}\times 1} \\ &= \overline{\mathbf{H}}_{N_\mathrm{r}\times N_\mathrm{t}}(kT_\mathrm{fr})\left[\mathbf{X}_{1\times N_\mathrm{t}}(kT_\mathrm{fr})\right]^T + \overline{\mathbf{N}}_{N_\mathrm{r}\times 1}(kT_\mathrm{fr}),\end{aligned} \tag{6.5}$$

where $\overline{y}_i = \frac{1}{mn}\mathbf{1}_{1\times mn}\mathbf{A}^i_{mn\times 1}$, $\mathbf{A}^i_{mn\times 1} = \left[\widetilde{y}_j\right]_{mn\times 1}$, $j = mod\left(i-1, \frac{V}{n}\right)n + o_1 + \left(\left\lfloor\frac{(i-1)n}{V}\right\rfloor m + o_2 - 1\right)V$, $o_1 = 1, \dots, n$, $o_2 = 1, \dots, m$, $\mathbf{1}_{1\times mn}$ is the matrix of ones.

Based on Lyapunov central limit theorem, when mn is a large number, b_i is a Gaussian distributed random variable with mean of $\mu_{b_i} = \frac{1}{mn}\sum_{o_1=1}^{n}\sum_{o_2=1}^{m}\mu_{\tilde{y}_j}$ and variance of $\sigma^2_{b_i} = \frac{1}{(mn)^2}\sum_{o_1=1}^{n}\sum_{o_2=1}^{m}\sigma^2_{\tilde{y}_j}$. Note that, following binning the number of pixels cannot be less than the number of Txs.

6.3 Proposed Algorithms

Two detection schemes are proposed in order to extract the *payload* from captured video streams and compare them to the HS/EGC algorithm. The operation of algorithms are best described with reference to the flowchart shown in Fig. 6.3. For the entire captured video, the proposed algorithms are first applied to odd and then to even frames of $\overline{\mathbf{Y}}^{\mathrm{o}}_{N_\mathrm{r}\times 1}$ and $\overline{\mathbf{Y}}^{e}_{N_\mathrm{r}\times 1}$, respectively. In the algorithms there are three stages of (*i*) *preamble* detection; (*ii*) *pilot* detection; and (*iii*) *payload* extraction, which are controlled by two flags, i.e., $Flag_{\mathrm{pr}}$ and $Flag_{\mathrm{pi}}$. Note that, at the start of algorithm, both flags are set to "0". In order to locate the footprint of the Tx on the floor surface

each frame is subtracted from the previous frame as given by:

$$\begin{aligned}\Delta\overline{\mathbf{Y}}^{\mathrm{o}}_{N_{\mathrm{r}}\times 1}(kT_{\mathrm{fr}}) &= \overline{\mathbf{Y}}^{\mathrm{o}}_{N_{\mathrm{r}}\times 1}(kT_{\mathrm{fr}}) - \overline{\mathbf{Y}}^{\mathrm{o}}_{N_{\mathrm{r}}\times 1}\big((k-1)T_{\mathrm{fr}}\big) \\ &= \overline{\mathbf{H}}_{N_{\mathrm{r}}\times N_{\mathrm{t}}}(kT_{\mathrm{fr}})\big[\Delta\mathbf{X}^{o}_{1\times N_{\mathrm{t}}}(kT_{\mathrm{fr}})\big]^{T} + \Delta\overline{\mathbf{N}}^{\mathrm{o}}_{N_{\mathrm{t}}\times 1}(kT_{\mathrm{fr}}),\end{aligned} \tag{6.6}$$

where $\Delta\mathbf{X}^{\mathrm{o}}_{1\times N_{\mathrm{t}}}(kT_{\mathrm{fr}}) = \mathbf{X}^{\mathrm{o}}_{1\times N_{\mathrm{t}}}(kT_{\mathrm{fr}}) - \mathbf{X}^{\mathrm{o}}_{1\times N_{\mathrm{t}}}\big((k-1)T_{\mathrm{fr}}\big)$ and $\Delta\overline{\mathbf{N}}^{\mathrm{o}}_{N_{\mathrm{r}}\times 1}(kT_{\mathrm{fr}}) = \overline{\mathbf{N}}^{\mathrm{o}}_{N_{\mathrm{r}}\times 1}(kT_{\mathrm{fr}}) - \overline{\mathbf{N}}^{\mathrm{o}}_{N_{\mathrm{r}}\times 1}\big((k-1)T_{\mathrm{fr}}\big)$ is an AWGN with zero mean and variance of $< 2\sigma^2_{\mathrm{N}}$. Note, elements of $\Delta\overline{\mathbf{Y}}^{\mathrm{o}}_{N_{\mathrm{r}}\times 1}(kT_{\mathrm{fr}})$ can have any integer values within the range of -255 to +255.

At the *preamble* detection stage, which is the same for both schemes, since Txs are synchronized and share the same *preamble*, $\Delta\mathbf{Y}^{\mathrm{o}}_{N\times 1}(kT_{\mathrm{fr}})$ is averaged as given by:

$$S_k = \left|\mathrm{mean}\left(\Delta\mathbf{Y}^{\mathrm{o}}_{N_{\mathrm{r}}\times 1}(kT_{\mathrm{fr}})\right)\right|, \tag{6.7}$$

where $|.|$ is the absolute value. This procedure is performed N_{pr} times. S_k is then applied to a *preamble* hard threshold module the output of which is compared with the *preamble*. On matching, $Flag_{\mathrm{pr}}$ is toggled to "1" and detection proceeds to the next stage.

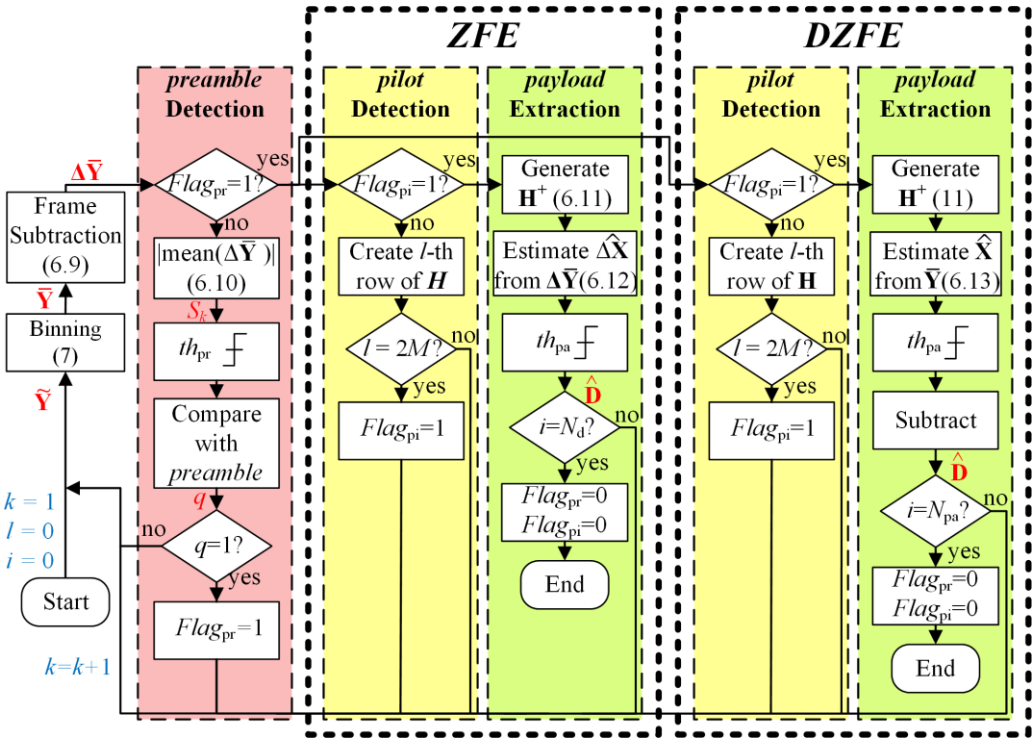

Figure 6.3: The flowchart of the proposed detection algorithms.

In the following subsections, each of the proposed detection techniques are described.

6.3.1 *Zero-Forcing Equalization (ZFE)*

Following preamble detection, $\overline{\mathbf{H}}_{N_r \times N_t}(kT_{fr})$ is generated for even values of k using pilot bits of the Txs. Since pilots are unique and only with a single bit set to "1" for each Tx, the frame related to each pilot is then used to construct each row of the DDZFE matrix of coefficient, i.e., $\overline{\mathbf{H}}_{N_r \times N_t}(kT_{fr})$, and on completion $Flag_{pi}$ is toggled to "1". Finally, in the payload extraction stage, in order to estimate the values of $\mathbf{X}^{o}_{N_t \times 1}(kT_{fr})$ both sides of (6.9) are multiplying with $\left[\overline{\mathbf{H}}_{N_r \times N_t}(kT_{fr})\right]^{-1}$ to force the interfering terms to be zero. Note that, $N_r \neq N_t$, $\overline{\mathbf{H}}_{N_r \times N_t}$ is rank deficient, therefore no inversed matrix. Instead, a pseudo inverse matrix can be used, which is given as [192]:

$$\overline{\mathbf{H}}^{+}_{N_\mathrm{t}\times N_\mathrm{r}} = \left(\overline{\mathbf{H}}^{\mathrm{H}}_{N_\mathrm{t}\times N_\mathrm{r}}\overline{\mathbf{H}}_{N_\mathrm{r}\times N_\mathrm{t}}\right)^{-1}\overline{\mathbf{H}}^{\mathrm{H}}_{N_\mathrm{t}\times N_\mathrm{r}}, \tag{6.8}$$

where $\overline{\mathbf{H}}^{\mathrm{H}}_{N_\mathrm{t}\times N_\mathrm{r}}$ is Hermitian transpose of $\overline{\mathbf{H}}_{N_\mathrm{r}\times N_\mathrm{t}}$. Accordingly, ZFE is applied to $\Delta\overline{\mathbf{Y}}^{\mathrm{o}}_{1\times N_\mathrm{r}}(kT)$, hence the transmitted signal can be estimated as:

$$\widehat{\Delta\mathbf{X}}^{\mathrm{o}}_{N_\mathrm{t}\times 1}(kT_\mathrm{fr}) = \overline{\mathbf{H}}^{+}_{N_\mathrm{t}\times N_\mathrm{r}}\left[\Delta\overline{\mathbf{Y}}^{\mathrm{o}}_{1\times N_\mathrm{r}}(kT_\mathrm{fr})\right]^{\mathrm{T}} - \overline{\mathbf{H}}^{+}_{N_\mathrm{t}\times N_\mathrm{r}}\left[\Delta\mathbf{n}^{\mathrm{o}}_{1\times N_\mathrm{r}}(kT_\mathrm{fr})\right]^{\mathrm{T}}. \tag{6.9}$$

However, this approach also leads to noise amplification (i.e., reduced SNR and higher BER).

Finally, $\widehat{\Delta\mathbf{X}}^{\mathrm{o}}_{N_\mathrm{t}\times 1}(kT_\mathrm{fr})$ is passed through a hard threshold module to estimate $\hat{d}^{l}_{k}$. Note, with the upper and lower levels of $\widehat{\Delta\mathbf{X}}^{\mathrm{o}}_{N_\mathrm{t}\times 1}(kT_\mathrm{fr})$ being "1" and "0", respectively th_pa is set to 0.5. This stage is repeated for N_pa iterations.

6.3.2 *Simple Detection Zero-Forcing Equalization (SDZFE)*

The SDZFE algorithm is very similar to DDZFE except for $\mathbf{H}^{+}_{N_\mathrm{t}\times N}$ that is applied to $\overline{\mathbf{Y}}_{N\times 1}$ as given by:

$$\widehat{\mathbf{X}}^{\mathrm{o}}_{N_\mathrm{t}\times 1}(kT_\mathrm{fr}) = \overline{\mathbf{H}}^{+}_{N_\mathrm{t}\times N_\mathrm{r}}\left[\overline{\mathbf{Y}}^{\mathrm{o}}_{1\times N_\mathrm{r}}(kT_\mathrm{fr})\right]^{\mathrm{T}} - \overline{\mathbf{H}}^{+}_{N_\mathrm{t}\times N_\mathrm{r}}\left[\overline{\mathbf{N}}^{\mathrm{o}}_{1\times N_\mathrm{r}}(kT_\mathrm{fr})\right]^{\mathrm{T}}. \tag{6.10}$$

$\widehat{\mathbf{X}}^{\mathrm{o}}_{N_\mathrm{t}\times 1}(kT_\mathrm{fr})$ is then passed through a hard threshold module and successively subtracted to estimate $\hat{d}^{l}_{k}$. In DZFE, the detection is carried out on each received frame. The advantage of using SDZFE over DDZFE would be the relaxed requirement for differential signalling, hence no enhanced noise.

6.4 Experimental Results

To evaluate the performance of the proposed system, a similar experimental test-bed to the one in Chapter 4 was used, see fig. 6.4(a) . Ten 1066-bit packets composed of the *payload*, *pilot*, and *preamble* of 1000, 2, and 64 bits long, respectively was generated in the OOK-NRZ format.

Note that, in the detection process, we used 10 binning. A camera-based Rx (i.e., IS-based Rx) offers a spatial diversity capability given that, the pixel size in the IS is in the order of ~μm, which is larger than the lights' half wavelength.

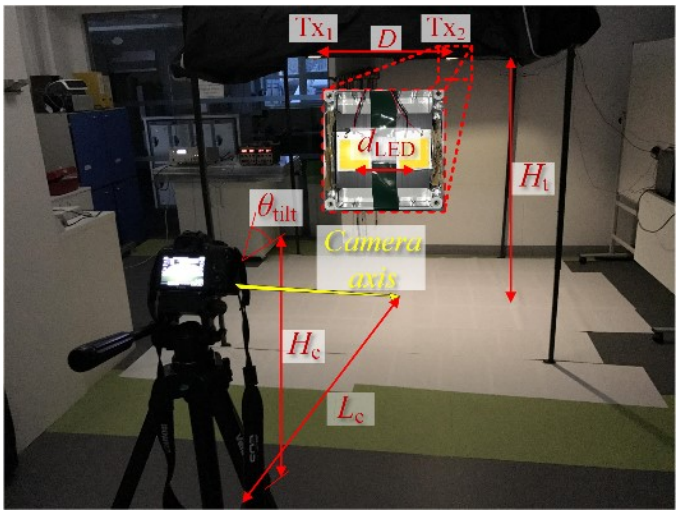

(a)

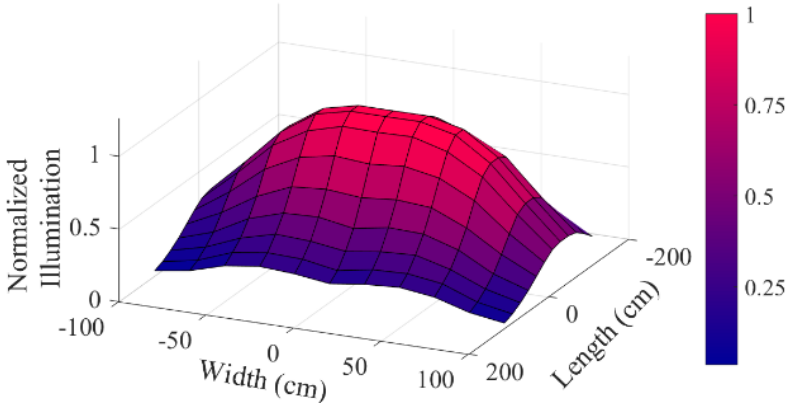

(b)

Figure 6.4: (a) The experimental testbed and (b) normalized light intensity on the floor for $D = 1$ m.

Figures 6.5 show the measured eye diagrams of the received signals for HS/EGC,

ZFE, and SDZFE before th_{pa}, where R_{b} is reduced ten times in order to have 10 samples per symbol. Note that, with high levels of interference, it is not possible to establish an error-free transmission with HS/EGC. Then it can be observed for all eye diagrams that: (*i*) the eye symmetry is maintained thus indicating very little contributions due channel distortion; (*ii*) sharp slopes indicate good tolerance to the timing jitter; (*iii*) the wide eye width for some cases (i.e., reduced interference and noise thus lower BER); (*iv*) multi-levels; and (*v*) higher SINR levels for some cases.

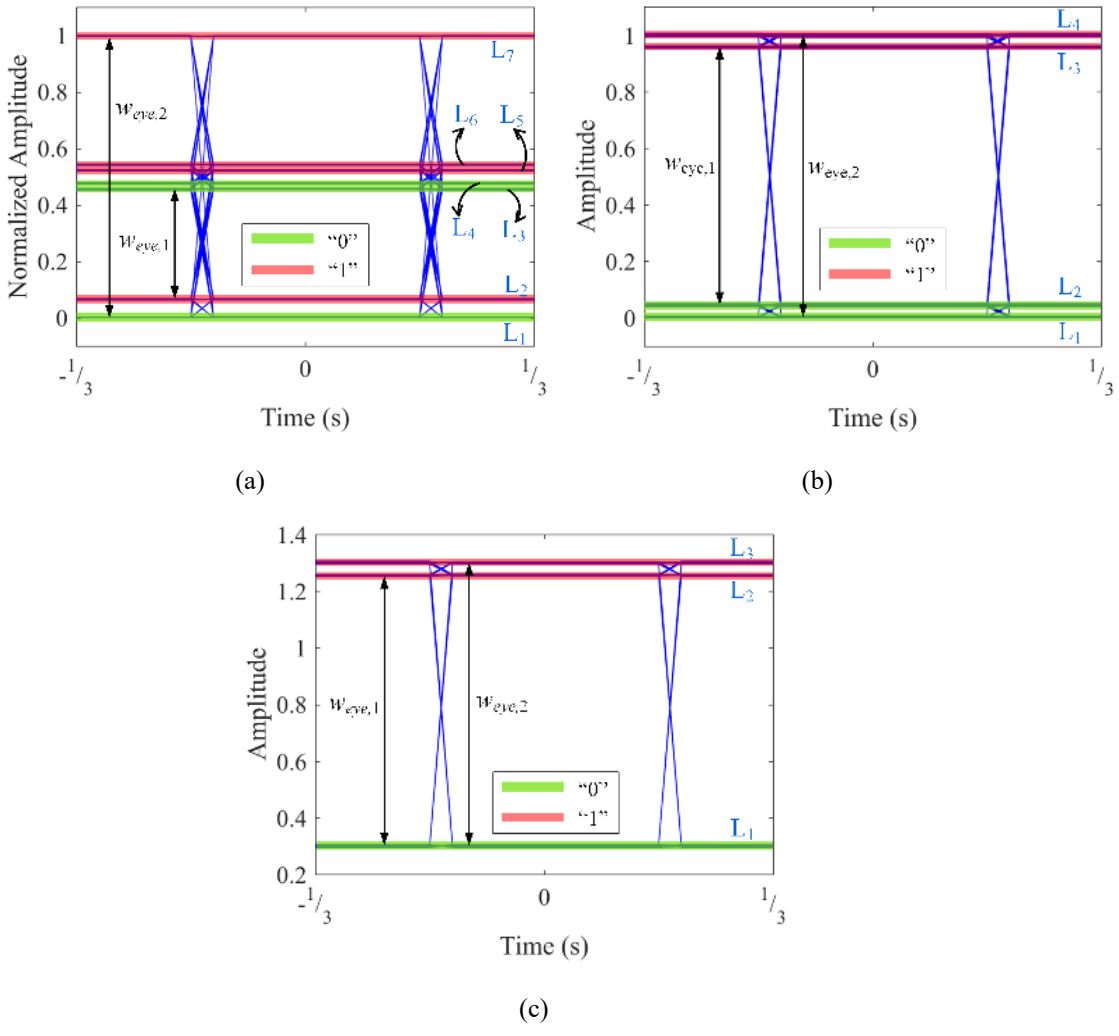

Figure 6.5: Eye diagrams of the received signal with interference and non-linear gamma correction for: (a) HS/EGC, (b) ZFE, and (c) SDZFE.

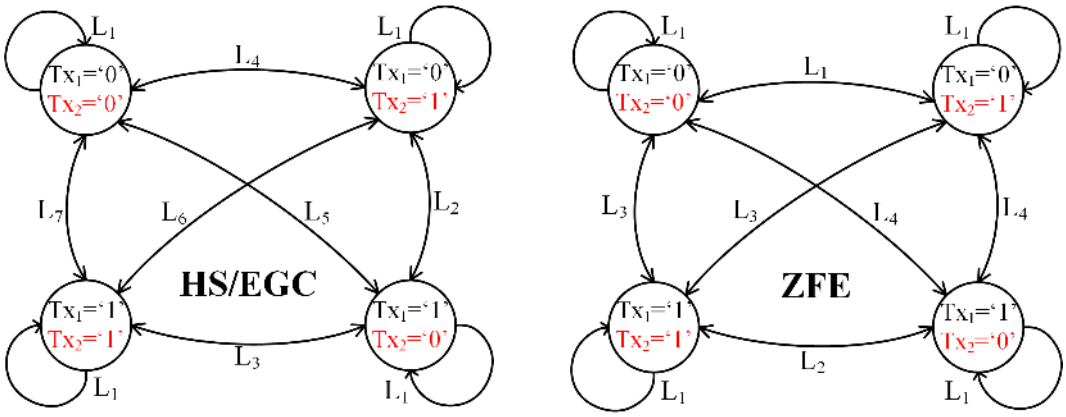

Figure 6.6: State diagrams for multi-levels eye diagrams: (a) HS/EGC, and (b) ZFE.

As shown in Figs. 6.5(a), and (b), for HS/EGC and ZFE, there are 7 and 4 levels, i.e., L_1 to L_7, respectively, which are best explained with reference to state diagrams depicted in Fig. 6.6. Additionally, for SDZFE scheme, 3-level shown is based on the states of desired and interfering Txs as outlined in Table 6.1. The multi-levels observed in the eye-diagrams for DDZFE and SDZFE are mainly due to non-linear gamma correction curve, while for HS/EGC it is due to both gamma correction and interference. In the presence of gamma correction, the intensity of light in the overlapping area is not the summation of the footprints; hence following ZFE, new levels are evident in the eye diagrams.

Table 6.1. State of Txs for Each Level of The Eye-Diagram for SDZFE.

DZFE	**Desired Tx**	**Interfering**
L1	"0"	"0"
L1	"0"	"1"
L3	"1"	"0"
L2	"1"	"1"

Figure 6.7(a) shows the simulated normalized eye-height (i.e., normalized to the widest eye opening $\frac{w_{\text{eye},1}}{w_{\text{eye},2}}$ as a function of D/H for HS/EGC, DDZFE and SDZFE and for two Txs with the viewing angles of 60^{o}. Notice that, the DDZFE and the SDZFE has an almost flat response over all D/H up to 2 m/m, which outperforms the HS/EGC. The negative value of the normalized eye opening for HS/EGC shows that L2 is less than L3, hence data cannot be recovered. Figure 6.7(b) depicts the normalized eye-height against the normalized ambient light illumination level γ (i.e., normalized to the peak illumination level of the Tx_1) for the proposed algorithms, P_{t} of 20 dBm, and for $D/H = 0.5$ m/m. Here as well, HS/EGC displays the worse normalised eye-height of < -0.3 compared with the average normalized heights of 0.8 and 0.9 for DDZFE and SDZFE, respectively, over $0.5 < \gamma < 4$. Note that, as expected HS/EGC displays an almost flat response. Note, for SDZFE and DDZFE, the increase in the eye width beyond $\gamma = 0.5$ is due to the increase in the intensity of low-level pixels, hence the entire image is shifted to the more linear region of gamma correction curve.

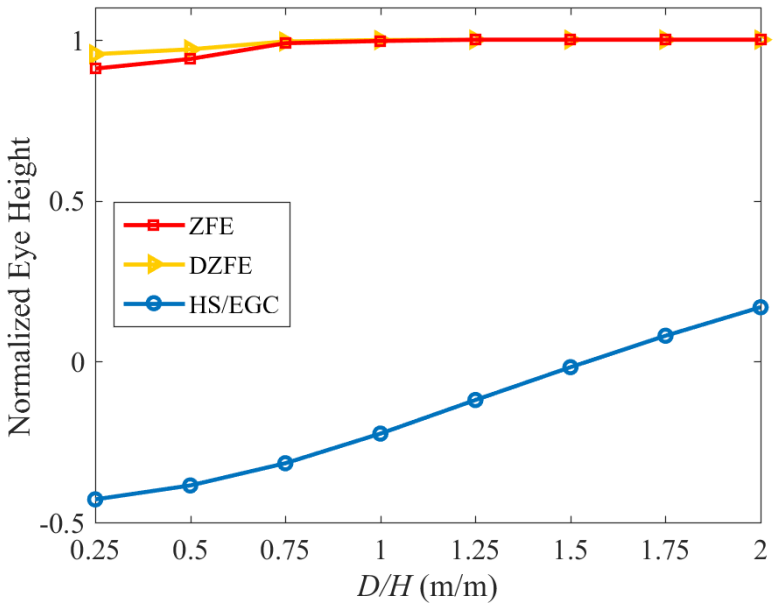

(a)

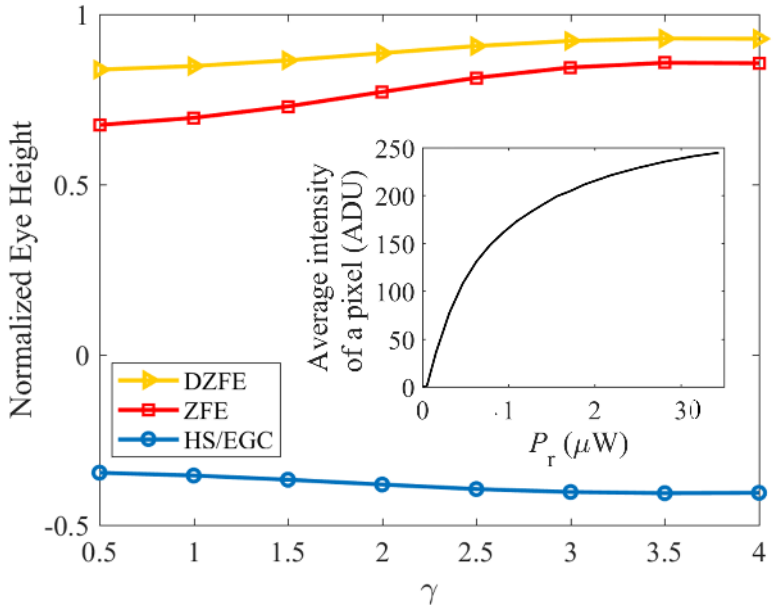

(b)

Figure 6.7: The normalized eye height as a function of: (a) D in the absence of ambient light; and (b) γ at $D/H = 0.5$ m/m for the proposed algorithms, P_t of 20 dBm, $L = 5$ m, and a Tx's viewing angle of 60^{o}. The inset is the average intensity of a pixel as a function of total received power at the camera for ISO of 3200, T_{exp} of 0.004 s, focal length of 55 mm, and aperture f-stop of f/5.6.

Figure 6.8(a) depicts the measured BER performance as a function of the transmit power for the proposed algorithms and for the ISO levels of 3200 and 6400, $T_{exp} = 0.01$ s, $L_s = 5$ m, and f-stop of $f/4$ with only a single Tx in the absence of ambient light. The results show almost the same BER performance for HS/EGC and DDZFE schemes with a marginal power penalty of 0.1 dB irrespective of the ISO. Note, for ISO of 6400, a 3 dB lower transmit power level is required compared to the ISO of 3200 for all schemes at BER lower than the forward error correction (FEC) limit of 3.8×10^{-3}. In addition, there is a ~1 dB of power penalty between SDZFE and HS/EGC irrespective of the ISO levels. Finally, Fig. 6.8(b) demonstrates the BER plots as a function of the transmit power for the three schemes and for link spans of 5 m and 10 m, ISO of 6400, T_{exp} of 0.01 s, and f-stop of $f/4$ displaying a similar profile as in

Fig. 6.8(a). Note, for a link span of 5 m the transmit power level is ~3 dB lower than the link span of 10 m at the BER below the FEC limit of 3.8×10^{-3} for all schemes.

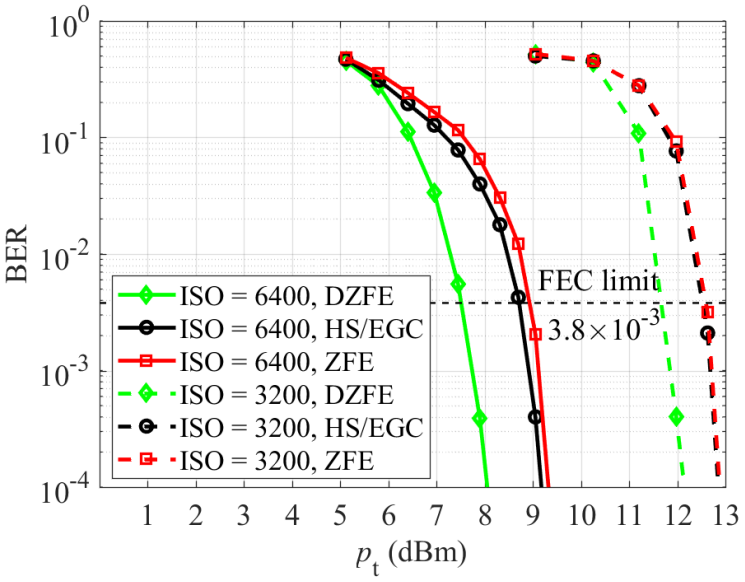

(a)

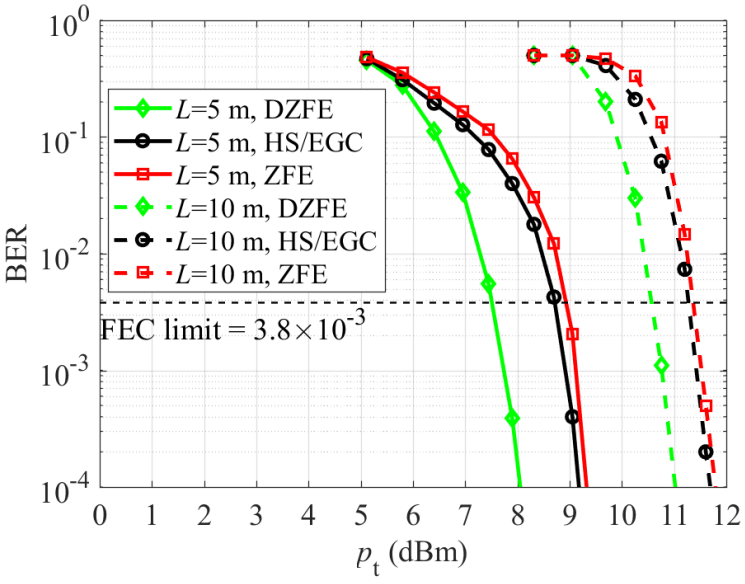

(b)

Figure 6.8: BER as a function of transmit power for Texp of 1/100 s, aperture f-stop of f/4 for: (a) different ISO levels, and (b) different link spans.

6.5 Link Budget

The link budget analysis for a link span of 60 m, which is a typical distance detecting an object from the reflected light in urban areas [193], is outlined in Table 6.2 showing the required power values for two cases where (*i*) no ambient light is considered such as highways at night and (*ii*) other lights in the street provide ambient light such as urban areas and shopping streets. As discussed in Chapter 2, the CE0 class dictates an average illuminance of 50 Lux, which is equivalent to 32.65 dB for a lamp at a height of 2 m, which is the average transmit power, i.e., in OOK-NRZ signalling the peak intensity is 35.65 dB (i.e., the peak is double the average value). Note, since the requirement is set on illuminance on the surface of the road, the height of the lamp only defines the area of the footprint. This means if the height is increased, the mean illuminance on the road surface is fixed, but the area of the footprint increases.

Here, we consider a 10 m lamp post, which compared to 2 m height of the Tx in the experiments gives a gain of 14 dB. Note, this analysis is based on the results for a $T_{\text{exp}} = 0.01$ s, ISO of 6400, aperture stop of $f/4$, and $f = 18$ mm. The results show link margins of 13 and 14 dB for HS/EGC and SDZFE algorithms in the absence of ambient light, respectively, and 23 and 24 dB for HS/EGC and SDZFE in the presence of ambient light, respectively. Therefore, this link margin allows a less exposure time for high frame rate cameras, or less aperture area for smaller cameras, e.g., a camera with a half aperture size and double the frame rate leaves a link margin of ~7 dB for HS/EGC in the absence of ambient light. Note that, a 100 m link span for a vehicle speed of 70 mph in the highways is equivalent to >3 s of link duration. Therefore, for a camera with 120 fps, this translates to 180 bits, i.e., a packet can contain ~100 bits to be in the safe side. In addition, for a speed of 30 mph in the urban area provided that a clear link span up to 100 m is available,

a link duration of ~7.5 s and hence 450 bits can be expected. Note, this link margin can also consider the blockage of the footprint due to obstacles or footprints being partially in the FoV of the camera.

Table 6.2. Link budget for different ambient light conditions and detection methods in OCC.

Background illumination	**No Ambient light**		**Ambient Light**	
Detection Method	**HS/EGC**	**DZFE**	**HS/EGC**	**DZFE**
Required P_t for $L_s = 10$ m (dBm)	11.5	10.5	1.5	0.5
Loss due to increase in the height from 2 m to 10 m (dB)	-14			
Geometrical loss at 100 m compared to 10 m (dB)	20			
Ratio of road surface to white paper reflection coefficient (dB)	5.2			
Total loss (dB)	11.2			
Required P_t for $L_s = 100$ m and road surface (dBm)	22.7	21.7	12.7	12.7
Available transmit intensity based on CE0 (dBm)	35.65			
Link margin (dB)	12.95	13.95	22.95	23.95

6.6 Summary

In this chapter, we proposed two algorithms based on DDZFE for NLOS MIMO OCC systems, in order to extract the payload in the presence of gamma correction, noise, and interference. We showed that, the proposed algorithms tolerate higher levels of interference compared to the HS/EGC scheme. For the OOK-NRZ signalling format, we showed that the eye diagrams displayed multiple-levels due to gamma correction and interference. We also showed that for higher transmit power level of 20 dBm, ZFE-based algorithms outperformed HS/EGC because of high tolerance to the ambient light and ratio of spacing to height of Txs (i.e., 0.25 m/m). However, for lower transmit power levels (i.e., 6 dBm $<$ P_{t} $<$ 13 dBm), HS/EGC offered almost the same BER performance as DDZFE below the FEC limit. Moreover, HS/EGC shows ~1.1 dB worse performance compared to SDZFE due to increased level of noise as a result of frame subtraction. Although DDZFE showed ~1.2 dB power penalty compared to SDZFE, th_{pa} in this scheme is fixed to 0.5. Compared to HS/EGC, which is limited to few scenarios, the proposed DDZFE and SDZFE algorithms offered higher tolerance to the spacing between Txs, but at the cost of increased computation time (i.e., by three times for 10 binning) for obtaining the inverse channel matrix. Finally, we showed that a link margin of ~13 dBm can be expected for HS/EGC for a street light with a height of 10 m, and a link span of 100 m, which enables the system to use higher frame rate cameras, or operate with some blocking or shadowing.

Chapter 7 CONCLUSIONS AND FUTURE WORK

7.1 Conclusions

This thesis highlighted the technical challenges, motivations behind conducting this study and the contributions made to knowledge in Chapter 1. An overview on the fundamentals of VLC in ITS including Tx, channel and Rx were given in Chapter Two. Typical modulation schemes used in VLC, features and requirements on the head/taillights and streetlights as well as reflection characteristics of road surfaces under different conditions were discussed. Chapter three provided an overview on OCC highlighting typical modulation schemes for OCC to avoid flickering problem due to low frame rate of the camera. A channel model for LOS OCC links as well as a review on the NLOS based were also presented. The chapter also illustrated a typical camera structure, discussing the role of lens system and a typical structure of CCD and CMOS image sensors. Moreover, the concept of rolling shutter and global shutter as well as the major noise sources were highlighted.

Chapter 4 presented an end-to-end NLOS $2 \times N_{\mathrm{r}}$ OCC system. For the first time, a

comprehensive theoretical model of the channel impulse response for NLOS OCC under clear weather conditions was developed. The image sensor of the camera is composed of a massive number photodetectors, which offers diversity capability that can be exploited to improve the link performance. Two hybrid combining techniques of HS/EGC and HS/MRC were investigated in terms of BER against the transmit power for different camera parameters.

In addition, in camera based optical Rxs with massive imaging capability, where light beams are mapped on a specific area of the image sensor, the illuminated sections (i.e., PDs) can be selected using SC. This chapter presented a SC technique known as mask matching, block matching, or region of interest in order to select the pixels with higher received intensity. A unique non-standard packet structure composed of *preamble*, *pilot*, and *payload* and a novel detection technique based on the packet structure were introduced. A comprehensive experimental test-bed was developed for measurements and evaluation of the proposed scheme. It was shown that, for an ISO of 6400, T_{exp} of 0.01 s, aperture f-number of $f/4$, the Tx being 1.8 m above the floor surface, in the absence of ambient light, and the camera being 5 m away from the Tx, by employing an RB only a transmit power of ~16 dBm was needed to achieve the 7% FEC BER limit of 3.8×10^{-3}. We showed that, both HS/MRC and HS/EGC-based systems offered almost the same performance because the intensity of the pixels in the region of interest did not vary significantly. It was also shown that, with doubling ISO, exposure time, and aperture area, the required transmit power to achieve the 7% FEC BER limit improved by ~3 dB. However, no improvement was expected by increasing the ISO as it does not improve the SNR of the system. The mismatch between the figures is because, in the JPEG format, low intensities below a certain value defined by the camera are clipped to zero. Therefore, by applying an amplification before

ADC, the signal moved away from the clipping point, hence improved power gain. Moreover, we showed that, the information could not be fully extracted when the overlapping area of two Txs exceeds ~50%. The overlap above 50% resulted in a part the signal related to level “1” fall below another part of the signal related to level “0”.

In the urban areas where the number of light sources in a small area is more, such as intersections, crossroads, or streets with opposite or staggered streetlight arrangements, the level of overlapping footprint of the Tx increases, hence enhanced interference. Therefore, the condition on the limited overlap may not apply. In Chapter Five, a SDM-TDM technique was proposed to reduce the overlapping area of the footprints. A dedicated packet structure was given for this system. The experiments in this chapter was carried out for different link spans, ambient light levels, focal points, and focusing modes. The results showed that, in the experimental setup, at a distance of 10 m and in the absence of ambient light, a transmit power of ~16 dBm per Tx was required, which showed a power penalty of ~3 dB compared to a link span of 5 m. This is because in low intensity levels, the camera in JPEG format clipped the signal. Therefore, when the camera was further away from the source, since the image of the Tx’s footprint shrinks, the received light was concentrated over a reduced number of pixels, hence less clipping. Moreover, by introducing ambient light to the system, the required power to achieve the BER of 3.8×10^{-3} improved by ~10 dB, since ambient light shifts the received signal away from the clipping point. In addition, the chapter highlighted that the focal point and focusing distance of the camera did not have a significant impact on the performance of the system, if the entire footprint of the Txs after changing the focal point is inside the FoV of the camera. The reason is that, by increasing the focal length at a fixed f-number the aperture area increases with the same speed, hence no improvement in the required transmit power. Therefore, the

camera can have a wide FoV and a wide aperture area.

Although TDM could solve the problem of increased overlapping footprints, in very dense urban areas such as shopping streets where the number of streetlights, screens, shopping lights, etc. exceeds tens in a small area, this technique may severely decrease the data rate. Chapter 6, for the first time, adopted ZF in the context of OCC. Two algorithms based on ZF was proposed which were capable of extracting the data under very high level of interference. It was shown that, when the ratio of the spacing between Txs was double the height of the Txs, the normalized height of the eye diagram for DDZFE and SDZFE algorithms was ~0.7 more compared to HS/EGC. Moreover, if the spacing was less than 1.5 times the height of the Txs, HS/EGC was not capable of recovering the data. This means, the spacing between two neighbouring lampposts with a height of 5 m must be at least 7.5 m to be able to use HS/EGC. In addition, if the illumination level of the ambient light on the road surface is equal to the peak intensity of the Txs, it was shown that, when the spacing between the Txs was four times more than the height of the Txs, the height of eye diagram for ZDF, SDZFE, and HS/EGC is ~0.8, ~0.9, and -0.4, respectively. This signifies that the ZF-based algorithms showed a high tolerance under high level of interference as well as ambient light. Although ZF increases the level of the noise in the Rx, in this chapter it was shown that, at the 7% FEC limit, the impact of noise enhancement was insignificant. However, SDZFE achieved a gain ~1 dB compared to HS/EGC at a cost of triple processing time. The thesis stated that, a link margin of ~13 dB can be expected for a link span of 100 m and a street light height of 10 m. This indicates that the link duration in a highway with 70 mph speed can be >3 s, which yields to a packet size of 100 bits for a frame rate of 120 fps.

In conclusion, this thesis investigated a solution to link outage in OCC due to

shadowing or the absence of LOS link by extracting the information from the off-axis reflection of the Txs. Different detection schemes were proposed for different scenarios based on the level of interference and experimentally evaluated as a feasible option. The proposed schemes were shown to be capable of extracting information under low levels of illumination.

7.2 Future work

Even though the objectives stated in Chapter one have been accomplished, the following future work is recommended in order to extend the work reported in this thesis.

1. **Flicker-free modulation formats:** In this work, OOK-NRZ was adopted as a modulation technique, which in very low data rates can cause flickering. There are a number of techniques reported in the literature that can avoid flickering. However, in RS-based OCC modulation schemes such as UPSOOK may be seen as dark and bright ribbons in large footprints. To solve this problem differential signalling can be adopted in which after frame subtraction only dark or bright regions will remain, provided that the Tx and camera are synchronised in frequency.
2. **Higher order modulation formats:** Since in the C2C communications, vehicles drive at a relatively high speed, it is necessary that the packets are short and receive at a high data rate before the scene is changed significantly. Therefore, since the data rate is fixed higher orders of mPAM can reduce the packet size. This ensures that the packets receive with less probability of error.

3. **Different level for preamble:** In this work, we considered 64 bits for preamble in order to avoid the repetition of preamble in the payload. However, this length for a C2C communication is long. Another option to avoid repetition is to use a different level of the signal as preamble. This level is suggested to be the highest level of the packet since preamble is the most important part of the packet and needs to be detected with less probability of error.

4. **Impact of fog on the performance of the system:** As mentioned in Chapter two, we did not consider the impact of fog on the performance of the system since the dominant condition of the weather is clear weather. However, it will be interesting to investigate that under what level of fog, illumination intensity, and link span, an NLOS communication link can be realized.

5. **Tracking the footprint:** Since the relative speed of the vehicles is high, the channel coefficients attained at the beginning of the packet might be outdated for the last few bits of the packet. This problem is especially important when the length of the packet is high compared to the frame rate of the camera. Hence, a need to track the footprint of the Txs and update the channel coefficients throughout the packet reception time. This can be estimated and implemented using image processing techniques.

References

[1] Z. Ghassemlooy, L. N. Alves, S. Zvanovec, and M.-A. Khalighi, *Visible Light Communications: Theory and Applications*: CRC Press, 2017.

[2] A. Burton, H. Minh, Z. Ghassemlooy, E. Bentley, and C. Botella, "Experimental demonstration of 50-Mb/s visible light communications using 4× 4 MIMO," *IEEE Photonics Technology Letters,* vol. 26, pp. 945-948, 2014.

[3] S. Hranilovic and F. R. Kschischang, "Short-range wireless optical communication using pixilated transmitters and imaging receivers," in *Communications, 2004 IEEE International Conference on*, 2004, pp. 891-895.

[4] P. Luo, M. Zhang, Z. Ghassemlooy, H. Le Minh, H.-M. Tsai, X. Tang*, et al.*, "Experimental demonstration of RGB LED-based optical camera communications," *IEEE Photonics Journal,* vol. 7, pp. 1-12, 2015.

[5] P. H. Pathak, X. Feng, P. Hu, and P. Mohapatra, "Visible light communication, networking, and sensing: A survey, potential and challenges," *ieee communications surveys & tutorials,* vol. 17, pp. 2047-2077, 2015.

[6] I. Takai, S. Ito, K. Yasutomi, K. Kagawa, M. Andoh, and S. Kawahito, "LED and CMOS image sensor based optical wireless communication system for automotive applications," *IEEE Photonics Journal,* vol. 5, pp. 6801418-6801418, 2013.

[7] M. Peden, R. Scurfield, D. Sleet, D. Mohan, A. A. Hyder, E. Jarawan*, et al.*, "World report on road traffic injury prevention," ed: World Health Organization Geneva, 2004.

[8] T.-C. Bui and S. Kiravittaya, "Demonstration of using camera communication based infrared LED for uplink in indoor visible light communication," in *Communications and Electronics (ICCE), 2016 IEEE Sixth International Conference on*, 2016, pp. 71-76.

[9] T. Yamazato, I. Takai, H. Okada, T. Fujii, T. Yendo, S. Arai*, et al.*, "Image-sensor-based visible light communication for automotive

applications," *IEEE Communications Magazine,* vol. 52, pp. 88-97, 2014.

[10] H. Worley. (2018). *Road traffic injuries*. Available: https://www.who.int/news-room/fact-sheets/detail/road-traffic-injuries

[11] N. E. Boudette. (2017). *Building a Road Map for the Self-Driving Car*. Available: https://www.nytimes.com/2017/03/02/automobiles/wheels/self-driving-cars-gps-maps.html

[12] O. K. Tonguz, "How Vehicle-to-Vehicle Communication Could Replace Traffic Lights and Shorten Commutes," ed: IEEE Spectrum, 2018.

[13] S. Khandelwal, A. Abhale, and U. Nagaraj, "Accident prevention and air pollution control using vanet under cloud environment," in *Proceedings of 3 rd International Conference on Recent Trends in Engineering & Technology (ICRTET'2014)*, 2014, pp. 900-904.

[14] T. Liu, A. A. Abouzeid, and A. A. Julius, "Traffic flow control in vehicular communication networks," in *American Control Conference (ACC), 2017*, 2017, pp. 5513-5518.

[15] X. Wu, S. Subramanian, R. Guha, R. G. White, J. Li, K. W. Lu*, et al.*, "Vehicular communications using DSRC: challenges, enhancements, and evolution," *IEEE Journal on Selected Areas in Communications,* vol. 31, pp. 399-408, 2013.

[16] H. Hartenstein and L. Laberteaux, "A tutorial survey on vehicular ad hoc networks," *IEEE Communications magazine,* vol. 46, pp. 164-171, 2008.

[17] M. L. Sichitiu and M. Kihl, "Inter-vehicle communication systems: a survey," *IEEE Communications Surveys & Tutorials,* vol. 10, 2008.

[18] S. K. Bhoi and P. M. Khilar, "Vehicular communication: a survey," *IET Networks,* vol. 3, pp. 204-217, 2013.

[19] (2017). *Dedicated ShortRange Communications in Intelligent Transport Systems (Technical Specification)*. Available: https://www.imda.gov.sg/-/media/imda/files/regulation-licensing-and-consultations/ict-standards/telecommunication-standards/radio-comms/imda-ts-dsrc.pdf?la=en

[20] A. Bazzi, B. M. Masini, A. Zanella, and A. Calisti, "Visible light communications in vehicular networks for cellular offloading," in *Communication Workshop (ICCW), 2015 IEEE International Conference on*, 2015, pp. 1416-1421.

[21] F. C. Commission, "FCC-15-50A1 (Allocation Report and Order)," ed, 2015.

[22] E. C. C. (ECC), "Compatibility Studies In The Band 5855– 5925 MHz Between Intelligent Transport Systems (ITS) and Other Systems," ed: European Conference of Postal and Telecommunications Administrations (CEPT), 2016.

[23] C. J. Hill and J. K. Garrett, "AASHTO connected vehicle infrastructure deployment analysis," *Federal Highway Administration, USDOT, Washington, DC,* 2011.

[24] O. K. Tonguz, N. Wisitpongphan, J. S. Parikh, F. Bai, P. Mudalige, and V. K. Sadekar, "On the broadcast storm problem in ad hoc wireless networks," in *Broadband Communications, Networks and Systems, 2006. BROADNETS 2006. 3rd International Conference on*, 2006, pp. 1-11.

[25] J. C. Lin, "Safety standards for human exposure to radio frequency radiation and their biological rationale," *IEEE Microwave Magazine,* vol. 4, pp. 22-26, 2003.

[26] V. Jungnickel, M. Uysal, N. Serafimovski, T. Baykas, D. O'Brien, E. Ciaramella*, et al.*, "A European view on the next generation optical wireless communication standard," in *Standards for Communications and Networking (CSCN), 2015 IEEE Conference on*, 2015, pp. 106-111.

[27] C. Danakis, M. Afgani, G. Povey, I. Underwood, and H. Haas, "Using a CMOS camera sensor for visible light communication," in *Globecom Workshops (GC Wkshps), 2012 IEEE*, 2012, pp. 1244-1248.

[28] E. Xie, X. He, M. S. Islim, A. Purwita, J. J. D. McKendry, E. Gu*, et al.*, "High-speed visible light communication based on a III-nitride series-biased micro-LED array," *Journal of Lightwave Technology,* 2018.

[29] S.-J. Kim, J.-W. Lee, D.-H. Kwon, and S.-K. Han, "Gamma Function Based Signal Compensation for Transmission Distance Tolerant Multilevel Modulation in Optical Camera Communication," *IEEE Photonics Journal,* vol. 10, pp. 1-7, 2018.

[30] Y. Goto, I. Takai, T. Yamazato, H. Okada, T. Fujii, S. Kawahito*, et al.*, "A new automotive VLC system using optical communication image sensor," *IEEE Photonics Journal,* vol. 8, pp. 1-17, 2016.

[31] M. Uysal, Z. Ghassemlooy, A. Bekkali, A. Kadri, and H. Menouar, "Visible light communication for vehicular networking: performance

study of a V2V system using a measured headlamp beam pattern model," *IEEE Vehicular Technology Magazine,* vol. 10, pp. 45-53, 2015.

[32] J. Perez-Ramirez and D. K. Borah, "A single-input multiple-output optical system for mobile communication: Modeling and validation," *IEEE photonics technology letters,* vol. 26, pp. 368-371, 2014.

[33] S. Itoh, I. Takai, M. S. Z. Sarker, M. Hamai, K. Yasutomi, M. Andoh, *et al.*, "A CMOS image sensor for 10Mb/s 70m-range LED-based spatial optical communication," in *Solid-State Circuits Conference Digest of Technical Papers (ISSCC), 2010 IEEE International*, 2010, pp. 402-403.

[34] S.-H. Yang, H.-S. Kim, Y.-H. Son, and S.-K. Han, "Reduction of optical interference by wavelength filtering in RGB-LED based indoor VLC system," in *Opto-Electronics and Communications Conference (OECC), 2011 16th*, 2011, pp. 551-552.

[35] R. Boubezari, H. Le Minh, Z. Ghassemlooy, and A. Bouridane, "Smartphone camera based visible light communication," *Journal of Lightwave Technology,* vol. 34, pp. 4121-4127, 2016.

[36] R. Boubezari, H. Le Minh, Z. Ghassemlooy, and A. Bouridane, "Novel detection technique for smartphone to smartphone visible light communications," in *Communication Systems, Networks and Digital Signal Processing (CSNDSP), 2016 10th International Symposium on*, 2016, pp. 1-5.

[37] S. Pergoloni, M. Biagi, S. Colonnese, R. Cusani, and G. Scarano, "A space-time RLS algorithm for adaptive equalization: The camera communication case," *Journal of Lightwave Technology,* vol. 35, pp. 1811-1820, 2017.

[38] Apple. (2018). *About Face ID advanced technology*. Available: https://support.apple.com/en-gb/HT208108

[39] W. Xiong and J. C.-M. Lee, "Efficient scene change detection and camera motion annotation for video classification," *Computer vision and image understanding,* vol. 71, pp. 166-181, 1998.

[40] Apple. (2018, September). *Augmented Reality for iOS*. Available: https://www.apple.com/uk/ios/augmented-reality/

[41] B. Lin, Z. Ghassemlooy, C. Lin, X. Tang, Y. Li, and S. Zhang, "An indoor visible light positioning system based on optical camera communications," *IEEE Photonics Technology Letters,* vol. 29, pp. 579-582, 2017.

[42] Mercedes-Benz. *Let there be light: the LED headlamps of the new E-Class.* Available: https://www.mercedes-benz.com/en/mercedes-benz/innovation/let-there-be-light-the-led-headlamps-of-the-future-e-class/

[43] P. Ji, H.-M. Tsai, C. Wang, and F. Liu, "Vehicular visible light communications with LED taillight and rolling shutter camera," in *Vehicular Technology Conference (VTC Spring), 2014 IEEE 79th*, 2014, pp. 1-6.

[44] I. Takai, T. Harada, M. Andoh, K. Yasutomi, K. Kagawa, and S. Kawahito, "Optical vehicle-to-vehicle communication system using LED transmitter and camera receiver," *IEEE photonics journal,* vol. 6, pp. 1-14, 2014.

[45] T. Nguyen, A. Islam, and Y. M. Jang, "Region-of-interest signaling vehicular system using optical camera communications," *IEEE Photonics Journal,* vol. 9, pp. 1-20, 2017.

[46] H. Chinthaka, N. Premachandra, T. Yendo, T. Yamasato, T. Fujii, M. Tanimoto*, et al.*, "Detection of LED traffic light by image processing for visible light communication system," in *Intelligent Vehicles Symposium, 2009 IEEE*, 2009, pp. 179-184.

[47] N. Rajagopal, P. Lazik, and A. Rowe, "Hybrid visible light communication for cameras and low-power embedded devices," in *Proceedings of the 1st ACM MobiCom workshop on Visible light communication systems*, 2014, pp. 33-38.

[48] Y. Kawai, T. Yamazato, H. Okada, T. Fujii, T. Yendo, S. Arai*, et al.*, "Tracking of LED headlights considering NLOS for an image sensor based V2I-VLC," in *International Conference and Exhibition on Visible Light Communications*, 2015.

[49] T. Nagura, T. Yamazato, M. Katayama, T. Yendo, T. Fujii, and H. Okada, "Tracking an LED array transmitter for visible light communications in the driving situation," in *Wireless Communication Systems (ISWCS), 2010 7th International Symposium on*, 2010, pp. 765-769.

[50] S. Arai, Y. Shiraki, T. Yamazato, H. Okada, T. Fujii, and T. Yendo, "Multiple LED arrays acquisition for image-sensor-based I2V-VLC using block matching," in *Consumer Communications and Networking Conference (CCNC), 2014 IEEE 11th*, 2014, pp. 605-610.

[51] Sony. *Sony xperia xz premium*. Available: https://www.sonymobile.com/gb/products/phones/xperia-xz-premium/specifications

[52] Phantom. *Phantom v2512*. Available: http://www.phantomhighspeed.com/Products/Ultrahigh-Speed-Cameras/v2512

[53] C.-W. Chow, C.-Y. Chen, and S.-H. Chen, "Visible light communication using mobile-phone camera with data rate higher than frame rate," *Optics express,* vol. 23, pp. 26080-26085, 2015.

[54] V. P. Rachim and W.-Y. Chung, "Multilevel Intensity-Modulation for Rolling Shutter-Based Optical Camera Communication," *IEEE Photonics Technology Letters,* vol. 30, pp. 903-906, 2018.

[55] W.-C. Wang, C.-W. Chow, L.-Y. Wei, Y. Liu, and C.-H. Yeh, "Long distance non-line-of-sight (NLOS) visible light signal detection based on rolling-shutter-patterning of mobile-phone camera," *Optics express,* vol. 25, pp. 10103-10108, 2017.

[56] R. D. Roberts, "Undersampled frequency shift ON-OFF keying (UFSOOK) for camera communications (CamCom)," in *Wireless and Optical Communication Conference (WOCC), 2013 22nd*, 2013, pp. 645-648.

[57] P. Luo, Z. Ghassemlooy, H. Le Minh, X. Tang, and H.-M. Tsai, "Undersampled phase shift ON-OFF keying for camera communication," in *Wireless Communications and Signal Processing (WCSP), 2014 Sixth International Conference on*, 2014, pp. 1-6.

[58] S.-H. Chen and C.-W. Chow, "Color-shift keying and code-division multiple-access transmission for RGB-LED visible light communications using mobile phone camera," *IEEE Photonics Journal,* vol. 6, pp. 1-6, 2014.

[59] (2019). *Homer*. Available: https://en.wikipedia.org/wiki/Homer

[60] A. G. Bell, "Alexander Graham Bell," 2004.

[61] H. Haas, "High-speed wireless networking using visible light," *SPIE Newsroom,* vol. 1, pp. 1-3, 2013.

[62] R. X. Ferreira, E. Xie, J. J. McKendry, S. Rajbhandari, H. Chun, G. Faulkner*, et al.*, "High bandwidth GaN-based micro-LEDs for multi-Gb/s visible light communications," *IEEE Photonics Technology Letters,* vol. 28, pp. 2023-2026, 2016.

[63] A. K. Rishinaramangalam, A. Rashidi, S. M. U. Masabih, A. A. Aragon, M. Monavarian, C. Lee*, et al.*, "Nonpolar GaN-Based Superluminescent Diode with 2.5 GHz Modulation Bandwidth," in *2018 IEEE International Semiconductor Laser Conference (ISLC)*, 2018, pp. 1-2.

[64] H. Le Minh, D. O'Brien, G. Faulkner, L. Zeng, K. Lee, D. Jung, *et al.*, "80 Mbit/s visible light communications using pre-equalized white LED," in *Optical Communication, 2008. ECOC 2008. 34th European Conference on*, 2008, pp. 1-2.

[65] N. Chi, M. Zhang, Y. Zhou, and J. Zhao, "3.375-Gb/s RGB-LED based WDM visible light communication system employing PAM-8 modulation with phase shifted Manchester coding," *Optics express,* vol. 24, pp. 21663-21673, 2016.

[66] M. Zhang, M. Shi, F. Wang, J. Zhao, Y. Zhou, Z. Wang, *et al.*, "4.05-Gb/s RGB LED-based VLC system utilizing PS-Manchester coded Nyquist PAM-8 modulation and hybrid time-frequency domain equalization," in *Optical Fiber Communication Conference*, 2017, p. W2A. 42.

[67] Y. Zhou, J. Shi, J. Zhang, and N. Chi, "Spectral Scrambling for High-security PAM-8 Underwater Visible Light Communication System," in *2018 Asia Communications and Photonics Conference (ACP)*, 2018, pp. 1-3.

[68] J. Armstrong, "OFDM for optical communications," *Journal of lightwave technology,* vol. 27, pp. 189-204, 2009.

[69] Q. Wang, Z. Wang, and L. Dai, "Multiuser MIMO-OFDM for visible light communications," *IEEE Photonics Journal,* vol. 7, pp. 1-11, 2015.

[70] S.-a. Liu, J. He, Q. Chen, R. Deng, Z. Zhou, S. Chen, *et al.*, "Experimental research of adaptive OFDM and OCT precoding with a high SE for VLLC system," *Optical Fiber Technology,* vol. 37, pp. 21-25, 2017.

[71] P. Chvojka, K. Werfli, S. Zvanovec, P. A. Haigh, V. H. Vacek, P. Dvorak, *et al.*, "On the m-CAP performance with different pulse shaping filters parameters for visible light communications," *IEEE Photonics Journal,* vol. 9, pp. 1-12, 2017.

[72] F. Wu, C. Lin, C. Wei, C. Chen, Z. Chen, H. Huang, *et al.*, "Performance comparison of OFDM signal and CAP signal over high capacity RGB-LED-based WDM visible light communication," *IEEE Photonics Journal,* vol. 5, pp. 7901507-7901507, 2013.

[73] P. A. Haigh, A. Burton, K. Werfli, H. Le Minh, E. Bentley, P. Chvojka, *et al.*, "A multi-CAP visible-light communications system with 4.85-b/s/Hz spectral efficiency," *IEEE Journal on Selected Areas in Communications,* vol. 33, pp. 1771-1779, 2015.

[74] K. Werfli, P. Chvojka, Z. Ghassemlooy, N. B. Hassan, S. Zvanovec, A. Burton*, et al.*, "Experimental Demonstration of High-Speed 4× 4 Imaging Multi-CAP MIMO Visible Light Communications," *Journal of Lightwave Technology,* vol. 36, pp. 1944-1951, 2018.

[75] Glamox. *LED and lifetime*. Available: https://glamox.com/uk/led-and-lifetime

[76] J. Cho, J. H. Park, J. K. Kim, and E. F. Schubert, "White light‐emitting diodes: History, progress, and future," *Laser & Photonics Reviews,* vol. 11, p. 1600147, 2017.

[77] F. M. V. S. Standards. (2018). *Standard No. 108 Lamps, Reflective Devices, and Associated equipment*. Available: http://www.nhtsa.gov/cars/rules/import/FMVSS/#SN108

[78] UNECE. (2018). *Vehicle Regulations*. Available: http://www.unece.org/trans/main/welcwp29.html

[79] P. Luo, Z. Ghassemlooy, H. Le Minh, E. Bentley, A. Burton, and X. Tang, "Performance analysis of a car-to-car visible light communication system," *Applied Optics,* vol. 54, pp. 1696-1706, 2015.

[80] TheNationalArchieves. (2012). *Useful Information On Lighting*. Available: https://webarchive.nationalarchives.gov.uk/20120810123700tf_/http://www.highways.gov.uk/customer/25238.aspx

[81] E. D.-H. C. Council. (2010). *Street Lighting Design Guide 4th Edition*. Available: http://www3.hants.gov.uk/street_lighting_design_guide__4th_edition_.pdf

[82] G. Crabb, R. Beaumont, and D. Webster, "Review of the class and quality of street lighting," *TRL Published Project Report,* 2009.

[83] PremiumLightPro. *LED Street Lighting: Procurement & Design* Available: http://www.premiumlightpro.eu/fileadmin/user_upload/Guidelines/Premium_Light_Pro_Outdoor_LED_Guidelines.pdf

[84] H.-C. Chen, J.-Y. Lin, and H.-Y. Chiu, "Rectangular illumination using a secondary optics with cylindrical lens for LED street light," *Optics express,* vol. 21, pp. 3201-3212, 2013.

[85] J. Grubor, S. C. J. Lee, K.-D. Langer, T. Koonen, and J. W. Walewski, "Wireless high-speed data transmission with phosphorescent white-light LEDs," in *Optical Communication-Post-Deadline Papers*

(published 2008), 2007 33rd European Conference and Exhibition of, 2007, pp. 1-2.

[86] J. J. McKendry, R. P. Green, A. Kelly, Z. Gong, B. Guilhabert, D. Massoubre*, et al.*, "High-speed visible light communications using individual pixels in a micro light-emitting diode array," *IEEE Photonics Technology Letters,* vol. 22, pp. 1346-1348, 2010.

[87] J. J. McKendry, D. Massoubre, S. Zhang, B. R. Rae, R. P. Green, E. Gu*, et al.*, "Visible-light communications using a CMOS-controlled micro-light-emitting-diode array," *Journal of lightwave technology,* vol. 30, pp. 61-67, 2012.

[88] A. Rashidi, M. Monavarian, A. Aragon, A. Rishinaramangalam, and D. Feezell, "Nonpolar m-Plane InGaN/GaN Micro-Scale Light-Emitting Diode With 1.5 GHz Modulation Bandwidth," *IEEE Electron Device Letters,* vol. 39, pp. 520-523, 2018.

[89] T. Wu, C.-W. Sher, Y. Lin, C.-F. Lee, S. Liang, Y. Lu*, et al.*, "Mini-LED and micro-LED: Promising candidates for the next generation display technology," *Applied Sciences,* vol. 8, p. 1557, 2018.

[90] P. Patton. (2008). *So Efficient, L.E.D.'s Are Now Fashion Plates, Too.* Available: https://www.nytimes.com/2008/01/27/automobiles/27LIGHT.html

[91] M. H. M. Shamim, M. A. Shemis, C. Shen, H. M. Oubei, T. K. Ng, B. S. Ooi*, et al.*, "Enhanced performance of 450 nm GaN laser diodes with an optical feedback for high bit-rate visible light communication," in *CLEO: Science and Innovations*, 2018, p. JTu2A. 29.

[92] C. Knapman. (2014). *Are BMW's laser headlights really worth £8,000?* Available: https://www.telegraph.co.uk/cars/news/are-bmws-laser-headlights-really-worth-8000/

[93] OSRAM. (2017). *Laser technology from OSRAM – now yet in another premium car!* Available: https://www.osram.com/am/services/about-osram-automotive/references/laser-technology-for-bmw-7-series/index.jsp

[94] (2018). *What are some advantages of curved OLED TV?* Available: https://www.samsung.com/au/support/tv-audio-video/advantages-of-curved-oled-tv/

[95] (2018). *FlexPai*. Available: https://www.royole.com/flexpai

[96] P. Haigh, Z. Ghassemlooy, F. Bausi, I. Papakonstantinou, H. Le Minh, S. F. Tedde*, et al.*, "Organic visible light communications: Recent

progress," in *Transparent Optical Networks (ICTON), 2014 16th International Conference on*, 2014, pp. 1-5.

[97] J. Spindler, M. Kondakova, M. Boroson, M. Büchel, J. Eser, and J. Knipping, "84‐1: Invited Paper: Advances in High Efficacy and Flexible OLED Lighting," in *SID Symposium Digest of Technical Papers*, 2018, pp. 1135-1138.

[98] P. M. Pattison, M. Hansen, and J. Y. Tsao, "LED lighting efficacy: Status and directions," *Comptes Rendus Physique,* vol. 19, pp. 134-145, 2018.

[99] F. Zheng, J. Zou, B. Yang, Y. Zhou, M. Shi, Y. Liu*, et al.*, "Fabrication and optical properties of laser diodes based on composite phosphors film packaging," *Optik,* vol. 176, pp. 254-261, 2019.

[100] (2016). *Audi TT RS Matrix OLED Animation*. Available: https://www.audi-mediacenter.com/en/audimediatv/video/audi-tt-rs-matrix-oled-animation-3239

[101] OSRAM. (2017). *OLED rear lights for another premium car*. Available: https://www.osram.com/am/services/about-osram-automotive/references/oled-rear-lights-for-bmw-m4-gts/index.jsp

[102] L. Michel, *Light: The shape of space: Designing with space and light*: John Wiley & Sons, 1995.

[103] M. Roser and P. Lenz, "Camera-based bidirectional reflectance measurement for road surface reflectivity classification," in *Intelligent Vehicles Symposium (IV), 2010 IEEE*, 2010, pp. 340-347.

[104] A.-M. Ylinen, T. Pellinen, J. Valtonen, M. Puolakka, and L. Halonen, "Investigation of pavement light reflection characteristics," *Road Materials and Pavement Design,* vol. 12, pp. 587-614, 2011.

[105] M. Piragnolo, A. Masiero, F. Fissore, and F. Pirotti, "Solar irradiance modelling with NASA WW GIS environment," *ISPRS International Journal of Geo-Information,* vol. 4, pp. 711-724, 2015.

[106] Y.-J. Zhu, Z.-G. Sun, J.-K. Zhang, Y.-Y. Zhang, and J. Zhang, "Training receivers for repetition-coded MISO outdoor visible light communications," *IEEE Transactions on Vehicular Technology,* vol. 66, pp. 529-540, 2017.

[107] X. Zhu and J. M. Kahn, "Free-space optical communication through atmospheric turbulence channels," *IEEE Transactions on communications,* vol. 50, pp. 1293-1300, 2002.

[108] X. Zhu and J. M. Kahn, "Markov chain model in maximum-likelihood sequence detection for free-space optical communication through

atmospheric turbulence channels," *IEEE Transactions on Communications,* vol. 51, pp. 509-516, 2003.

[109] F. Hossain and Z. Afroze, "Eliminating the effect of fog attenuation on FSO link by multiple TX/RX system with travelling wave semiconductor optical amplifier," in *Advances in Electrical Engineering (ICAEE), 2013 International Conference on*, 2013, pp. 267-272.

[110] M. Elamassie, M. Karbalayghareh, F. Miramirkhani, R. C. Kizilirmak, and M. Uysal, "Effect of fog and rain on the performance of vehicular visible light communications," in *2018 IEEE 87th Vehicular Technology Conference (VTC Spring)*, 2018, pp. 1-6.

[111] Y. H. Kim, W. A. Cahyadi, and Y. H. Chung, "Experimental demonstration of VLC-based vehicle-to-vehicle communications under fog conditions," *IEEE Photonics Journal,* vol. 7, pp. 1-9, 2015.

[112] K. Cui, G. Chen, Z. Xu, and R. D. Roberts, "Experimental characterization of traffic light to vehicle VLC link performance," in *GLOBECOM Workshops (GC Wkshps), 2011 IEEE*, 2011, pp. 808-812.

[113] C. B. Liu, B. Sadeghi, and E. W. Knightly, "Enabling vehicular visible light communication (V2LC) networks," in *Proceedings of the Eighth ACM international workshop on Vehicular inter-networking*, 2011, pp. 41-50.

[114] A.-M. Căilean, B. Cagneau, L. Chassagne, M. Dimian, and V. Popa, "Novel receiver sensor for visible light communications in automotive applications," *IEEE Sensors Journal,* vol. 15, pp. 4632-4639, 2015.

[115] N. Lourenço, D. Terra, N. Kumar, L. N. Alves, and R. L. Aguiar, "Visible light communication system for outdoor applications," in *Communication Systems, Networks & Digital Signal Processing (CSNDSP), 2012 8th International Symposium on*, 2012, pp. 1-6.

[116] Hamamatsu. *Si PIN photodiode S9055-01*. Available: https://www.hamamatsu.com/jp/en/product/type/S9055-01/index.html

[117] P. P. Manousiadis, S. Rajbhandari, R. Mulyawan, D. A. Vithanage, H. Chun, G. Faulkner*, et al.*, "Wide field-of-view fluorescent antenna for visible light communications beyond the étendue limit," *Optica,* vol. 3, pp. 702-706, 2016.

[118] Hamamatsu. *High speed, compact Si APD for the 700 nm band featuring low-bias operation*. Available:

https://www.hamamatsu.com/eu/en/product/type/S14643-02/index.html

[119] D. Chitnis and S. Collins, "A SPAD-based photon detecting system for optical communications," *Journal of Lightwave Technology,* vol. 32, pp. 2028-2034, 2014.

[120] Autonews. (2013). *Rearview camera was one of Jordan's nifty tricks in '56*. Available: https://www.autonews.com/article/20150713/OEM03/307139919/rearview-camera-was-one-of-jordan-s-nifty-tricks-in-56

[121] ForzaSilicon. (2019). *History of Digital Imaging & Image Sensors*. Available: http://www.forzasilicon.com/history-of-digital-imaging/

[122] K. E. Laver, S. George, S. Thomas, J. E. Deutsch, and M. Crotty, "Virtual reality for stroke rehabilitation," *Cochrane database of systematic reviews,* 2015.

[123] Y. Wu, F. Tang, and H. Li, "Image-based camera localization: an overview," *Visual Computing for Industry, Biomedicine, and Art,* vol. 1, p. 8, 2018.

[124] Y. Li, Z. Ghassemlooy, X. Tang, B. Lin, and Y. Zhang, "A VLC Smartphone Camera based Indoor Positioning System," *IEEE Photonics Technology Letters,* 2018.

[125] X. Liu and Z. Zhu, "Advances in Optical Communications Technologies," *IEEE Communications Magazine,* vol. 56, pp. 176-176, 2018.

[126] N. Saha, M. S. Ifthekhar, N. T. Le, and Y. M. Jang, "Survey on optical camera communications: challenges and opportunities," *Iet Optoelectronics,* vol. 9, pp. 172-183, 2015.

[127] T. Nguyen, A. Islam, T. Hossan, and Y. M. Jang, "Current status and performance analysis of optical camera communication technologies for 5G networks," *IEEE Access,* vol. 5, pp. 4574-4594, 2017.

[128] N. Serafimovski, V. Jungnickel, Y. M. Jang, and J. Li, "An overview on high speed optical wireless light communications," *IEEE 802.11 Documents,* 2017.

[129] P. Chavez-Burbano, V. Guerra, J. Rabadan, C. Jurado-Verdu, and R. Perez-Jimenez, "Novel Indoor Localization System Using Optical Camera Communication," in *2018 11th International Symposium on Communication Systems, Networks & Digital Signal Processing (CSNDSP)*, 2018, pp. 1-5.

[130] N. T. Le, M. A. Hossain, and Y. M. Jang, "A survey of design and implementation for optical camera communication," *Signal Processing: Image Communication,* vol. 53, pp. 95-109, 2017.

[131] H. C. Hyun, T. Nguyen, J. S. Bong, K. H. Soon, and J. Y. Min, "Far distance LED-to-Ship Communication employing Optical Camera Communication," *한국통신학회 학술대회논문집,* pp. 1089-1090, 2015.

[132] N. Iizuka, "Image sensor communication—Current status and future perspectives," *IEICE Transactions on Communications,* vol. 100, pp. 911-916, 2017.

[133] S.-H. Chen and C.-W. Chow, "Hierarchical scheme for detection of rotating MIMO visible light communication systems using mobile-phone camera," in *Optical Communications and Networks (ICOCN), 2014 13th International Conference on*, 2014, pp. 1-4.

[134] P. Luo, M. Zhang, Z. Ghassemlooy, S. Zvanovec, S. Feng, and P. Zhang, "Undersampled-Based Modulation Schemes for Optical Camera Communications," *IEEE Communications Magazine,* vol. 56, pp. 204-212, 2018.

[135] P. Luo, Z. Ghassemlooy, H. Le Minh, H.-M. Tsai, and X. Tang, "Undersampled-PAM with subcarrier modulation for camera communications," in *Proc. Opto-Electron. Commun. Conf.(OECC)*, 2015, pp. 1-3.

[136] P. Luo, M. Zhang, Z. Ghassemlooy, H. Le Minh, H.-M. Tsai, X. Tang*, et al.*, "Experimental demonstration of a 1024-QAM optical camera communication system," *IEEE Photon. Technol. Lett.,* vol. 28, pp. 139-142, 2016.

[137] P. Hu, P. H. Pathak, X. Feng, H. Fu, and P. Mohapatra, "Colorbars: Increasing data rate of led-to-camera communication using color shift keying," in *Proceedings of the 11th ACM Conference on Emerging Networking Experiments and Technologies*, 2015, p. 12.

[138] S. Arai, S. Mase, T. Yamazato, T. Endo, T. Fujii, M. Tanimoto*, et al.*, "Experimental on hierarchical transmission scheme for visible light communication using led traffic light and high-speed camera," in *Vehicular Technology Conference, 2007. VTC-2007 Fall. 2007 IEEE 66th*, 2007, pp. 2174-2178.

[139] J. M. Kahn and J. R. Barry, "Wireless infrared communications," *Proceedings of the IEEE,* vol. 85, pp. 265-298, 1997.

[140] N. Rajagopal, P. Lazik, and A. Rowe, "Visual light landmarks for mobile devices," in *Information Processing in Sensor Networks,*

IPSN-14 Proceedings of the 13th International Symposium on, 2014, pp. 249-260.

[141] Z. Yang, H. Zhao, Y. Pan, C. Xu, and S. Li, "Magnitude matters: A new light-to-camera communication system with Multilevel Illumination," in *Computer Communications Workshops (INFOCOM WKSHPS), 2016 IEEE Conference on*, 2016, pp. 1075-1076.

[142] H. Du, J. Han, Q. Huang, X. Jian, C. Bo, Y. Wang*, et al.*, "Martian--message broadcast via LED lights to heterogeneous smartphones: poster," in *Proceedings of the 22nd Annual International Conference on Mobile Computing and Networking*, 2016, pp. 417-418.

[143] F. Yang, S.-N. Li, Z. Yang, C. Qian, and T. Gu, "Spatial multiplexing for non-line-of-sight light-to-camera communications," *IEEE Transactions on Mobile Computing,* 2018.

[144] J. Nakamura, *Image sensors and signal processing for digital still cameras*: CRC press, 2016.

[145] N. Waltham, "CCD and CMOS sensors," in *Observing photons in space*, ed: Springer, 2013, pp. 423-442.

[146] B. E. Bayer, "Color imaging array," *US patent 3,971,065,* 1976.

[147] R. A. Maschal Jr, S. S. Young, J. Reynolds, K. Krapels, J. Fanning, and T. Corbin, "Review of Bayer pattern color filter array (CFA) demosaicing with new quality assessment algorithms," Army Research Lab Adelphi Md Sensors and Electron Devices Directorate2010.

[148] NPL. (2019). *The eye's response to colour*. Available: http://www.npl.co.uk/publications/good-practice-online-modules/optical-radiation-safety/the-human-eye-and-light/the-eyes-response-to-colour/

[149] (2019). *Bayer Filter*. Available: https://en.wikipedia.org/wiki/Bayer_filter

[150] ITU. (2019). *Parameter values for the hdtv standards for production and*

international programme exchange. Available: https://www.itu.int/rec/R-REC-BT.709/

[151] J. C. Chau and T. D. Little, "Analysis of CMOS active pixel sensors as linear shift-invariant receivers," in *Communication Workshop (ICCW), 2015 IEEE International Conference on*, 2015, pp. 1398-1403.

[152] C. L. Joseph, E. Halkiadakis, S. Bernal, and D. Maiullo, *Modern Devices: The Simple Physics of Sophisticated Technology*: John Wiley & Sons, 2016.

[153] (2019). *Curve Shape in Digital Photography*. Available: http://www.covingtoninnovations.com/dslr/curves.html

[154] B. Clerckx and C. Oestges, *MIMO wireless networks: channels, techniques and standards for multi-antenna, multi-user and multi-cell systems*: Academic Press, 2013.

[155] R. Janaswamy, *Radiowave propagation and smart antennas for wireless communications*: Springer Science & Business Media, 2001.

[156] S.-H. Chen and C.-W. Chow, "Single-input multiple-output visible light optical wireless communications supporting quality of service," *Electronics Letters,* vol. 51, pp. 406-408, 2015.

[157] C.-W. Chow, C.-Y. Chen, and S.-H. Chen, "Enhancement of signal performance in LED visible light communications using mobile phone camera," *IEEE Photonics Journal,* vol. 7, pp. 1-7, 2015.

[158] A. Sturniolo, G. Cossu, E. Ciaramella, N. B. Hassan, Z. Shou, Y. Huang*, et al.*, "ROI Assisted Digital Signal Processing for Rolling Shutter Optical Camera Communications," in *2018 11th International Symposium on Communication Systems, Networks & Digital Signal Processing (CSNDSP)*, 2018, pp. 1-6.

[159] T. C. o. Philadelphia. (2017). *Municipal Energy Master Plan for the Built Environment*. Available: https://www.phila.gov/media/20170927092513/MunicipalEnergyMasterPlan.pdf

[160] Z. Li and C. Zhang, "An Improved FD-DFE Structure for Downlink VLC Systems Based on SC-FDMA," *IEEE Communications Letters,* 2018.

[161] A. M. Abdelhady, O. Amin, A. Chaaban, B. Shihada, and M.-S. Alouini, "Downlink resource allocation for dynamic TDMA-based VLC systems," *IEEE Transactions on Wireless Communications,* vol. 18, pp. 108-120, 2019.

[162] Y. Qiu, S. Chen, H.-H. Chen, and W. Meng, "Visible Light Communications Based on CDMA Technology," *IEEE Wireless Communications,* vol. 25, pp. 178-185, 2018.

[163] L. Yin, X. Wu, and H. Haas, "SDMA grouping in coordinated multi-point VLC systems," in *Summer Topicals Meeting Series (SUM), 2015*, 2015, pp. 169-170.

[164] Y. Wang, L. Tao, X. Huang, J. Shi, and N. Chi, "8-Gb/s RGBY LED-based WDM VLC system employing high-order CAP modulation and hybrid post equalizer," *IEEE Photonics Journal,* vol. 7, pp. 1-7, 2015.

[165] M. Hammouda, A. M. Vegni, H. Haas, and J. Peissig, "Resource allocation and interference management in OFDMA-based VLC networks," *Physical Communication,* 2018.

[166] Y. Yapici and I. Guvenc, "Non-Orthogonal Multiple Access for Mobile VLC Networks with Random Receiver Orientation," *arXiv preprint arXiv:1801.04888,* 2018.

[167] S. D. Perli, N. Ahmed, and D. Katabi, "PixNet: Interference-free wireless links using LCD-camera pairs," in *Proceedings of the sixteenth annual international conference on Mobile computing and networking*, 2010, pp. 137-148.

[168] K. Liang, C.-W. Chow, and Y. Liu, "RGB visible light communication using mobile-phone camera and multi-input multi-output," *Optics express,* vol. 24, pp. 9383-9388, 2016.

[169] T. Kondo, R. Kitaoka, and W. Chujo, "Multiple-access capability of LED visible light communication with low-frame-rate CMOS camera for control and data transmission of mobile objects," in *System Integration (SII), 2015 IEEE/SICE International Symposium on*, 2015, pp. 678-683.

[170] W. A. Cahyadi, Y. H. Kim, Y. H. Chung, and C.-J. Ahn, "Mobile phone camera-based indoor visible light communications with rotation compensation," *IEEE photonics journal,* vol. 8, pp. 1-8, 2016.

[171] T. Seybold, C. Keimel, M. Knopp, and W. Stechele, "Towards an evaluation of denoising algorithms with respect to realistic camera noise," in *Multimedia (ISM), 2013 IEEE International Symposium on*, 2013, pp. 203-210.

[172] W. Gu, M. Aminikashani, P. Deng, and M. Kavehrad, "Impact of multipath reflections on the performance of indoor visible light positioning systems," *Journal of Lightwave Technology,* vol. 34, pp. 2578-2587, 2016.

[173] H. J. Trussell and M. J. Vrhel, *Fundamentals of digital imaging*: Cambridge University Press, 2008.

[174] H. Tian and A. El Gamal, "Analysis of 1/f noise in CMOS APS," in *Sensors and Camera Systems for Scientific, Industrial, and Digital Photography Applications*, 2000, pp. 168-177.

[175] J. Redd. (2000). *Calculating statistical confidence levels for error-probability estimates*. Available:

https://www.lightwaveonline.com/articles/print/volume-17/issue-5/features/calculating-statistical-confidence-levels-for-error-probability-estimates-53462167.html

[176] L. U. Khan, "Visible light communication: Applications, architecture, standardization and research challenges," *Digital Communications and Networks,* vol. 3, pp. 78-88, 2017.

[177] Z. Zhou, M. Kavehrad, and P. Deng, "Indoor positioning algorithm using light-emitting diode visible light communications," *Optical Engineering,* vol. 51, p. 085009, 2012.

[178] J. Luo, L. Fan, and H. Li, "Indoor positioning systems based on visible light communication: state of the art," *IEEE Communications Surveys & Tutorials,* vol. 19, pp. 2871-2893, 2017.

[179] Y. Wang, N. Chi, Y. Wang, L. Tao, and J. Shi, "High speed LED based visible light communication networks for beyond 10Gb/s wireless access," in *Wireless Communications and Signal Processing (WCSP), 2014 Sixth International Conference on*, 2014, pp. 1-6.

[180] S.-H. Yang, D.-R. Kim, H.-S. Kim, Y.-H. Son, and S.-K. Han, "Indoor positioning system based on visible light using location code," in *Communications and Electronics (ICCE), 2012 Fourth International Conference on*, 2012, pp. 360-363.

[181] S. H. Yang, D. R. Kim, H. S. Kim, Y. H. Son, and S. K. Han, "Visible light based high accuracy indoor localization using the extinction ratio distributions of light signals," *Microwave and Optical Technology Letters,* vol. 55, pp. 1385-1389, 2013.

[182] Y. Hou, S. Xiao, H. Zheng, and W. Hu, "Multiple access scheme based on block encoding time division multiplexing in an indoor positioning system using visible light," *Journal of optical communications and networking,* vol. 7, pp. 489-495, 2015.

[183] B. A. Fowler, A. El Gamal, D. X. Yang, and H. Tian, "Method for estimating quantum efficiency for CMOS image sensors," in *Solid State Sensor Arrays: Development and Applications II*, 1998, pp. 178-186.

[184] Z. Zhou, B. Pain, and E. R. Fossum, "Frame-transfer CMOS active pixel sensor with pixel binning," *IEEE Transactions on electron devices,* vol. 44, pp. 1764-1768, 1997.

[185] A. Amantayeva, M. Yerzhanova, and R. C. Kizilirmak, "Multiuser MIMO for underwater visible light communication," in *2018 International Conference on Computing and Network Communications (CoCoNet)*, 2018, pp. 164-168.

[186] N. Omura, A. Higashi, J. Yabuuchi, T. Iwamatsu, and S. Oshiba, "Experimental Demonstration of OFDM Based WDM-MIMO Visible Light Communication System," in *2018 Asia-Pacific Microwave Conference (APMC)*, 2018, pp. 872-874.

[187] K. O. Akande, F. B. Offiong, H. Alrakah, and W. O. Popoola, "Performance Comparison of MIMO CAP Receivers in Visible Light Communication," in *2018 11th International Symposium on Communication Systems, Networks & Digital Signal Processing (CSNDSP)*, 2018, pp. 1-5.

[188] D. Tagliaferri, A. Matera, C. Capsoni, and U. Spagnolini, "Nonlinear visible light communications broadcast channel precoding: A new solution for in-flight systems," *IEEE Photonics Journal,* vol. 10, pp. 1-14, 2018.

[189] C. B. Peel, Q. H. Spencer, A. L. Swindlehurst, and M. Haardt, "An introduction to the multi-user MIMO downlink," *IEEE communications Magazine,* vol. 61, 2004.

[190] W. O. Popoola, E. Poves, and H. Haas, "Error performance of generalised space shift keying for indoor visible light communications," *IEEE Transactions on Communications,* vol. 61, pp. 1968-1976, 2013.

[191] K. Xu, H.-Y. Yu, Y.-J. Zhu, and H.-B. Cai, "Channel-adaptive space-collaborative constellation design for MIMO VLC with fast maximum likelihood detection," *IEEE Access,* vol. 5, pp. 842-852, 2017.

[192] K. Karakayali, R. Yates, G. Foschini, and R. Valenzuela, "Optimum zero-forcing beamforming with per-antenna power constraints," in *2007 IEEE International Symposium on Information Theory*, 2007, pp. 101-105.

[193] (2012). *Mercedes-Benz previews next-generation intelligent safety and driver assistance systems; "sensor fusion"*. Available: https://www.greencarcongress.com/2012/11/mb-20121122.html